Particle fueling and exhaust in the Wendelstein 7-X island divertor

by

Thierry Kremeyer

A doctoral dissertation submitted in partial fulfillment of the requirements for the degree of

Doctor of Philosophy
(Nuclear Engineering - Engineering Physics)

at the

University of Wisconsin - Madison
2019

Date of final oral examination: 12/13/2019

The dissertation is approved by the following members of the
Final Oral Committee:

Oliver Schmitz, Professor, Engineering Physics
David Anderson, Professor, Electrical and Computer Engineering
Benedikt Geiger, Assistant Professor, Engineering Physics
Chris Hegna, Professor, Engineering Physics
John Pfotenhauer, Professor, Mechanical Engineering
Thomas Sunn Pedersen, Professor, Max-Planck-Institut für Plasmaphysik,Greifswald

Abstract

A single-reservoir particle balance for the main species hydrogen has been established for Wendelstein 7-X (W7-X). This has enabled the quantitative characterization of the particle sources and sinks in the standard Island Divertor configuration for the first time. Findings from attached to first results for detached divertor scenarios are presented. Fueling efficiencies, flux balances and source locations were measured and used to infer the total particle confinement time. Perturbative gas injection experiments served to measure the effective particle confinement time τ_p^*. Combining both confinement times provides access to the overall recycling coefficient $\bar{R}$. Hydrogen and helium particle inventories have been addressed and the knowledge of particle sources and sinks provides insight into the capability of the magnetic island size and shape to control exhaust features.

The global particle balance revealed that no significant difference in the fueling efficiencies from up- and downstream gas fueling was found for H, and that overall the fueling efficiency of He was about 60 % higher. The recycling fluxes of the divertor and wall were found to govern the particle source. It was shown that in attached scenarios, 57 % of recycled particles came from the divertor, while the remainder of the overall recycling flux source was distributed between the baffle (9 %), heat shield (22 %) and steel panels (12 %). τ_p values in the range of 100 - 120 ms, depending on the exact density, were extracted for these discharges.

Together with τ_p, the global recycling coefficient $\bar{R}$ was calculated for every τ_p^* measurement and a typical value close to unity was obtained. This indicates that the wall reservoir was in the transition between small absorption or small desorption, depending on the density level of the previous discharge and the duration of the current discharge. An increase of the island size and shape through a control coil current, resulted in no change of τ_p but doubled τ_p^*, indicating the feasibility of the control coils as an actuator for stable divertor operation. The increase of the control coil current shifted 22 % of the particle flux, and therefore the recycling neutral source, from the divertor to the graphite tiles of the first wall shield. This led to more neutrals in the main chamber, which was detected in an increase of the neutral pressure by 23 %, and is consistent with the observed increase in τ_p^*. In addition, an increase of the radiated power by 51 % was seen in the scrape-off-layer (SOL), which was connected to an increase in the abundance of carbon impurities:

A 44 % increase in C-II emission normalized to density and temperature was measured in the SOL. Camera data also indicated that the carbon flux on the heat shield increased, due to the particle load increase observed that could cause an increase in first wall erosion. First assessment of detached divertor conditions shows that the fueled particle flux was fully balanced by the pumped flux with a constant wall source. The particle confinement time τ_p doubled to levels of 250 ms for these discharges. This is a result of a decrease of the overall recycling flux at an increased density level. The origin of this improvement in particle confinement is not clear at this point, but an equilibrium between sources and sinks was shown.

Helium exhaust was studied as an unavoidable impurity species in a later burning plasma. To obtain measurements, the Wisconsin In-Situ Penning (WISP) gauge has been designed, qualified, and implemented as part of this thesis. WISP gauges were installed at three poloidal positions in the same toroidal plane at W7-X. They were used to measure He and H partial pressures as well as total neutral pressures. While τ_p^* for H was around 8 s for the normal island, no significant decay of the neutral He was seen. No island size effects on the He pumping could be measured. A collection and build up of substantial helium partial neutral pressure in the island divertor was shown.

Acknowledgements

At this point I would like to thank the many people who supported me over the last five years along the way and made this thesis possible.

First of all, I would like to thank my advisor Oliver Schmitz for his guidance, many discussions and support throughout the completion of this work. Thank you for offering me the opportunity to start as a PhD student at UW, even though I was just looking for one semester abroad and despite me knowing nothing about plasmas.

Thomas Klinger, for taking his time for a young mechanical engineering intern that was in Greifswald for only one month and eager to learn about fusion. Thank you for your valuable advice and motivating me to take the leap into the physics side of fusion.

Thomas Sunn Pedersen for welcoming me in his department and allowing me to use his PAX magnet for the first high field testing of the WISP gauges.

Uwe Wenzel for welcoming me into the W7-X team and helping me with small and big challenges, especially in the beginning of my work at IPP.

Dirk Pilopp for his extensive support with the engineering and implementation of the immersion tubes. Without your help, the WISP gauges would not have been ready at the beginning of OP1.2.

Alexander Card for the support in data acquisition and making sure that all of the WISP data was stored reliably in the ArchiveDB.

Edward Thomas, Jr. and Darrick Artis at Auburn University for the opportunity to use MDPX for the in depth WISP testing. MDPX is such a great and versatile experiment and I could not have imagined a more supportive and welcoming atmosphere.

Sebastijan Brezinsek in his help and guidance in organizing and planing of the experimental session for fueling and exhaust. Thank you for the numerous spontaneous discussions and short lectures about atomic physics and plasma surface interaction.

Ralf König for the advice and guidance on developing the single-reservoir particle balance. Thank you for always having an open ear for me, whenever I spontaneously stopped by your office.

Jeffrey Harris and ORNL for supplying the Filterscope diagnostic at W7-X and making it available for the spectroscopic measurements of the WISP gauge.

Alexander Card, Freya Moran, Erik Flom, and Meghan Lazerson for being my native proof readers and working through this document.

Valeria Perseo for the quick moral support through Telegram whenever it was needed during the writing phase.

Thank you to my parents, Muddi and Holli, for helping me believe that I could be whatever I wanted to be, and teaching me the life skills and discipline necessary to get here. Thank you for always having my back and taking care of things when I didn't have the time.

Thank you Rory for being the best dog I could ask for, helping me relax and recharge my brain no matter how long or stressful the day was.

Finally, I would like to thank the University of Wisconsin, the United States Department of Energy, and all other agencies who have helped to fund and support this work.

This work was funded in part by the Department of Energy under grant DE-SC0014210.

The operation of the MDPX device is funded by the Department of Energy under Award Number DE-SC0019176, the NSF-DOE Partnership Program in Basic Plasma Science and Engineering (PHY-1613087 / DE - SC0016330), and the NSF-EPSCoR program (OIA-1655280). The MDPX device was originally designed and built with funding from the NSF-MRI program (NSF-1126067).

This work has been carried out within the framework of the EUROfusion Consortium and has received funding from the Euratom research and training programme 2014-2018 and 2019-2020 under grant agreement No 633053. The views and opinions expressed herein do not necessarily reflect those of the European Commission.

Contents

1 Introduction **1**

2 Background **7**

2.1 Wendelstein 7-X - A quasi-isodynamic optimized stellarator . 7

2.2 The Island Divertor - Operational flexibility with different configurations 12

2.2.1 Island size effects on neutral compression 19

2.3 Helium exhaust in stellarators 22

2.4 Physical principles of a Penning discharge 26

2.5 The S/XB method - Converting photon to particle fluxes . . . 30

3 Diagnostic Setup and Analytic Computation **34**

3.1 Available key diagnostics 34

3.1.1 Integral Electron Density Dispersion Interferometer . . 36

3.1.2 Main Gas Inlet System 37

3.1.3 Divertor Gas Box / Thermal Helium Beam Diagnostic 38

3.1.4 Langmuir Probe Arrays 40

3.1.5 Multi Purpose Manipulator 41

3.1.6 Filtered Visible Cameras 42

3.2 Introduction to a global, single-reservoir particle balance . . . 45

3.2.1 Total amount of particles 47

3.2.2 Fueling efficiencies 47

3.2.3 Gas sources from gas injections 49

3.2.4 Φ_{wall} - A recycling dominated source term 50

Photon flux from Cameras 52

Filterscope 53

Determination of S/XB at W7-X 54

3.2.5 Effective confinement time τ_p^* and $\bar{R}$ 61

3.3 Proof-of-principle of a spectroscopically assisted Penning gauge at W7-X 63

4 The Wisconsin In-situ Penning (WISP) Probe Head **67**
4.1 Anode design . . . 67
4.2 The WISP probe head . . . 70
4.3 Experimental set up at MDPX . . . 73
4.4 WISP behavior in different scenarios . . . 75
4.4.1 Magnetic field scan . . . 75
4.4.2 Anode potential scan . . . 77
4.4.3 Gas dependency of ion current measurement . . . 78
4.4.4 Partial pressure scan . . . 79
4.4.5 Misalignment test . . . 81
4.4.6 Aging . . . 84
4.5 Successful implementation at W7-X . . . 85
4.5.1 Setup of assembly . . . 85
Probe head space . . . 86
Immersion tube . . . 86
Interface . . . 87
4.5.2 Spectroscopic set-up at W7-X . . . 87
4.5.3 Calibration at W7-X . . . 88
4.5.4 Comparison with ASDEX pressure gauges . . . 90

5 Single-Reservoir Particle Balance for Hydrogen **93**
5.1 Gas injection fueling is unaffected by island size and fueling location . . . 96
5.2 Fueling efficiency of recycled H particles . . . 97
5.3 Particle confinement based on the single-reservoir particle balance . . . 99
5.4 Sensitivity of τ_p to key input parameters: S/XB_{Wall}, f_{recy}, and camera view angle . . . 102
5.4.1 Sensitivity to S/XB_{Wall} . . . 102
5.4.2 Sensitivity to recycling fueling efficiency f_{recy} . . . 103
5.4.3 Sensitivity to the camera view angle . . . 105
5.5 τ_p, τ_e, and τ_p^* behavior with increase in island size . . . 107
5.6 Increased island size leads to a shift of particle loads onto main wall components . . . 111
5.7 Increase of P_{Rad} likely due to increased sputtering on the shield 114
5.8 The particle balance in detached scenarios . . . 120

6 Helium Fueling and Exhaust **127**
6.1 Comparison of fueling efficiencies for helium and hydrogen . 127

6.2 Build up of substantial helium partial neutral pressure in the island divertor 128

7 Conclusion and future work **132**

7.1 Conclusion 132

7.2 Future work 134

7.2.1 Additional fueling systems for the particle balance . . 135

7.2.2 Effective S/XB coefficients 135

7.2.3 Comparison with modeling 136

Chapter 1

Introduction

One of the biggest challenges for mankind will be to provide a secure, sustainable, safe, and carbon-free energy supply in the future. This requires a fundamental change in the global energy mix and a shift away from fossil fuels [1]. While renewable energies like wind, solar, or hydro power are sustainable, they inherently suffer from strong fluctuations in their output power. Due to the lack of large-scale area-wide energy storage systems, renewable energies will not be able to securely provide the base load energy demand of industrial nations [2]. Nuclear fusion could be a possible solution.

Nuclear fusion describes a reaction in which two smaller atomic nuclei fuse together to form a heavier one. Their combined mass is less than that of the addition of their independent masses - an effect that is due to differing binding energies. This is known as the mass defect, where the difference in mass is released as energy. A first generation fusion power plant will utilize a fusion reaction between the two heavy hydrogen (H) isotopes, deuterium (D) and tritium (T), exploiting the characteristic that this reaction has the greatest energy yield at the lowest temperature [3]. The two isotopes, when undergoing fusion, form a helium (He) nucleus, a neutron, and release 17.6 MeV of energy, as shown in equation 1.1.

$$D_1^2 + T_1^3 \rightarrow He_2^4(3.5MeV) + n_0^1(14.1MeV) \tag{1.1}$$

Extremely high energies are necessary to bring the two positively-charged nuclei close enough together, so that the strong nuclear force can overcome the coulomb repulsion [3]. In this energy range, matter is in the state of an ionized gas where nuclei are stripped of their orbital electrons. This is called a plasma and is known as the fourth state of matter. Due to the separation of the electrons and ions, the plasma becomes electrically conductive, and

is dominated by long-range electric and magnetic fields and can be manipulated by such. The use of magnetic fields to confine the plasma for the purpose of generating thermonuclear fusion power is known as magnetic confinement fusion [4].

To achieve a burning, self-sustaining plasma, three conditions have to be met simultaneously. The first is the aforementioned high temperatures T on the order of millions of degrees Celsius (around 10 keV or 1.16×10^8 K). Secondly, a sufficient particle density n is necessary to guarantee a threshold number of collisions to occur. Finally, the energy confinement time τ_e describes the rate at which the system loses energy. The triple product is the product of T, n, and τ_e. By analyzing the power balance of a fusion plasma, one can find the value above which the plasma ignites. This is quantified in the so-called Lawson criterion, which describes the lower-limit of values required to achieve a self-sustained continuous fusion reaction [5]. The minimum of the triple product occurs at the smallest cross section at $T = 14\ keV$, and the criterion becomes:

$$nT\tau_e > 3 \cdot 10^{21} \frac{keV\ s}{m^3} \tag{1.2}$$

The two most viable magnetic confinement concepts for energy production - known as the tokamak and stellarator - utilize toroidal magnetic field configurations to confine plasmas with the goal of achieving the Lawson Criterion. Helically-twisted magnetic fields are necessary to mitigate the effects from curvature drifts. The plasma particles will stay in the machine moving along field lines and can only escape by moving across them.

The tokamak requires three superimposing magnetic fields to create the helical magnetic fields required to confine the plasma [6]. A toroidal field is created by planar coils outside the plasma vessel. A central solenoid stack works as a transformer with the plasma itself taking the place of the secondary winding. This induces a current in the plasma itself which forms the second field. This leads to a twisting of the field lines and results in a helical combined field. A third, vertical field is then used to position the current inside of the plasma. The tokamak concept requires continuous inductive current drive or replacement by non-inductive methods, which increases the need for control actuators and the recirculating power to sustain the plasma current. The plasma current is significant, 15 MA for ITER, which results in the risk of violent plasma termination by disruptions [6].

The stellarator concept, in contrast, does not require a driven toroidal current to create the confining field, which removes the need for a solenoidal transformer, and by extension pulsed operation [7]. This makes stellarators suitable for continuous steady-state operation. The magnetic confinement field arises from a discretized series of electromagnetic coils, external to the plasma vessel, which are preformed in such way that the superposition of their fields produces the required complex, helical shape. The resulting field varies over three-dimensions; it is not axisymmetric as in the case of the tokamak. While this represents a much more complicated scenario, it also allows for new freedoms in shaping the magnetic field in order to optimize desired properties. Modern technology - in both the super computers which design the coil shapes, and the superconducting materials which enable continuous operation of high magnetic field strengths - has enabled the optimization of stellarator field configurations to perform in such a way as to to overcome a historical drawback: confinement of high-energy, collisionless particles. Three main concepts for optimized stellarators emerged over the last decades, which address this issue [8]. Out of these three optimizations, the quasi-isodynamic concept was chosen as the design basis of W7-X [9].

In a fusion reaction the neutron will leave the confined area as it is not affected by the magnetic field. The charged He nuclei, or He ash, is bound to the confining field. This allows the He to deposit its energy into the plasma, thereby heating it. However, this induces the need for efficient removal of these helium atoms from the plasma, since the He can lead to fuel dilution that can ultimately extinguish the plasma. In order to allow a fusion plasma to sustain its energy losses by self-heating from the fusion process, the He concentration is limited to about 10 % without other impurities present, making a sufficient He exhaust mandatory for a reactor [10]. The part of the fusion device designed to generate the necessary neutral pressures for adequate pumping and exhaust is called the divertor. Divertors are used to achieve a sufficient He and impurity exhaust during operation and form a well defined plasma boundary [11][12]. The divertor concept and the importance of He exhaust will be discussed in more detail in chapter 2.

The magnetic field of W7-X is designed in a way that natural small radial magnetic field perturbations induce islands on low order rational surfaces [13]. Target plates are positioned at ten stellarator-symmetric locations to intersect these islands and utilize them as the interface for PFCs in the island divertor. The island size can be manipulated by divertor control coils and serves as a control parameter to optimize divertor performance.

This dissertation is an effort towards exploring the fueling, exhaust, and recycling of the island divertor in W7-X. The impact of the island size on particle confinement, and the exhaust properties from a plasma edge and divertor perspective are simultaneously presented. This was assessed in two ways: First, a global, single-reservoir particle balance for the main ion species H was established, and enabled the quantitative characterization of the particle sources and sinks in the main Island Divertor scenarios. The particle confinement time τ_p for H was determined by linking the density time trace to the plasma outflux and the refueling particle sources [14]. Second, the density decay time of a perturbative gas injection was analyzed to measure the effective confinement time τ_p^* of H and He [14].

The exhaust of helium was quantified in this thesis by analysis of the helium confinement and neutral pressure dynamics. To address these questions a new diagnostic dedicated for the implementation in W7-X was developed.

Penning gauges assisted by spectroscopy are a powerful tool to obtain the total neutral pressure as well as fractional neutral pressures of specific impurities [15]. The WISP gauge is a miniaturized Penning gauge arrangement, which exploits the ambient magnetic field of magnetic confinement fusion experiments to establish the Penning discharge. Then, in-situ spectroscopy is conducted to separate the fractional neutral pressures of hydrogen, helium and possibly also other impurities. The WISP probe head was qualified using the magnetic field of the Magnetized Dusty Plasma Experiment, MDPX, at Auburn University between 0.25 T and 3.5 T [16]. It was successfully implemented and operated in the Wendelstein 7-X (W7-X) island divertor baffle and vacuum vessel [17]. Quantitative measurements of the neutral household for light impurities, in particular helium, is important for tokamak as well as stellarator divertors in order to quantify the removal rate of impurities and thus avoid fuel dilution and excessive radiative energy loss [18].

In this thesis the in-depth quantitative evaluation for hydrogen and helium will be shown as well as measurements from the second Test Divertor Unit (TDU) campaign at W7-X, so-called OP1.2b [19]. The development of the WISP gauge will be described as well as experimental exploration of W7-X discharges, focusing on the island size effect on fueling, exhaust, and recycling through the particle balance. This thesis is organized as follows:

- **Chapter 2 - Background:** This chapter provides a short review of topics necessary for the understanding of this thesis. The first section introduces the W7-X stellarator in more detail, discussing the magnetic field, its symmetries, and the plasma facing components important in

this work. Subsequently the island divertor and the various operational configurations are introduced. The importance of He exhaust, particularly in stellarators is discussed. Finally the physical principles of a Penning discharge and the S/XB coefficient, used to convert photon into particle fluxes, are introduced.

- **Chapter 3 - Diagnostic Setup and Analytic Computation:** The key diagnostics that were used to measure density, gas fluxes, and how the total wall source was evaluated from multiple camera and other photon flux observations are introduced. This section is followed by an introduction of the global, single-reservoir particle balance. A detailed explanation of how the individual terms of the particle balance are calculated. A partial pressure gauge for He exhaust studies was still missing, and in this section the first proof-of-principle of an optically assisted Penning gauge to fill this gap is presented.

- **Chapter 4 - The Wisconsin In-Situ Penning (WISP) probe head:** The newly developed Wisconin In-Situ Penning (WISP) gauge is introduced. The results of an in depth testing at MDPX at Auburn University are shown, as well as the implementation of the probe head at W7-X.

- **Chapter 5 - Single-Reservoir Particle Balance for Hydrogen:** Results of the analysis of the particle balance are presented. First, the experiments on different fueling efficiencies are compared to each other. Following this, the τ_p calculations of the particle balance are compared with τ_p^* measurements. The effect of a larger island size will be discussed in regards to particle fluxes to different plasma facing components. The particle balance was used to analyze the transition into a detached scenario and its challenges will be discussed.

- **Chapter 6 - Helium fueling and exhaust:** The direct assessment of the He fueling and exhaust properties with the island divertor is presented, which utilizes the new WISP diagnostic. A substantial neutral pressure build up with He injections was measured in the island divertor.

- **Chapter 7 - Conclusion and future work:** An increase of the island size, from control coil current 0 kA to 2 kA, resulted in no change of τ_p but doubled τ_p^*. The increase of the island size shifted 22 % of the particle flux, and therefore the recycling neutral source, from the divertor to the graphite tiles of the first wall shield. The particle confinement time τ_p

increased significantly when transitioning from the attached to the detached phase of a W7-X discharge. The thesis will end with an outlook on future work.

Chapter 2

Background

2.1 Wendelstein 7-X - A quasi-isodynamic optimized stellarator

The magnetic field configuration used for W7-X results from a quasi-isodynamic optimization. The optimization technique, besides W7-X, was also used as a basis for the HELIcal-axis Advanced Stellarator, or HELIAS reactor study [20]. Wendelstein 7-X is the first superconducting machine based on this optimization of the magnetic field. Unlike its predecessor Wendelstein 7-AS (Advanced Stellarator), which was partially optimized to reduce equilibrium currents [21], W7-X is fully optimized towards multiple goals such as equilibrium stability, low neo-classical transport, reasonably good energetic particle confinement and feasibility of construction. The quasi-isodynamic optimization aims to minimize the internal plasma currents, i.e. Pfirsch-Schlüter and Bootstrap current, so that an equilibrium is almost entirely provided by the external magnetic field [8].

Rising plasma pressure can induce an outward radial displacement of the inner magnetic surfaces, which is called the Shafranov shift [22]. The Shafranov shift can be minimized by reducing the Pfirsch-Schlüter current, as done in the HELIAS design [23]. Thus the magnetic field of W7-X becomes stable against changes of the plasma pressure, which is important for the island divertor concept [24]. In the island divertor concept, natural occurring islands in the plasma edge are intersected by target plates. This will be discussed in greater detail in the next section. A significant Pfirsch-Schlüter current could induce a Shafranov shift that would lift the island to a position where it is no longer intersected by the target plates, thus negating the island divertor concept. First experiments revealed a Shafranov shift of 1 - 2 cm [19], which is in agreement with theoretical predictions.

In a reactor scenario the highly energetic He ion, so-called α particle,

needs to be confined for at least one slowing down time, so that the energy can be transferred to the thermal plasma. Without this energy transfer, a self-sustained burning plasma would not be feasible. To achieve sufficient confinement of fast particles, W7-X utilizes five linked magnetic mirrors resulting in the five fold symmetry of the magnetic field. These mirrors are created by increasing the magnetic field between the field periods [25] as shown in figure 2.1.

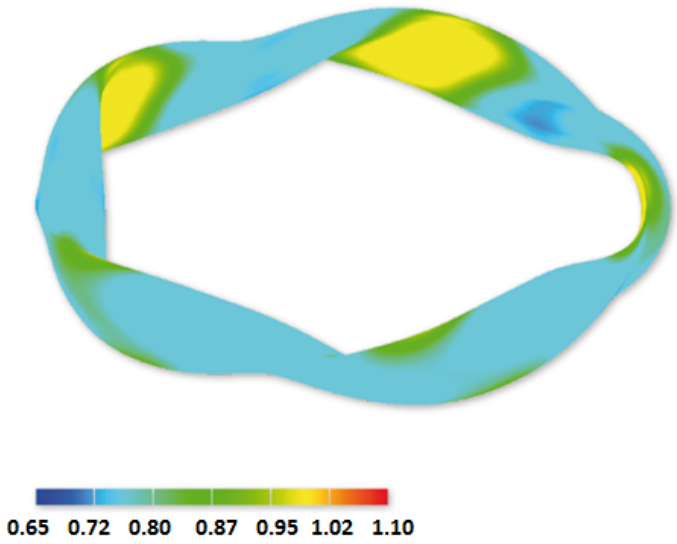

FIGURE 2.1: Magnetic field strength of the quasi-isodynamic configuration. Image taken from [9, Fig. 3].

The increase in field strength to form these magnetic mirrors can be seen in yellow on the in-board side of the magnetic surface topology. A fraction of the particles are trapped in between these mirrors and oscillate back and forth, resulting in a poloidal rotation but no movement across the mirror in the toroidal direction, and are thus kept away from zones of high field inhomogeneity [24] [25]. Figure 2.2 visualizes this drift orbit for the example of a 300 keV T ion that is trapped in the low magnetic field region. The strength of the magnetic surface is color coded similar to figure 2.1, with the stronger field in green, going into yellow at maximum field strength on the left and right side of the image. The particle movement of the T ion is pictured in red where the oscillation between the mirrors is superimposed by a net poloidal rotation.

The five-fold symmetric field is created by 50 modular coils of five different types, 20 planar coils of two different types, as well as 5 trim coils. The machine was assembled out of five identical modules, each consisting of point symmetric half modules. A computer-aided design (CAD) drawing of

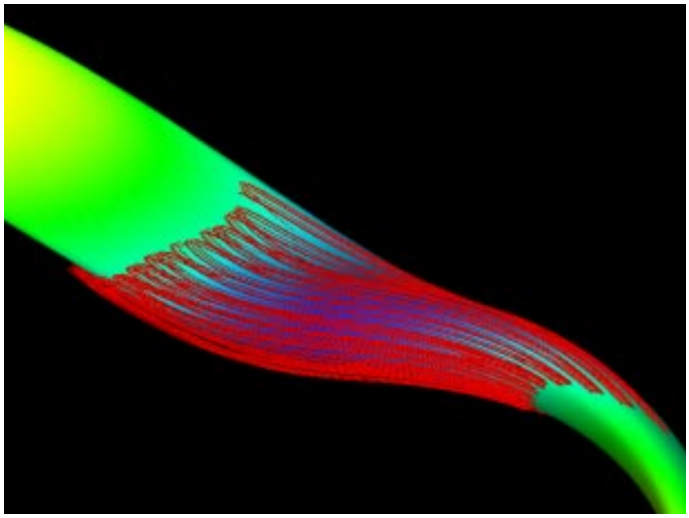

FIGURE 2.2: Path of a reflected 300 keV T ion in a poloidally closed drift orbit. The coloring of the magnetic field surface indicates the magnetic field strength, similar to figure 2.1. Image taken from [25, Fig. 11].

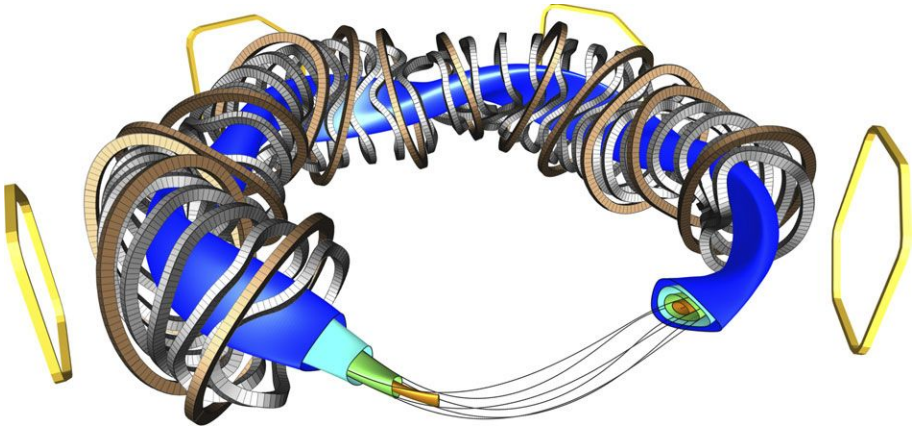

FIGURE 2.3: CAD drawing of the three different coil types and their location around some nested magnetic surfaces. The modular coils are shown in grey, planar coils in brown and the saddle trim coils in yellow. The fifth trim coil as well as some planar and non-planar coils in the foreground are not pictured, so as to not obstruct the view on the magnetic field surfaces. Image taken from [26, Fig. 1].

the different coil types around the magnetic field are depicted in figure 2.3. The blue surface is cut open in the front, revealing some of the underlying nested surfaces. On the right side a cross section through all the closed surfaces is shown. Surrounding the blue surface, that visualizes the last closed flux surface (LCFS), are the coils that create the field. The superconducting non-planar coils are shown in gray. The planar coils which are also superconducting, are pictured in copper brown and four of the five trim coils in

yellow. The planar coils can be used to change the rotational transform ι. $\frac{\iota}{2\pi}$ is defined as the number of poloidal turns per toroidal turn of a field line on a toroidal flux surface and describes the twist of the magnetic field. Due to deviations during manufacturing and assembly of the coils, as well as deformations due to gravity, the "as-built" coils and regular field can vary slightly from the designed field [27]. These deviations are known as error fields and some mode components can be corrected with the trim coils [26]. The trim coils are not super conducting and are mounted on the outside of the cryostat in the form of saddle coils. The construction of W7-X and field mapping during the startup campaign has already demonstrated, that it is possible to construct such an optimized 3D magnetic field within the required accuracy and symmetry despite the high complexity of the machine itself [26].

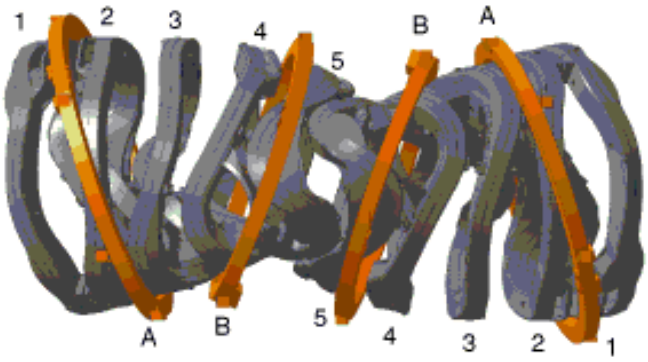

FIGURE 2.4: CAD drawing of coils in one module. Modular coil types 1-5 in grey and planar coils type A and B in brown are pictured as they appear in one module. The point symmetry of the half modules is clearly visible. Image taken from [28, Fig. 1(b)].

The coil set up for one module is shown in figure 2.4. Here the ten non-planar coils in each module are again shown in grey. The five different kinds are numbered 1 through 5. The four planar coils of types A and B are pictured in copper brown. The half modules are split between the two non-planar coils number 5 and the point symmetry of them is visible. The modules are number 1 through 5 with the respected half modules 0 and 1. The first half module of module two would therefore be identified as half module 20, while the second half module of module 5 would be considered half module 51. This serves as an easy numbering system to identify the location of different divertor modules, ports and diagnostics.

Depending on the operational phase considered, different heating systems are available. In the future final stage (OP2+) between 10-15 MW of

steady-state electron cyclotron radiation heating (ECRH), 3.5 MW pulsed (2 s) ion cyclotron radiation heating (ICRH) as well as neutral beam injection (NBI) heating power at 14/20 MW for H/D was available. In this phase W7-X will be designed for discharge lengths up to 30 min at an integrated input heating energy of 18 000 MJ. An overview of the device parameters during the test divertor campaign OP1.2 which is the experimental phase relevant for this thesis, is shown in table 2.1. The exact values and layout chosen for the discharges presented in this thesis is covered in detail in the preface of chapter 5.

Average Major Radius	5.5 m
Average Minor Radius	0.53 m
Plasma Volume	28.6 m^3
Plasma mass	5 - 30 mg
Plasma Density	up to 1.2×10^{20} m^{-3}
T_e	3.4 keV
T_I	$\approx T_e$
Discharge length	10 - 100 s
Volume of plasma vessel	$\approx 50m^3$
B (on axis)	2.5 T
Triple product	6.4×10^{19} $\frac{\text{keV s}}{\text{m}^3}$

TABLE 2.1: Wendelstein 7-X device parameters for OP 1.2 [19].

The plasma vessel of W7-X is equipped with a variety of plasma facing components (PFCs) that serve different purposes. For this analysis five different types of PFCs are considered. These are shown in the example around one divertor module in figure 2.5. The PFCs will be introduced in order of their designed heat flux capability: the divertor, the baffle, the heat shield, and the steel wall panels. Here the divertor target plates, made out of fine-grain graphite, are shown in light blue. The horizontal and vertical target are shown in light blue with the pumping gap, shown in yellow, in between. The divertor is surrounded by the baffle which consists of many individual graphite tiles. A majority of the inboard side and other areas that are predicted to be exposed to significant heat loads are covered by the heat shield. The heat shield also consists of individual graphite tiles, similar to the baffle, however designed to take a lower heat flux. The other areas with comparably low heat fluxes are then covered with steel panels.

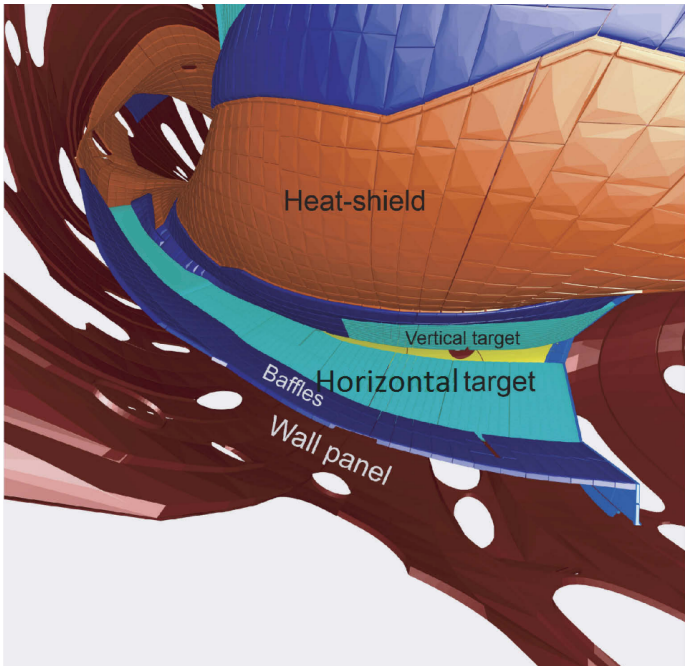

FIGURE 2.5: CAD drawing of the PFCs around one divertor element. The different PFCs are color coded. The divertor target plates with the horizontal and the vertical target in light blue. These targets are surrounded by the baffle in dark blue. The largest PFCs area-wise is the heat shield in orange and the wall panels in dark red. Image taken from [29, Fig. 6(a)(modified)].

2.2 The Island Divertor - Operational flexibility with different configurations

W7-X utilizes a helical resonant divertor concept, the island divertor, for efficient power and particle exhaust which was tested on a smaller scale on W7-AS [30]. The island divertor structure is aligned as close fitting shells with the basic 3D equilibrium of the device. Certain variations in ι are possible, which allows W7-X to be run in different configurations, leading to some degree of operational flexibility. However, the dependence of the divertor performance on the actual magnetic configuration is a key aspect of the exploration and qualification effort of the island divertor concept.

The rotational transform ι was briefly introduced in the previous section as the number of poloidal turns per toroidal turn of a magnetic field line. Mathematically this can be expressed using the poloidal and toroidal magnetic field strength B_p and B_t together with the major radius R and the minor radius r as [6]:

$$\frac{\iota}{2\pi} = \bar{\iota} = \frac{B_p}{B_t}\frac{R}{r} \tag{2.1}$$

An unperturbed magnetic field line would close on itself on a rational surface after one toroidal turn. The magnetic field of W7-X however is designed in a way that induces islands on low order rational surfaces [13]. Since these islands are formed by the external coils, the edge islands are part of the vacuum magnetic field. The planar coils provide experimental flexibility with

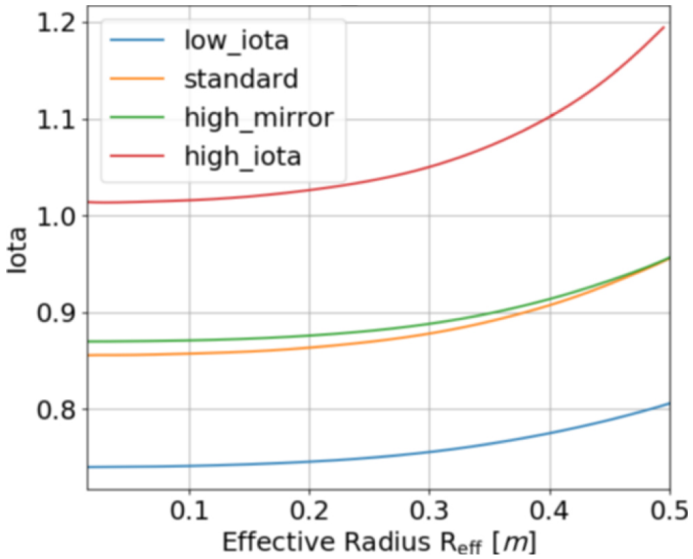

FIGURE 2.6: Rotational transform ι plotted over the effective radius R_{eff} for different magnetic field configurations at W7-X. Image taken from [31, Fig. 2].

the island divertor, by allowing to change ι. The island divertor can be operated with three different iota values that form the different island chains. These iota profiles as function of the effective radius R_{eff} are shown in figure 2.6.

The configuration with $\bar{\iota} = 5/6$ is called the low iota configuration, the 5/5 is used for the standard and high mirror configuration, while the 5/4 on the high end of the spectrum is called the high iota configuration. Also the iota can be increased such, that no low order resonance is located at the plasma radius of the divertor targets, which allows to bring a good flux surface in contact with the divertor targets generating a limiter scenario [32].

All discharges in this study were conducted in the standard divertor configuration with an edge iota of 5/5. The standard divertor configuration (SDC) – while being considered as the best divertor structure for optimal alignment of strike lines on the divertor target as well as optimal neutral compression features - might in fact not be optimal for steady-state operation since it is expected to feature a significant level of boot-strap current [32]. This current changes the iota profile in the plasma edge and would

thereby alter the island geometry and thus the divertor properties. Mitigation or complete avoidance of such direct impact of plasma equilibrium effects on the divertor configuration and performance is highly desired.

The divertor target plates are placed to intersect these islands to create open field lines that end on the target. The first open field line following the last closed flux surface (LCFS) is known as the separatrix and is sketched in figure 2.7. Here a cross section of the bean-shaped plane of W7-X is shown

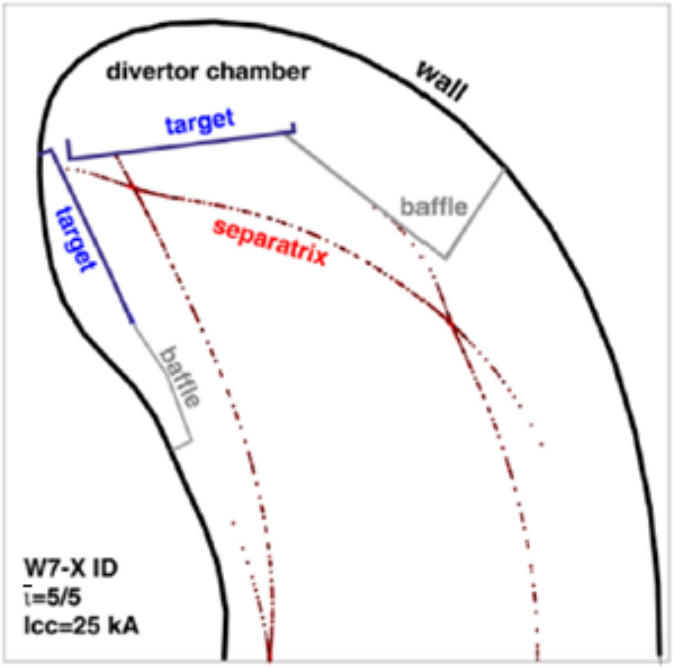

FIGURE 2.7: Cross-section of the standard divertor configuration of W7-X at the bean shaped plane. Image taken from [32, Fig. 1].

with the horizontal target on the top and the vertical target to the left in blue. The separatrix for the $\bar{\iota} = 5/5$ case, caused by the intersected islands is shown in red. The particles are led across the X-point on the open field lines until they strike the target plates. The area where particles hit the target are therefore also known as strike lines or as the wetted area.

A CAD model of a divertor module overlaid with a Poincaré plot in red and the wetted area in blue is shown in figure 2.8. The standard 5/5 island structure can be seen in the Poincaré plot and how the two islands in the lower left part of the image are intersected by the target plates, creating open field lines. Particles that follow these open field lines are directed onto the target plate where they are neutralized. These wetted areas on the target plates, based on field line tracing with diffusion, are visualized in blue.

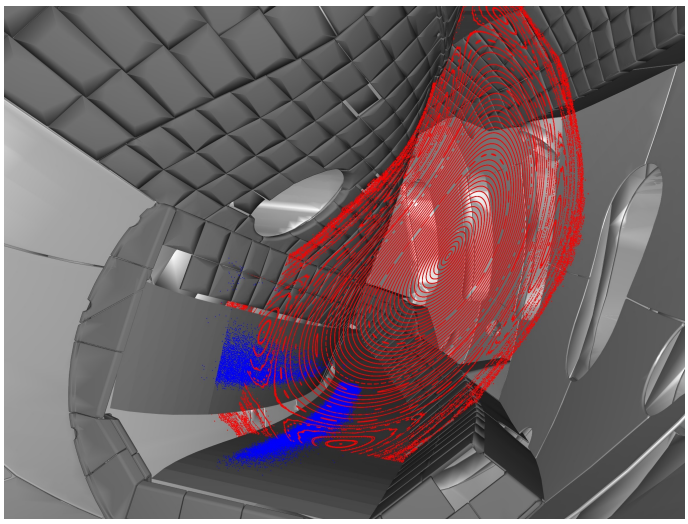

FIGURE 2.8: CAD drawing of a divertor module overlaid with a Poincaré plot of the standard configuration in red and the wetted area in blue. Courtesy of S. Lazerson.

Lower divertor (Half module)	Connected upper divertor (Half module)
10	31
20	41
30	51
40	11
50	21

TABLE 2.2: Magnetically connected divertor modules in the standard configuration at W7-X.

This increases the neutral density around the pump duct, through which the particles can be exhausted.

In the standard configuration each of the five islands is intersected by two divertor modules, causing a magnetic connection between these two modules. This becomes important when comparing different diagnostics, as will be discussed in chapter 3. Each lower divertor module is magnetically connected with an upper divertor two modules further. Table 2.2 serves as an overview of the magnetic divertor pairs.

When following an intersected flux tube from one divertor module to the other, they can make many toroidal turns before intersecting the magnetically paired divertor. At W7-X, an individual flux tube inside the island does not close on itself after one toroidal rotation but shifts slightly clockwise inside the island. This continues for each following toroidal rotation until the flux tube is intersected by the paired target. This leads to much longer target-target connection lengths at W7-X - being an order of magnitude higher than

in tokamaks - where it is usually on the order of tens of meters [13]. The connection length L_c depends on the number of islands N, the radial island width r_i, the shear at the resonance ι', as well as the major radius R, and can be described as[33]:

$$\frac{L_c}{2\pi} = \frac{R}{N r_i \iota'} \tag{2.2}$$

Ten identical divertor modules have been installed in stellarator-symmetric locations. Each module contains one upper and one lower divertor as pictured in figure 2.9, thus preserving the five-fold symmetry. Here the divertor

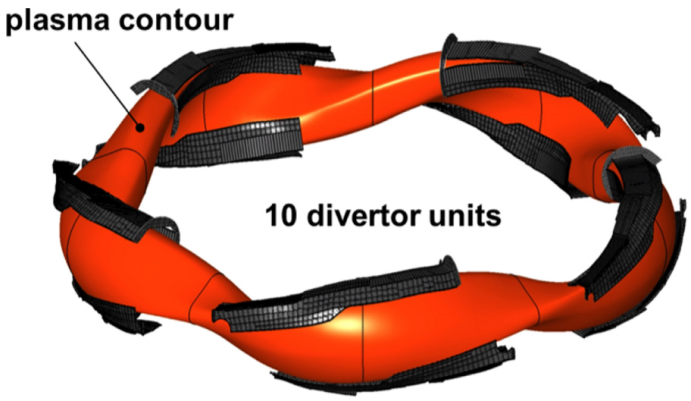

FIGURE 2.9: CAD drawing of the ten divertor modules in grey placed around theplasma contour in orange. Thin black lines seperate the half modules. Image taken from [31, Fig. 1].

modules are shown with their respective positions around the LCFS of the base-line plasma contour in orange. The half modules are separated by thin black lines. With this visualization it becomes clear that the placement of the divertor modules not only preserves the five-fold symmetry of the device, but also the point symmetry of the half modules. Each divertor module congregate consists of a horizontal and a vertical target with the pumping gap in between, as briefly shown in figure 2.5. The design of each of these modules is pictured in figure 2.10 in greater detail.

In figure 2.10, the areas that are designed for the highest heat flux are shown in red. In the front, the horizontal and vertical part of the divertor targets are located around the pumping gap. The horizontal target is much longer than the vertical target since the wetted area shifts depending on the configuration. In the low iota and standard configuration the wetted area is located in the front, while the red area on the horizontal target in the back is known as the high-iota tail since that is the configuration that will put the particle load on this area. For cost reduction reasons the part in between is designed to take a smaller heat load and is marked in yellow. The target

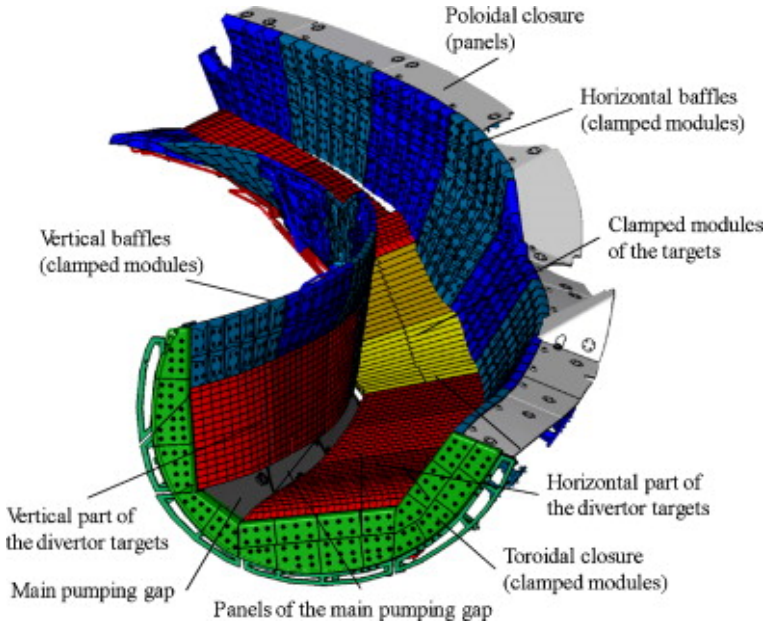

FIGURE 2.10: CAD drawing of a divertor module showing the different target plates, pumping gap, baffles and closures. Image taken from [34, Fig. 2].

plates are surrounded by baffles shown in blue. The baffles, together with the poloidal closures in grey and the toroidal closure in green, close off the divertor such that neutral gas, pumped through the pumping gap, cannot reenter the main chamber but stays in the divertor closure long enough until it gets pumped out of the machine by the vacuum pumps.

Recent results from OP1.2 have shown that there is a significant leakage from the divertor closure, and only 34 % of the particles that get transported through the pumping gap get removed by the vacuum pumps. The rest of the particles flow back into the main chamber resulting in a higher neutral pressure on the mid-plane, that is coupled to the sub-divertor neutral pressure. A high backflow and a moderate compression is not a problem as long as the neutrals are ionised in the SOL and reenter the divertor. The divertor during OP1.2 is therefore considered a partially closed divertor [35].

For the operational phase considered in this thesis, these divertor modules were only inertially cooled and were called the "Test Divertor Unit" or TDU [36]. The plasma facing components of the TDU were manufactured out of fine-grain graphite-fiber composite, while the steady-state, water-cooled, high-heat-flux (HHF) divertor will be made out of carbon-fiber reinforced carbon (CFC) [37].

In addition to the flexibility towards changes in the edge ι, each divertor

module is equipped with a divertor control coil that can be used to manipulate the island. The control coil current I_{cc} is commonly used as a metric to describe the island manipulation and can be varied from $-2.5\,\mathrm{kA}$ to $2.5\,\mathrm{kA}$. For this study the standard island at $I_{cc} = 0\ kA$ was compared to a magnetic structure of the island with $I_{cc} = 2\ kA$. While applying a control coil current does not change the edge ι it does change the field line pitch and therefore the connection length as described in equation 2.2 [38]. The connection lengths and magnetic structure for the two cases that are compared in this thesis are shown in figure 2.11.

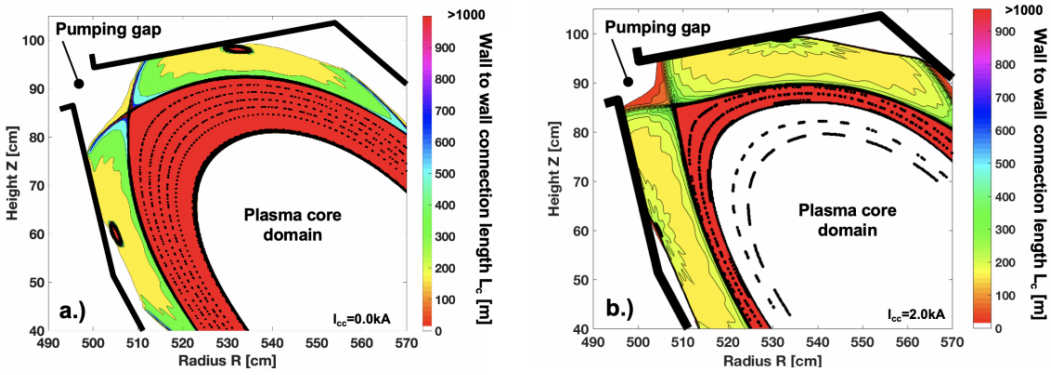

FIGURE 2.11: Wall to wall connection length of the island structure with $I_{cc} = 0\ kA$ in (a) and the island structure with $I_{cc} = 2\ kA$ in (b) at toroidal angle $\phi = 12.5$ with L_c towards plasma core > 1000 m. Taken from [39, Fig. 6].

Here the normal island case on the left (a) is compared with the $I_{cc} = 2kA$ island on the right (b). The overlaid Poincaré plot shows the closed flux surfaces inside the separatrix with long connection lengths in red. The wall to wall connection length L_c reduces significantly when crossing the 5/5 separatrix, revealing flux surfaces that are intersected by the target plates and therefore reduced in L_c. This domain thus represents the SOL of the island divertor.

Multiple features are visible that can have an effect on recycling, neutral distribution and ionization. Intuitively the largest impact on neutral pressure is due to the strike line location, which moves 5.9 cm closer to the pumping gap, with an increase in control coil current from $I_{cc} = 0kA$ to $I_{cc} = 2kA$. At the same time, L_c is reduced from 500 m to under 200 m at the strike line location. The island width at the O-point increases from ~ 6 cm to ~ 9 cm, while the outer separatrix moves much closer to the outer baffle. This could lead to an increase in neutral pressure in the main chamber, but could also trap recycling neutrals from the horizontal target and retain them in the SOL.

2.2.1 Island size effects on neutral compression

To obtain a first general insight into the effect of such changes of the island size and structure on particle exhaust, a dedicated modeling study is briefly reviewed [32]. This study by Feng et al. uses the EMC3-EIRENE code, which is a plasma edge fluid and kinetic neutral model. A self-sustained global particle balance is achieved by assuming 100 % recycling on PFCs, without pumping and external particle sources. Hydrogen plasmas are assumed, with carbon as a representative impurity species. Since this study is focused on how to achieve detachment, there was no helium involved. The general exhaust properties inferred by Feng et al. served as guidelines for the experiments detailed in chapter 5 [32].

With respect to fueling and exhaust as the central topic of this thesis work, this paper by Feng et al. serves as an orientation on the basic trends of particle exhaust and neutral dynamics across a broad density range and three different island sizes. It will be investigated in this thesis how the island size affects the total neutral and fractional H and He pressure in the divertor chamber as well as particle confinement time τ_p, effective particle confinement time τ_p^* and the global recycling coefficient $\bar{R}$.

The understanding on how the island size affects these parameters can then be used as the groundwork for an optimization towards further improvement of the exhaust. It is of scientific and operational importance to understand if the island size can be used as a control parameter for stable divertor operations, but is also of economic significance since the edge islands take up valuable space inside the vacuum vessel that could otherwise be used for confinement [32].

Hydrogen plasmas, at a total input power into the scrape of layer (SOL) of 10 MW, with carbon as the main impurity species, were used as input conditions for the modeling. The SOL is separated by the LCFS from the confined area. These input conditions are representative for the general experimental plasma conditions. Limited heating power in OP1.2 places detailed side-by-side comparisons on the topic of particle exhaust outside the scope of this thesis. As motivated in section 2.2, the study numerically compared the standard configuration with the high-mirror configuration, in order to address if the comparably small changes in the edge topology alter the divertor exhaust characteristics significantly.

In the model, the following metrics were used by Feng et al. to characterize the divertor performance: carbon density n_C, concentration C_C at the LCFS, and the neutral density n_n /pressure p_n in the divertor chamber; all

monitored while increasing the level of carbon radiation in terms of the radiated power P_{rad}. However, the concept of radiating thermal power with low-Z impurities in the edge bears the risk of impurity contamination of the plasma core [32]. It was therefore concluded in the study, that it is desirable to generate a divertor situation with a high radiation fraction in the SOL and divertor domain, low carbon concentration in the plasma core and a high neutral pressure. These were henceforth used as the modeling benchmark criteria for assessing the divertor performance.

The island size at W7-X can be adjusted using the divertor control coils or by using different currents in the planar coils. Changing the planar coil currents triggers global changes to the equilibrium, for example the case of the edge ι as discussed in section 2.2. In the study by Feng et al. the island size was varied by applying the planar coils to shift the 5/5 resonance with respect to the targets and was changed between small, medium and large for each configuration.

The EMC3-EIRENE simulations were performed with $n_e = 6 \times 10^{19} \frac{1}{\mathrm{m}^3}$ and $D = 0.5 \frac{\mathrm{m}^2}{\mathrm{s}}$ for different radiation fractions. In Figure 2.12 the neutral pressure in the divertor chamber, as function of carbon radiation fraction for high-mirror configurations (left) and SDC (right) [32], is shown. The differences in the absolute P_0 between the high-mirror configuration and the SDC, is mainly due to different strike line locations and are not an effect of the island size. However, within each configuration, the small and medium-sized island show a rollover effect with increasing radiation, i.e. the divertor pressure first increases with the carbon radiation fraction, peaks and then drops. In contrast to this rollover the carbon radiation seems to have no effect on the divertor pressure in the large island scenario. In both cases the highest divertor pressure is seen with the medium island case, followed by the small island. The smallest divertor pressure is expected for the large island case. The results of these simulations indicate that the medium-sized islands are optimal for neutral compression in both, the high mirror and the SDCs. Contributions from energetic hydrogen atoms are not taken into consideration in this study since they are less relevant for neutral pressure measurements and particle pumping [32].

In contrast to this simulation, the control coils were utilized as the preferred method to change the island size during the OP1.2 experimental campaign, and therefore also in the experiments presented in this thesis. As a qualitative comparison the natural island with $I_{cc} = 0\ kA$ will be compared to a enlarged island at the boundary of the technical capabilities of the control

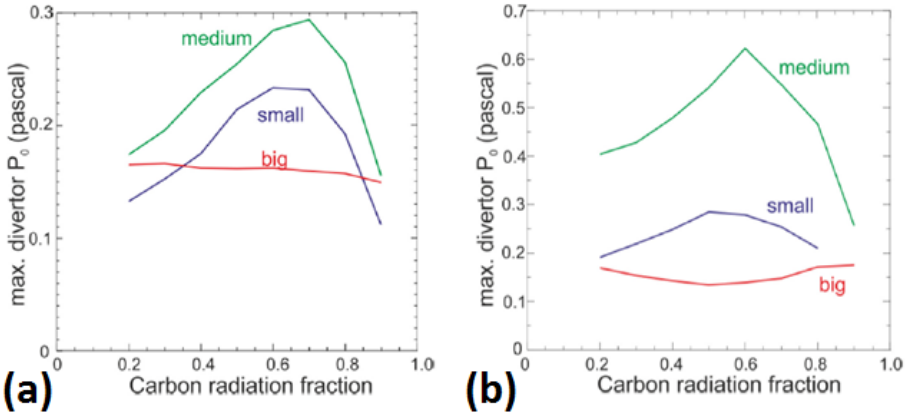

FIGURE 2.12: Neutral pressure in the divertor chamber as function of carbon radiation fraction for high-mirror configurations (a) and SDC (b). Taken from [32, Fig. 8 & 9].

coils with $I_{cc} = 2\ kA$ as the large island case.

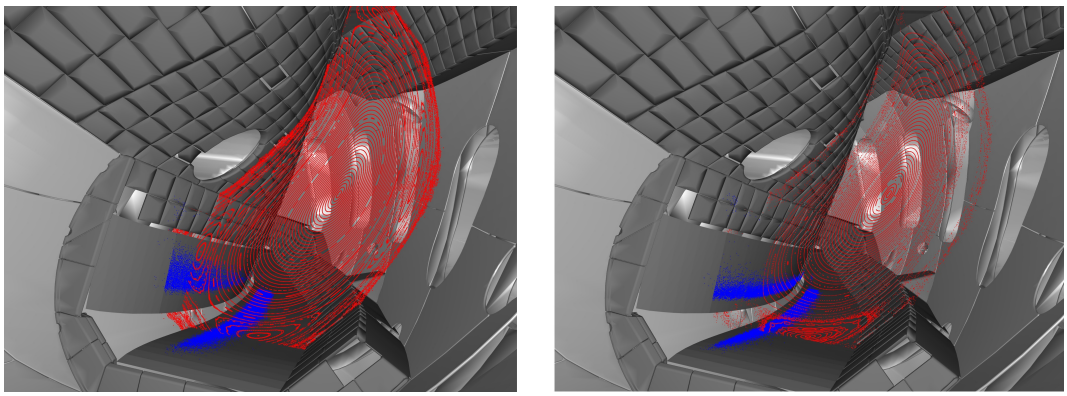

FIGURE 2.13: Poincaré plot of the normal island on the left with $I_{cc} = 0kA$ and the large island with $I_{cc} = 2kA$ on the right. The Poincaré plot with the change in the edge topology is visualized in red, while blue marks the wetted area on the horizontal and vertical target. Courtesy of S. Lazerson.

In figure 2.13 a CAD model of a divertor segment with the horizontal target on the bottom and the vertical target to the left of it are shown, as introduced in section 2.2 in figure 2.10. The CAD model is overlaid with a Poincaré plot in red that visualizes the change in the closed flux surfaces in the edge topology with an increase in island size. The wetted area or strike line is pictured in blue. The strike line becomes narrower and shifts closer to the pumping gap which should increase the neutral pressure in that region. The increase in island size brings the island closer to the baffle on the right - this could potentially trap neutrals that are released from the target plates and keep them from reentering the plasma. The increase in the neutral density on the target should ultimately increase the likelihood of these particles

being exhausted. In addition to the changes in strike line location and the potential of the island blocking recycling neutrals, an increase in island size with the control coils changes the field line pitch. The effects of the field line pitch on the connection length have been discussed in section 2.2 and figure 2.11, and should be kept in mind in this context.

The effects of the control coil current on the island size, edge topology, field line pitch and therefore connection length, strike line location, and potential trapping of neutrals have been discussed in the last two sections. The island size and magnetic structure change is revealed as a potential control parameter for stable divertor operation. By utilizing a single-reservoir particle balance, the experiments presented in this thesis are purposed to explore this potential as a control parameter.

2.3 Helium exhaust in stellarators

A steady-state D-T fusion reaction in a future fusion reactor would continuously produce helium, therefore one of the main design functions of a divertor is to realize sufficient exhaust of the resulting He ash. Helium is hence the dominant plasma impurity and is of great interest to impurity transport and exhaust studies. If not properly exhausted, an increase in He concentration leads to a dilution of the reactant - thus He concentrations above ≈ 10 % are not acceptable [40].

Besides diluting the thermonuclear plasma, helium can also radiate confined energy which decreases the fusion rate [41]. Control of the helium ion density is also important for edge physics and plasma material interaction, as helium is an effective sputtering species which can alter erosion properties and hence the first wall and divertor material integrity [42].

An analytical analysis of the impact of He concentrations on the burn criterion [10] [43] reveals a connection between the energy confinement time τ_E and the effective α-confinement time τ_α^*. The increase of the α-particles in the plasma ($\dot{N}_\alpha$) can be calculated from the difference of the reaction rate and the He pump rate. The reaction rate is described by the number of deuterium and tritium particles N_D and N_T and the fusion rate coefficient $\langle \sigma v \rangle_{fus}$ while the He pump rate is described by the ratio of the number of α-particles N_α and their effective confinement time, as seen in equation 2.3.

$$\dot{N}_\alpha = N_D N_T \langle \sigma v \rangle_{fus} - \frac{N_\alpha}{\tau_\alpha^*} \tag{2.3}$$

The change of the energy content $\dot{W}$ of the plasma is given by the difference between the energy increase through the α particle heating E_α and the energy decrease through mechanisms that lead to a finite value for the energy confinement time τ_E. Assuming $T_e = T_i$:

$$\dot{W} = N_D N_T \langle \sigma v \rangle_{fus} E_\alpha - \frac{3\,(N_e + N_D + N_T)\,T_e}{2\,\tau_E} \tag{2.4}$$

From quasi-neutrality the electron density can be described as $N_e = N_D + N_T + 2N_He$. For low He concentrations this can be simplified and if we take $N_e = N_D + N_T$, a He concentration of under 10 % ($\frac{N_\alpha}{N_e} < 0.1$) and an electron temperature between 10 and 20 keV we arrive at equation 2.5 for the stationary case:

$$\frac{\tau_\alpha}{\tau_E} = \frac{N_\alpha}{N_e}\frac{E_\alpha}{3k\,T_e} \leq 10 \tag{2.5}$$

What is shown is that both insufficient particle and energy confinement, which prevents the ignition of the plasma, as well as high impurity particle confinement can be disadvantageous for a steady-state reactor due to the He accumulation.

Helium exhaust can be considered in different reservoirs, each one representing a specific spatial domain around the plasma, with each region requiring different diagnostics to measure their He concentration. The α particles are created in the plasma core where they must be transported into the edge and out through the last closed flux surface (LCFS), neutralized at a divertor, pumped through the pumping gap, and eventually removed from the device through pumping by appropriate pumps.

To achieve stable plasma edge conditions, it is mandatory to establish and control a stable and well-defined plasma wall interface (PWI) and SOL. Thus, it is important to find an operating regime where the energy confinement is large enough to allow ignition, but also allows sufficient particle and impurity exhaust. This is not only true for He but also for species that might be used for edge cooling like neon and for impurities in general or for impurities born by plasma material interaction. For the tokamak concept, successful He exhaust capabilities have been demonstrated at ASDEX-U [44] and DIII-D [45]. Both devices have a poloidal divertor geometry and were able to show that their $\frac{\tau_\alpha}{\tau_E}$ ratio was at the margin [46] or even exceeding the feasible ratio of 10. Methods to improve He exhaust are still of great interest, especially for stellarators which have a transport regime which has a negative radial electric field that produces an inward directed neoclassical impurity transport, called the ion root regime [47] [48] [49]. In these cases, it is important to

improve the outward transport of He as well as other impurities. Since typical exhaust efficiencies for helium ε_{He} are well below 10 %, it is important to retain helium in the SOL, and avoid He transport back into the confined region [50]. The exhaust efficiency can be expressed by the global recycling coefficient $\bar{R}$ that will be discussed in chapter 3 as equation 2.6 [51].

$$\varepsilon_{exh} = 1 - \bar{R} \tag{2.6}$$

Equation 2.6 describes the probability of a particle to be removed from the plasma by the pumping system. For a particle to be exhausted it first needs to be transported from the SOL into the pumping gap. The probability of a particle in the SOL to enter the pumping gap is described as the collection or SOL exhaust efficiency ε_{SOL}. After the particle arrives at the pumping gap it needs to be removed from the system by the vacuum pumps. The probability for this process is called the removal or pumping efficiency ε_{pump}. The overall exhaust efficiency of He can therefore be described as the product of the SOL and pumping efficiency as seen in equation 2.7 [51].

$$\varepsilon_{He} = \varepsilon_{SOL} * \varepsilon_{pump} \tag{2.7}$$

The pumping efficiency depends on the pumping speed S of the pumping system and the neutral pressure p that the system is pumping against, and the flux of recycled helium. The pumping speed is the mean volume flow over time through, in this case, the pumping gap [52].

$$S = \frac{dV}{dt} \tag{2.8}$$

The actual volume flow rate or pumped flux is then described by the product of the pumping speed and the neutral pressure, depicted in equation 2.9.

$$q_{pV} = S \cdot p = \frac{dV}{dt} \cdot p \tag{2.9}$$

In turbomolecular vacuum pumps which are commonly used to create high and ultra high vacuums on fusion machines, the compression ratio varies exponentially with the square root of the molecular weight of the gas. This means that a turbomolecular pump has different pumping speeds for different gases [52]. To calculate the volume flow rate of a particular gas, like in our case helium, the pumped flux would be described by the product of the

pumping speed and the partial pressure, defined in equation 2.10.

$$q_{He} = S_{He} \cdot p_{He} \tag{2.10}$$

Equation 2.10 describes the pumped He flux in the divertor. However not all particles that get transported into the pumping gap get pumped out of the system. Some particles also leave the pumping gap and recycle back into the plasma, which can be described as a recycling flux Γ_{He}. The He pumping efficiency can therefore be described as:

$$\varepsilon_{pump,He} = p_{He} \cdot \frac{S_{eff,He}}{\Gamma_{He}} \tag{2.11}$$

and the overall He exhaust efficiency as:

$$\varepsilon_{He} = \varepsilon_{SOL} \cdot p_{He} \cdot \frac{S_{eff,He}}{\Gamma_{He}} \tag{2.12}$$

The pumping speeds at the divertor are commonly determined by in-situ calibration while the recycling flux can be derived from the observed photon flux. With known edge temperatures and densities, this photon flux can be converted into a particle flux with the use of the S/XB coefficient, which will be discussed later in this chapter. The He partial pressure however has to be measured directly, and in the case of a fusion reactor, in a deuterium environment.

Even though many residual gas analyzers (RGA) that function on the principle of quadrupole mass spectrometers (QMA) struggle to resolve the mass difference between He at 4.003 amu and D_2 at 4.028 amu, there are some commercial RGAs that claim to be capable of doing so. However they are sensitive to ambient magnetic field and thus might have to be mounted further away. Another diagnostic technique is to excite the neutral gas while observing the discharge spectroscopically and using the emitted line intensities for partial pressure measurements. Optical observations have been used on ASDEX-type hot cathode ion gauges [53], while a comparison of different electron sources to excite the neutral gas has found that the best line-emitting light sources is a Penning discharge [18].

2.4 Physical principles of a Penning discharge

The following section will explain how a Penning discharge is established using a combination of electric and magnetic fields. This section will serve as the physical background for a proof-of-principle implementation of an optically assisted Penning gauge during OP1.1 in section 3.3, and will be applied for the more sophisticated development of the WISP probe head in chapter 4.

The Penning discharge was discovered by F.M. Penning in 1936 [54]. Penning originally used it as a simple glow discharge plasma source at low pressures. He described experiments regarding the ignition potential and the characteristics of the glow discharge between coaxial cylinders in an axial magnetic field as shown in figure 2.14. Here a cross section of the two cylinders is seen. The outer cylinder is held at ground and serves as the cathode while the anode, which is pictured as the small inner circle, is held at a positive potential.

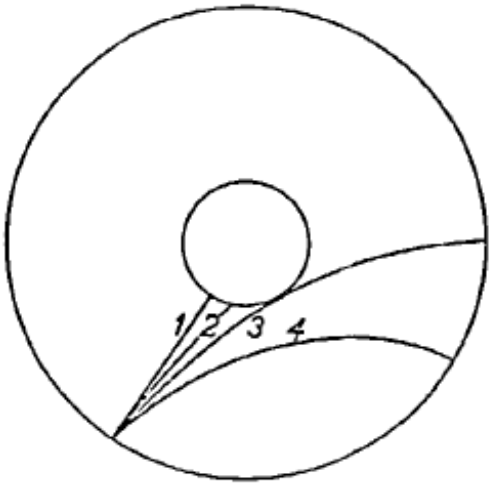

FIGURE 2.14: Electron paths between co-axial cylinders in an axial magnetic field. B is increasing from 1 to 4. Taken from [54, Fig. 1].

Without the magnetic field, electrons leaving the cathode would just be accelerated towards the anode. With a magnetic field of sufficient strength, they will follow a cycloidal path of considerable length before reaching the anode. If the magnetic field exceeds the field of path 3, the anode current goes to zero and the electrons are captured by the cathode. When introducing neutral gas at low pressure into the system, some of the electrons will collide with the neutral particles. If the electron loses energy greater than its work function, it becomes impossible for the electron to return to the cathode. The

electron path lengths thus increase very substantially and the electrons ionize more neutral particles through electron collision than they would without a magnetic field [54]. For the glow discharge a lengthening of the electron path has the same effect as an increase in pressure. This makes it possible to maintain a stable glow discharge at pressures where a discharge would not be possible without an increase of the electron pathway due to the magnetic field, without changing any other parameters.

Modern Penning gauges and traps use a slightly different electrode configuration, but keep the idea of using a magnetic field to lengthen the path of the charged particles. Depending on the direction of the electric field, positively or negatively charged particles can be trapped. Penning traps are used for precise measurements of properties of ions and stable subatomic particles. They are mostly used within the field of mass spectrometry. At CERN Penning traps are also used to store anti-protons [55].

The Penning principle can also be utilized to create robust neutral pressure gauges. In the common Penning trap, charged particles are trapped by a combination of a constant magnetic field with an electrostatic quadrupole field as shown in Figure 2.15. Here a cross section of a cylindrical anode (a) is shown that is closed with surrounding cathode plates (b) at the two openings. The magnetic field (B) is aligned co-axially to the cylindrical anode. An example electron is shown which is centered in the co-axial direction by the electrical force F_E from the cathode. The gyro motion resulting from the present magnetic field is sketched as well.

When using a Penning cell as a pressure gauge instead of a trap, an electron cloud is trapped inside the quadrupole field. In a magnetic field B, the electrons oscillate due to the Lorenz force with the mass m and the charge q in a circular path around the magnetic field line at the cyclotron frequency.

$$\omega_c = \frac{q}{m} B \tag{2.13}$$

Due to the electric quadrupole field this movement gets modified. The actual movement of a particle in a Penning cell can be described through a set of three harmonic oscillators [57]. The electrons oscillate axially through the cylindrical anode (a), getting pushed back and forth by the force of the electrical field F_E created by the cathode end plates. The axial frequency ω_z due to the electric field with the potential U can be described as:

$$\omega_z = \sqrt{\frac{q}{m}\frac{U}{d^2}} \tag{2.14}$$

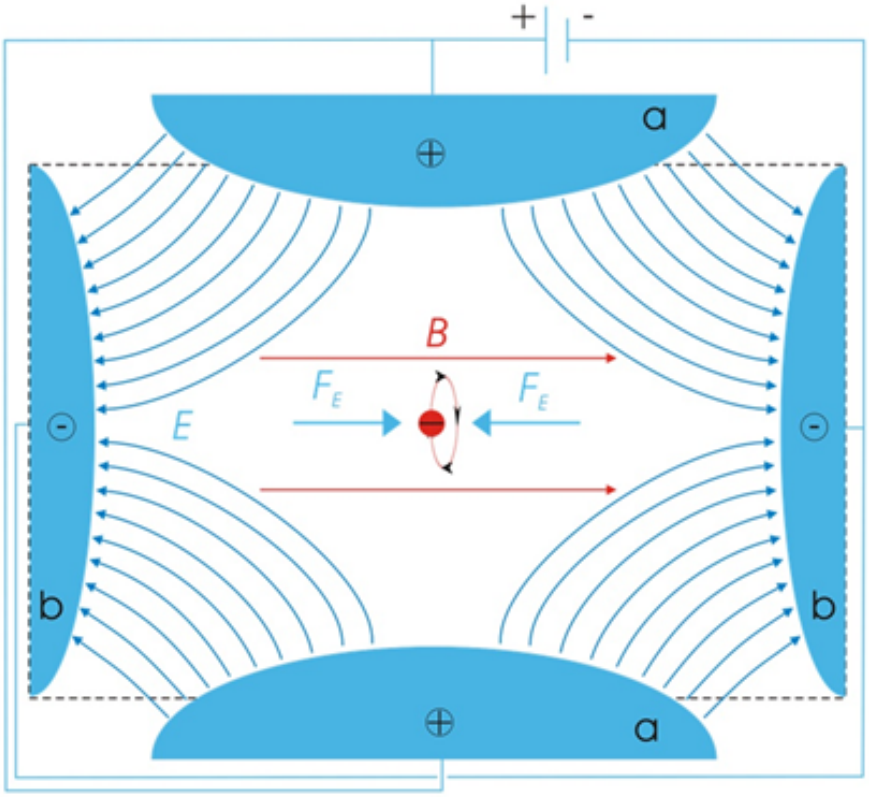

FIGURE 2.15: Schematics of the quadrupole field of a Penning trap, Ring Anode (a) and Cathode (b). Based on a sketch from [56].

where d is a geometrical parameter that can be calculated out of the distance from the center to the end cap z_0 and the radius of the anode ring r_0:

$$d^2 = \frac{1}{2}\left(z_0^2 + \frac{r_0^2}{2}\right) \tag{2.15}$$

The radial movement is defined by two frequencies, the modified cyclotron frequency and the Magnetron frequency. The modified cyclotron movement follows a circular path around the magnetic field lines, with the frequency being decreased by the electric quadrupole field [57]:

$$\omega_+ = \frac{\omega_c}{2} + \sqrt{\frac{\omega_c^2}{4} - \frac{\omega_z^2}{2}} \approx \omega_c - \frac{U}{2d^2B} \tag{2.16}$$

The magnetron movement is a slow drift around the center of the Penning cell with the frequency:

$$\omega_- = \frac{\omega_c}{2} - \sqrt{\frac{\omega_c^2}{4} - \frac{\omega_z^2}{2}} \approx \frac{U}{2d^2B} \tag{2.17}$$

The modified cyclotron frequency can thus be described as:

$$\omega_c = \omega_+ + \omega_- \tag{2.18}$$

and forms a classical epitrochoidal trajectory in the radial plane[57]. For $\omega_+/\omega_- = 8$ this trajectory will look like figure 2.16. The first electrons that

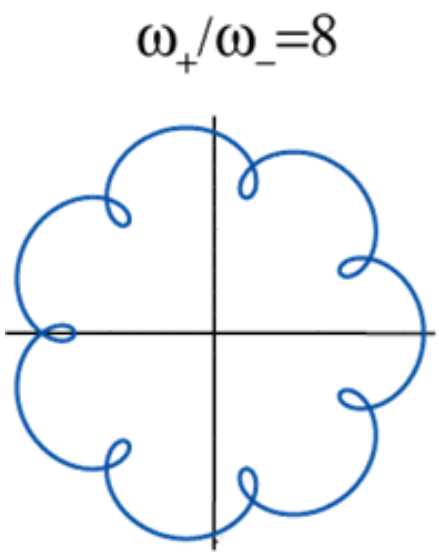

FIGURE 2.16: Classical epitrochoidal trajectory in the radial plane. Taken from [58].

get trapped are natural electrons, that occur due to ionization through background radiation. Neutral particles entering into the trap, therefore have a chance of ionization through electron collision. The electron that gets separated from the neutral particle joins the electron cloud while the ion travels towards the cathode. Ion collisions with the cathode can release additional electrons that populate the electron cloud.

More neutral particles inside the trap, i.e. a higher neutral pressure, results in more of these collisions and hence ionization happening. The ion current measured at the cathode is thus proportional to the neutral pressure. Due to this fact Penning cells have an ignition pressure that has to be reached for a stable glow discharge to occur. After the glow discharge is established, a glow discharge can be sustained at a lower pressure than the ignition pressure, since there is still a higher electron density in the cell due to the electrons from previous ionization or ion collision with the cathode. Typical pressure ranges for Penning gauges are between 10^{-8} mbar up to 10^{-2} mbar. In comparison to other vacuum gauges they are placed between thermocouples on the higher pressure range and overlap for a significant part of the operating range with hot cathode ionization gauges. Their operation spans from

intermediate, to high, and into the ultrahigh vacuum classification. The ion current I is dependent on the neutral pressure p by a power function.

$$I = c_1 \cdot p^{c_2} \tag{2.19}$$

Further details on the function and the effect that electric potential and magnetic fields have on a Penning discharge will be discussed in chapter 4, while a practical proof-of-principle on how to combine a Penning gauge with optical spectroscopy is discussed in section 3.3.

2.5 The S/XB method - Converting photon to particle fluxes

A major challenge in achieving the particle balance is the measurement of the recycling-dominated flux as a result of neutralization and re-emission of neutrals on material surfaces. The determination of atomic particle fluxes, Γ_A through passive spectroscopy of atomic lines is a well known method, which accuracy depends on the knowledge of the appropriate atomic data and the local plasma parameters [59] [60] [61]. The atomic particle fluxes can be calculated from the photon flux ϕ_A of observed electron transitions of the atom by utilizing inverse photon-efficiencies or S/XB coefficients:

$$\Gamma_A = \phi_A * \frac{S}{XB} \tag{2.20}$$

The inverse photon-efficiency consists of the collisional ionization rate coefficient S and the excitation rate coefficient X. B is called the branching ratio and is a ratio between excitation and de-excitation or radiation. S/XB is derived from calculations of the line-integrated intensity I_{tot} and the atomic particle flux entering the plasma Φ_A. Assuming a coronal equilibrium, the emission coefficient ε for a spectral line can be expressed as[59]

$$\varepsilon = \frac{B}{4\pi} n_a n_e X \tag{2.21}$$

where n_e is the plasma electron density and n_a the atomic ground state density. The line-integrated intensity over the emission region r_1 to r_2 can thus be described as [59]:

$$I_{tot} = h\nu \int_{r_1}^{r_2} \varepsilon(r) dr = B \frac{h\nu}{4\pi} \int_{r_1}^{r_2} n_a(r) n_e(r) X dr \tag{2.22}$$

Under the assumption that full ionization is reached in the emission region, the atomic particle flux can be described as [59]:

$$\Gamma_A = \int_{r_1}^{r_2} n_a(r) n_e(r) S dr \tag{2.23}$$

The particle flux can be related to the plasma density by solving the ratio of the line-integrated intensity and the particle flux for Φ_A:

$$\Gamma_A = \frac{I_{tot}}{B} \frac{4\pi}{h\nu} \frac{\int_{r_1}^{r_2} n_a(r) n_e(r) S dr}{\int_{r_1}^{r_2} n_a(r) n_e(r) X dr} \tag{2.24}$$

Under the assumption that the rate coefficients do not vary significantly in the emission area this can be simplified to [59]:

$$\Gamma_A \approx \frac{4\pi I_{tot}}{h\nu} \frac{S}{XB} = \phi_A * \frac{S}{XB} \tag{2.25}$$

The molecular flux can be calculated in a similar manner, however a study has shown for that hydrogen the molecular flux is approximately the same as the atomic flux for the predominant surface temperatures. The total particle flux can therefore be described as [60]:

$$\Gamma_{total} \approx 2 * \phi_A * \frac{S}{XB} \tag{2.26}$$

For hydrogen, the use of the Balmer series lines, in particular the H_α line at 656.28 nm, are used for ϕ_A measurements [59] [61]. The correspondent S/XB coefficients are readily available in the Atomic Data and Analysis Structure - ADAS data base for a wide temperature and density range [62]. The density dependence is shown in figure 2.17. Here the S/XB for atomic H are plotted over the plasma density n_e at five different plasma temperatures T_e. For the lower densities the S/XB coefficient stays almost constant over four orders of magnitude in density. At densities above $10^{19}\,\mathrm{m}^{-3}$ the sensitivity of S/XB increases drastically. When looking at the three different temperatures, it can be seen that there is a significant change between 10 eV and 50 eV while the temperature increase from 50 eV to 100 eV leads to no significant change.

This becomes even more obvious when plotting the S/XB coefficient over the temperature as done in figure 2.18. Here the change of the S/XB value is plotted in respect to the plasma temperature for some selected densities. The values increase drastically in the low temperature range up to 20 eV and become very robust to temperature changes above 40 eV.

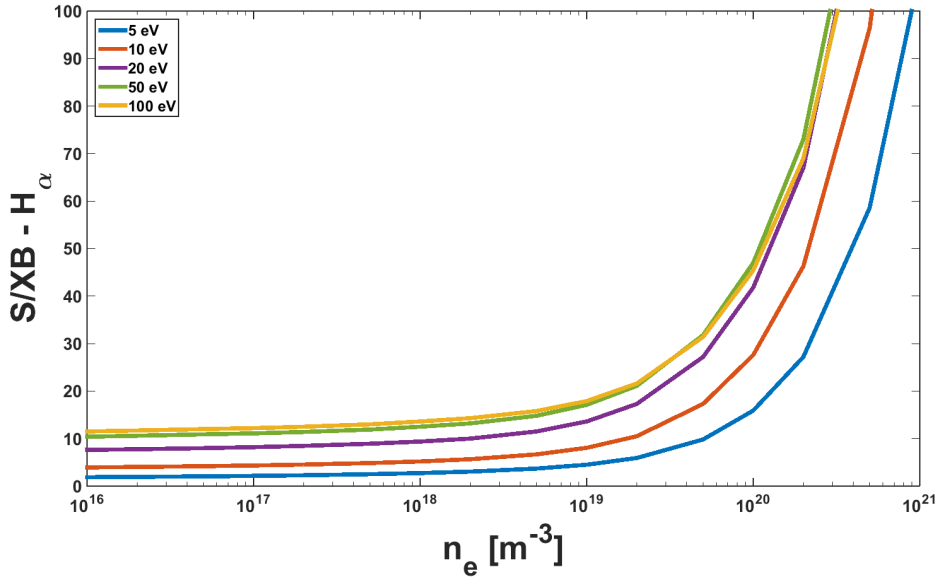

FIGURE 2.17: H_α S/XB coefficients for 5 different temperatures over the electron density taken from the ADAS data base [62].

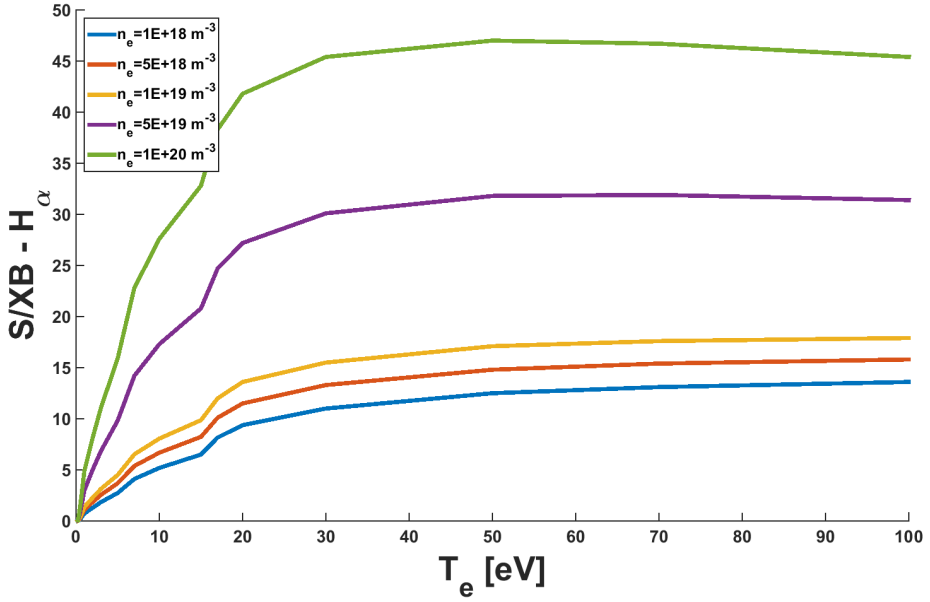

FIGURE 2.18: H_α S/XB coefficients for 5 different densities over the electron temperature in eV taken from the ADAS data base [62].

The S/XB coefficient is therefore sensitive to temperature changes between 0 and 20 eV and density changes above $10^{19}\,\mathrm{m}^{-3}$, while being robust against temperatures changes above 40 eV and densities below $10^{18}\,\mathrm{m}^{-3}$. When using the S/XB coefficient in the sensitive regime a small uncertainty in the T_e or n_e measurement can result in a large uncertainty for the calculated

particle flux.

The derivation of the atomic S/XB coefficient and its sensitivity to n_e and T_e show that this method is only valid under the assumption that the particles fully ionize in the emission region. A change of T_e and n_e can be tolerated as long as the changes are within the stable regions towards temperature and density shown in figure 2.17 and 2.18. The analysis becomes difficult for steep temperature and density gradients in the emission regions since the H_α radiation is emitted by the neutral H atoms and the location of the emission, and therefore the local T_e and n_e values at the location of the emission, can not be deduced from a line integrated measurement. This issue can be mitigated through specific assumptions based off measurements, or through simulated H_α emission locations.

Chapter 3

Diagnostic Setup and Analytic Computation

In this chapter an overview of the diagnostic and analysis methods used in chapter 5 and 6 to assess fueling and confinement at W7-X is presented in two sections. First, the diagnostics for key measurements are introduced and second the use of them in the analytical particle balance model.

The necessary diagnostics that provide measurements to fill the analytical model are discussed in the first section. A preface covering the scientific and technical data handling and storage in the Archive Data Base (ArchiveDB) is followed by subsections for each key diagnostic used in this thesis. These subsections will briefly cover the physical principles of each diagnostic while focusing on the unique properties and how they are implemented at W7-X. This includes a detailed discussion of the measurement location as well as the expected uncertainties of the measurement.

In the second section the analytical concept of the global single-reservoir particle balance will be introduced to derive the global particle confinement time τ_p. Also, the methods to infer the effective confinement time τ_p^* will be discussed.

One key measurement to investigate the helium exhaust capacity of the island divertor that was missing before this thesis work, is the partial neutral pressure measurement for helium and hydrogen. A specific diagnostic has been developed and the basics as well as the qualification is described.

3.1 Available key diagnostics

During OP1.2 over 40 diagnostics have been commissioned and operated at W7-X [63]. An overview of the key diagnostics relevant for the single-reservoir particle balance and related analysis is given in this section. During experiments, diagnostics are synchronized using a digital trigger system and

the data from each diagnostic is stored in the ArchiveDB. The ArchiveDB is the centralized data archive for all scientific and technical data collected at W7-X [64]. It was designed with quasi steady-state operation in mind and for a storage performance of 30GB/s during experiments, expected storage amount of 1.4 PB/year, a high reliability of 364 days/year, as well as maintainability and portability [64]. Since it is designed for steady-state operation, the absolute time, in nanoseconds since 01/01/1970, is used as the primary index.

Each experiment is identified by a unique program ID. While in the future it is planned to have multiple program IDs within a long discharge, currently a separate discharge was conducted for every program ID. For this reason, discharge and program ID are used interchangeably in this thesis.

The archiveDB can be accessed through an Application Programming Interface (API) and supports a Representational State Transfer (REST) model for accessing a set of resources through a fixed set of operations. It allows access to the W7-X data by using the HTTP protocol, as well as JSON and CBOR. Since the REST web services is based on standard protocols for data transport and encoding it can easily be integrated in many languages, e.g. Python/Matlab, Java, C, IDL, or LabVIEW [65].

The interferometer, with the integrated electron density $\bar{n_e}$ will be introduced first as the central measurement for the single-reservoir particle balance in section 3.2. It's followed by the two different gas fueling systems available at W7-X, which form the external sources. After introduction of diagnostics for edge temperature and density measurements, that are necessary for the determination of the S/XB coefficient (see 2.5 and 3.2.4), the filtered visible cameras used to measure the integrated photon fluxes on the PFCs will be discussed. The position of the Langmuir probe array and the He beam diagnostic that together provide T_e and n_e profiles in the divertor region are shown in a cross section of the divertor in figure 3.1. The physical divertor structure with the two targets and the baffle is pictured in thin black lines, superimposed with a Poincaré plot for two different island sizes. The position of the Langmuir probe array is illustrated by a red box, while the measurement region of the He beam is pictured by green dotted lines. This measurement region is formed by the spectroscopic observation parallel to the divertor plates intersecting with the elongation of the gas nozzles.

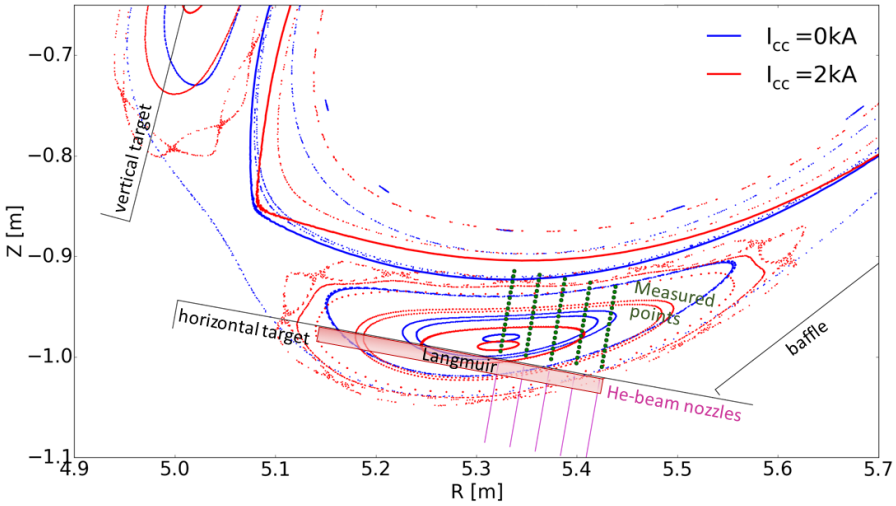

FIGURE 3.1: Poincaré plot for the standard configuration in the island divertor. Normal island size is shown in blue, large island size in red. Pink lines resemble the gas injection valves while the green dotted lines resemble the area of observation from spectroscopy. Red area marks the location of the Langmuir array. Courtesy of T. Barbui.

3.1.1 Integral Electron Density Dispersion Interferometer

The Integral Electron Density Dispersion Interferometer (IEDDI) is the key diagnostic for measuring the plasma density, in this case the line integrated electron density [66] [67]. Interferometry is based on the change in the refractive index with density that yields a phase delay. This phase delay is

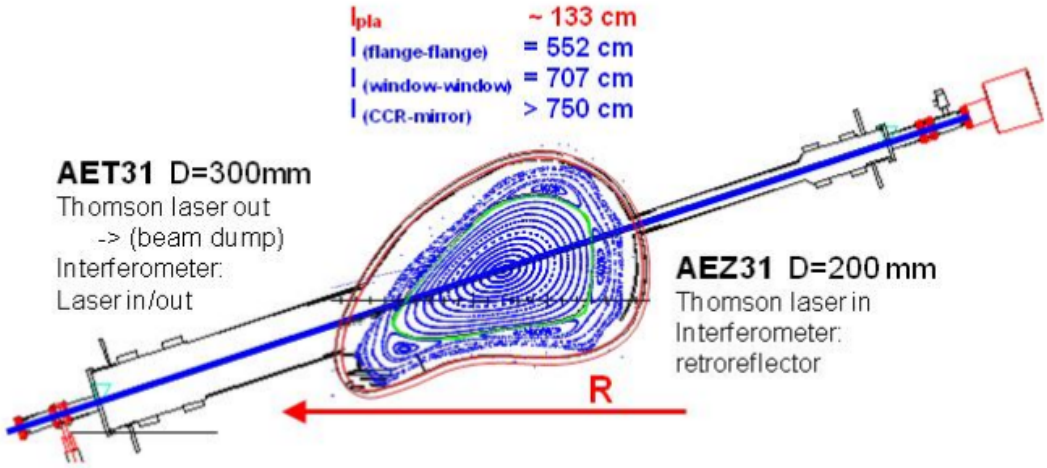

FIGURE 3.2: Cross-section through module 3, visualizing the beam path length of the IEDDI. Taken from [68].

interpreted to obtain a reliable density measurement in the plasma.

A cross section through module 3 of the measurement location of the interferometer is shown in Figure 3.2. The plasma vessel is outlined in red in the center with the blue Poincaré plot visualizing the magnetic field topology. The beam path is shown as a blue thick line going from the AET31 port to the retroreflector in port AEZ31. The outboard side of the machine is on the left, marked by the direction of the major radius R in red. A variety of path lengths are listed above the plasma vessel. The one channel of the IEDDI has a beam path length through the plasma of 1.33 m where electron densities between $10^{17}\,\mathrm{m}^{-3}$ and $10^{21}\,\mathrm{m}^{-3}$ can be measured at up to 50 kHz resulting in a time resolution of up to 20 µs. The line integrated density time traces are stored in the ArchiveDB in [m^{-2}] and have to be divided by the 1.33 m path length to get to the plasma density in [m^{-3}] [69].

Generally all currently acquired IEDDI data has a composite density error. First all density data is subject to fairly Gaussian optical and bit-noise. This is of the order of a few $10^{17}\,\mathrm{m}^{-2}$. Secondly the real-time evaluation of the density data on the Field Programmable Gate Array (FPGA) have a systematic phase dependent shift of the density around the true density. This is phase dependent, i.e. it changes as the true density changes and can therefore not be simply subtracted or averaged away. However we know from calibration measurements, that the shift is between $3-6\cdot10^{18}m^{-2}$. Given that this is an order of magnitude above the noise level, this is assumed as the general uncertainty.

3.1.2 Main Gas Inlet System

The main gas system at W7-X consists of multiple ring lines that supply gas to the different modules of the device. Besides some special valves for Argon injection or for boronization there is one H and one He valve in each module of W7-X. A fast gas injection system based on Piezo valves is used on the mid-plane on the high field side in each module to control the injection of He and H flows between 0.1 and 10 mbarl/s, or 4.9×10^{18} and 4.9×10^{20} particles per second [70]. The calibrated flow of each individual valve is available in the archive. The systematical calibration uncertainty is listed with $\pm$ 17 % while the standard deviation of a set of gas injections with the same input parameters is only $\pm$ 3 %. The total measurement uncertainty is therefore assumed to be $\pm$ 20 %.

3.1.3 Divertor Gas Box / Thermal Helium Beam Diagnostic

The second gas injection system is part of the He beam diagnostic. First the divertor gas box as an injection system will be introduced before the measurement technique for temperature and density measurements is discussed.

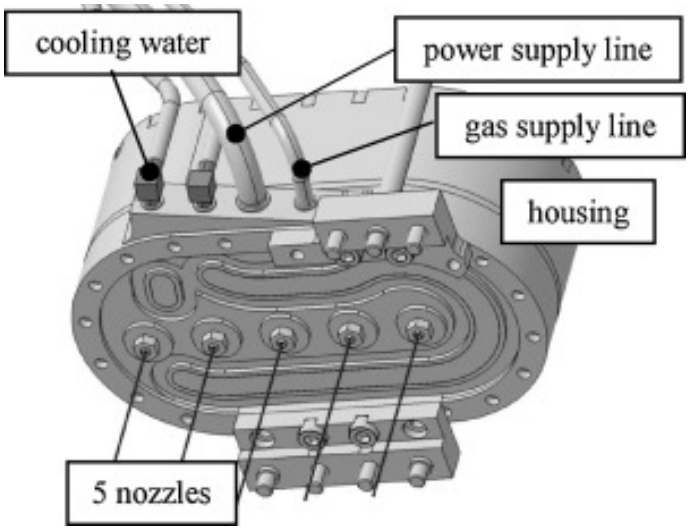

FIGURE 3.3: Valve box of the divertor gas injection system with the main supplies attached. Taken from [63, Fig. 1].

The gas injection system consists of two gas injection boxes, one at the upper divertor in HM51 and one at the lower divertor in HM30. Each injection system consists of the gas box, shown in figure 3.3, attached to the back side of the divertor module. The gas supply line is fed by a gas-reservoir which is filled to a certain pressure $p_{divertor-gas}$ before each discharge. Since the flow rates of the different nozzles are only calibrated for fully opened valves, the gas flow with partially opened valves can be estimated by the change in pressure in the gas-reservoir[71] .

The power supply line controls the five independent Piezo valves arranged poloidially with a response time of around 6 ms between input signal and valve opening [72]. One valve of each gas box is connected to a fast power supply allowing an opening time of down to 2 ms. The other valves have a minimum opening time of approximately 12 ms. The piezo valves can be controlled real-time with a feedback signal based on interferometer, bolometer, and line intensities in the divertor. A thin, $\varnothing 0.6mm$ and $\approx 10cm$ long nozzle feeds the gas at supersonic flows through the divertor plate, directly into the plasma edge, where it penetrates relatively deeply through the SOL [68]. The position of the valves is marked by pink lines that go through the horizontal divertor target in figure 3.1.

The gas box is designed for pre-fill pressures of 10 mbar up to 60 bar, enabling flow rates from 10^{18} to 10^{23} particles per second [72]. A list of the calibrated flow rates for fully opened valves in OP1.2 is shown in table 3.1. The raw data, stored in the ArchiveDB, is the reservoir pressure $p_{divertor-gas}$ as well as the voltage that is applied to each piezo valve. The calculation of the particle fluxes is explained in more detail in section 3.2.3.

During operation HM51 is used for gas fueling while HM30 is used for the He beam diagnostic to measure T_e and n_e [63]. For the temperature and density measurements a line-ratio spectroscopy system based on a collisional-radiative model (CRM) is used [73]. The green dotted lines in figure 3.1 visualize where the spectroscopic observation parallel to the horizontal divertor plates intersects with the gas released by the nozzles. The He gas flows used for diagnostic purposes are much smaller than what was typically used for fueling and are on the order of 5×10^{18} a/s [71]. This is high enough for reliable spectroscopic measurements but low enough to not disturb global or local plasma parameters.

Radial profiles from 1.5 cm up to 14 cm above the horizontal divertor target can be measured. Spectral line emission from locally-injected He and neon is channeled to multiple 20 cm and 32 cm Czerny-Turner spectrometers, allowing high spectral resolution observation of the observed He and Ne lines, as well as various visible impurity lines and Balmer series lines. The intensity of three He-I lines, $\lambda_1 = 667.8nm$, $\lambda_2 = 728.1nm$, and $\lambda_3 = 706.5nm$ is measured for diagnostic purposes. The ratio λ_1/λ_2 is sensitive to electron density while λ_2/λ_3 is sensitive to electron temperature. Systematic uncertainties derived from the atomic model were not available at this time. The uncertainty estimation is therefore based on the CRM model used at TEXTOR[74]. The uncertainties are specified as 30 % uncertainty in T_e and 10 % in n_e measurements [71].

During detachement at W7-X, low temperatures ($<< 10eV$) and high densities ($> 10^{20}m^{-3}$) result in weak or even undetectable He line emissions. This results in T_e and n_e edge measurements in the divertor to suffer from great uncertainties or being generally unavailable for detached phases. This limitation can be overcome by using Ne or a He+Ne mixture in the future, but was not available as a measurement during OP1.2.

3.1.4 Langmuir Probe Arrays

A Langmuir probe is a diagnostic used to measure the electron temperature, electron density, and electric potential of a plasma [75]. A Langmuir probe is one of the simplest plasma diagnostics to build but interpretation of the measurements is difficult. Little of the interpretation can be discussed here but an overview of the basic layout, the set-up at W7-X and the measurement parameters will be introduced.

In its fundamental form an electrode, i.e. a wire, is exposed to the plasma and its bias voltage is swept between negative and positive voltages. A negative potential will attract ions while a positive one will attract electrons. The collected charged particles can be measured as a current, based on which the plasma parameters can be derived [76].

At W7-X there are two identical Langmuir probe arrays in the upper and the lower divertor in module 5. An individual array is visualized in figure 3.4. There are 20 graphite probe tips embedded in the TDU in four groups,

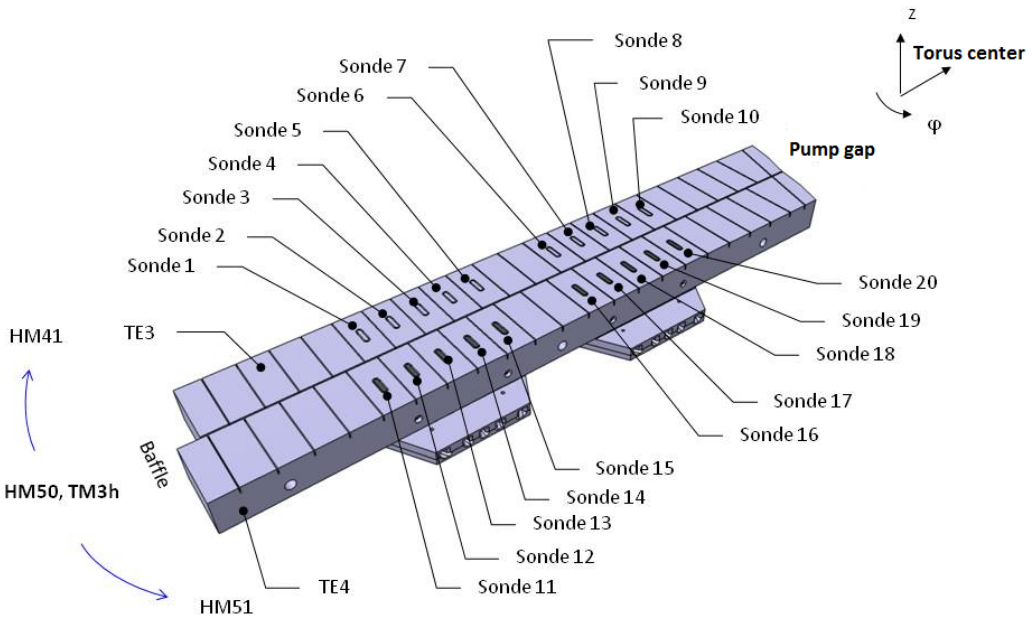

FIGURE 3.4: CAD drawing of the numbered Langmuir probes in the horizontal target of the TDU. The center of the torus is to the upper right with the pump gap starting where the CAD model ends.. Taken from [77].

forming two rows. These are located in the low iota part of the upper and

lower divertor in module 5, horizontal target elements 3 and 4. Their poloidal location in the horizontal target is also visualized in figure 3.1. The probes are 25 mm apart poloidally, but due to the shallow magnetic field incidence angle only approximately 3.5 mm radially. Because this incidence angle varies between three and six degrees depending on the probe and configuration, the tips have been faceted to always have similar effective areas and present small leading edges. The effective probe area is 1.1 - 2.3 mm^2 for all configurations under a 3 - 6°magnetic field incidence angle [68].

The Langmuir Probe has measurement channels for all 40 Probes and is available for most discharges during OP1.2, swept with 500 Hz sinusoidally. Δt for T_e, n_e, V_f will thus be 2 ms and data was recorded continuously throughout discharges. Raw data was acquired at 500 kHz resulting in $\Delta t = 2\mu s$ for I_{sat} or I_{float}. Data for the plasma parameters is currently available on request but raw data is available in the archive immediately [78]. The exact uncertainties are provided with the calibrated data and are usually within 10 % for density and 20 % for temperature measurements [79].

3.1.5 Multi Purpose Manipulator

The Multi Purpose Manipulator (MPM) is a versatile plunge system mounted at the outer mid-plane at W7-X in module 4 [80]. The MPM consists of two

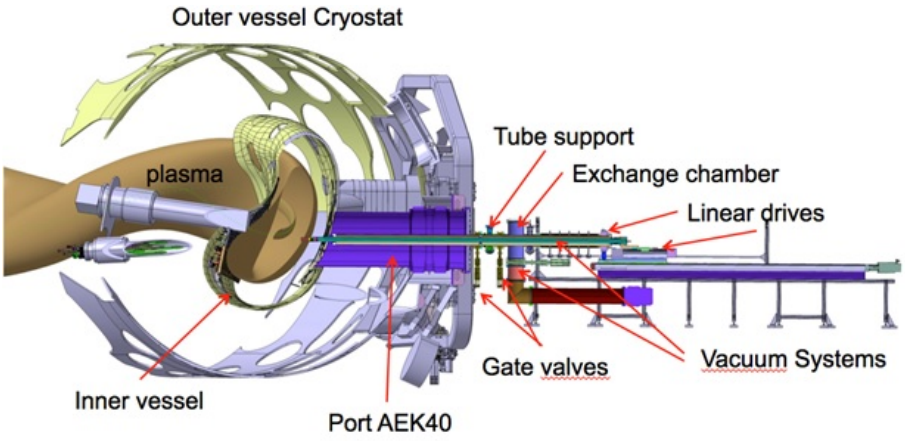

FIGURE 3.5: Overview of the MPM set up on W7-X. Taken from [81].

stacked linear drives: The first drive carries the probes from outside the cryostat to the plasma vessel wall. From that position, the second linear drive can perform fast plunges with an acceleration of up to 30 m/s^2 and a distance of up to 350 mm into the plasma. The island chain and the last closed flux surface can be crossed in all magnetic configurations [82].

The system can be equipped with currently ten different probe heads for a variety of different diagnostics or injections. Most probe heads are equipped with some sort of Langmuir probe. During the plunge the probe head continuously takes T_e and n_e measurements creating a profile that goes from about 150 mm from the PFC to about 200 mm. In the scenarios discussed in this thesis the LCFS is 227 mm away from the PFC at the MPM location. Since the MPM is mounted on the mid-plane, intersecting flux tubes far away from the divertor, the acquired data is used as upstream measurements. The profiles are also assumed to be representative for the conditions at the steel panel and heat shield PFC.

The systematic uncertainty is difficult to quantify since it is based of assumptions that are difficult to test, e.g. Maxwellian distribution, no interference between different probes on probe head, all probes are exposed to the same plasma. The signal to noise ratio was found to be below 10 % resulting in a total uncertainty estimate for $\Delta T_e = 20$ % and $\Delta n_e = 30$ % [80].

3.1.6 Filtered Visible Cameras

Each divertor module at W7-X is monitored by a set of two visible cameras. Both visible cameras are mounted in an immersion tube, together with an IR camera [83]. Each visible camera can be equipped with a narrow band pass filter $\Delta\lambda = \pm 1$nm, that will only let light of a certain wavelength pass and be detected by the camera. The filter wave lengths are chosen based on wavelengths of known atomic transitions. The cameras have been corrected for distortions in the camera and lens assembly and were calibrated with a photon flux source of known intensity. This enables the measurement of a calibrated photon flux from a specific atomic transition. The image can be separated into different regions of interest (ROI), and the photon fluxes can be integrated over those areas. The photon fluxes have been corrected for optical and geometric factors by the responsible diagnostician and a calibrated, integrated photon flux over the PFCs was provided [85].

The mounting position of the immersion tubes can be seen in a fish-eye picture of the interior of one module in figure 3.6. The set of three vacuum windows for the three cameras can be seen in each immersion tube. Their field of view (FOV) is sketched with the orange lines. The cameras on the left side are focused on the lower divertor while the ones on the right observe the upper divertor. Both FOV overlap on the heat shield. The consequences for

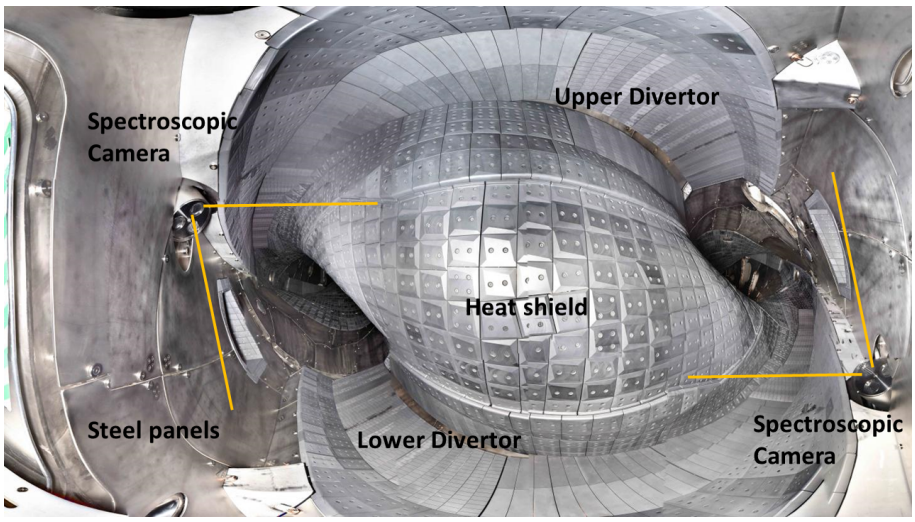

FIGURE 3.6: Wide angle picture of one module at W7-X. The immersion tubes with the three windows for the three cameras can be seen with a sketched field of view in orange. The cameras on the left are focused on the lower divertor region while the ones on the right observe the upper divertor. Taken from [84].

the calculations of the entire photon flux on the heat shield are discussed in section 3.2.4.

Each half-module is equipped with a narrow band pass filter for H_α (656.3 nm @ 2 nm FWHM) and one additional filter for the other camera. Both cameras in module 31 have an H_α filter as a stereoscopic view, H_γ (434.1 nm @ 2 nm FWHM) filters are installed in half module 10 and 21, as well as C-II (514.3 nm @ 2 nm FWHM) in 40 and 41, and C-III (465.4 nm @ 2 nm FWHM) in 11 and 20. One of the H_α filters was outside of the specifications and was contaminated by a neighboring C-II line at 658 nm. Therefore the photon flux can not be allocated to one atomic transition and one particular species. This camera will be ignored for the purposes of this work and will be replaced by an average of the other nine cameras.

For the particle balance the photon flux gets integrated over the ROI, in this case the shield, baffle, horizontal, and vertical target as pictured in figure 3.7 (a). The CAD model shown in (a) is superimposed with a frame of an H_α measurement, revealing the photon flux along the strike lines on the target. Images of the H_α photon flux measurements as used for the analysis are later shown in figure 5.10. The PFCs are introduced along figure 2.5 in section 2.1. A separate time trace of the integrated photon flux in [1/(s sr)] is provided for each camera and each ROI [85].

The signal to noise ratio is usually good resulting in an uncertainty on

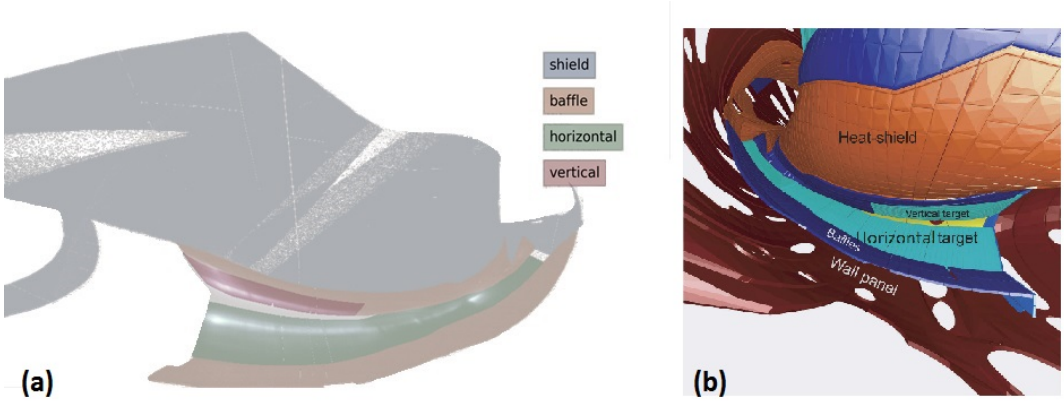

FIGURE 3.7: (a)Field of view of the filtered visible cameras superimposed with an H_α photon flux measurement. The regions of interest are color coded for the shield (gray), baffle (orange), horizontal (green), and vertical (red) target. Courtesy of P. Drewelow. (b) CAD drawing of the PFCs around one divertor element. Image (b) taken from [29, Fig. 6(a)(modified)].

the order of 1 %, but two systematic uncertainties were of concern. The first concern was that the cameras look through the SOL, where H_α radiation is predominant, twice. A suitable test would be to measure the photon flux over a port opening. If the photon flux over a port opening is significantly smaller than on a surface it would be an indication that the photon flux is dominated by the particle wall interaction and the contribution of the radiation in front of the lens is insignificant. A pair of filterscope lines of sight was identified, that view from the same port in different modules with the only difference being that one is viewing a surface, while the other one is viewing a port opening.

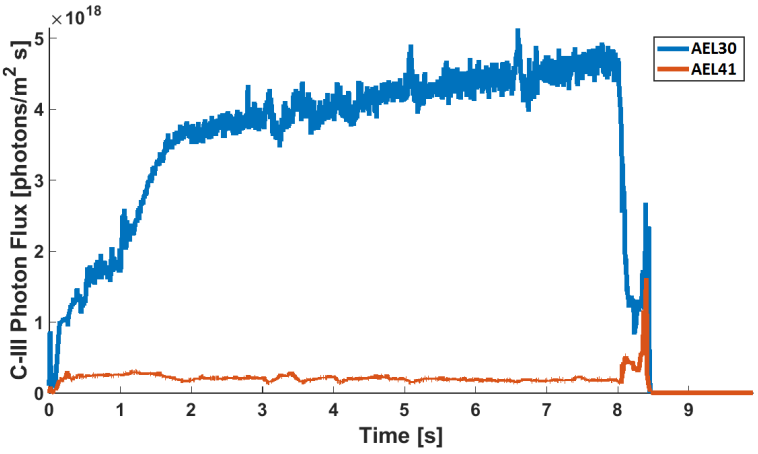

FIGURE 3.8: C-III (465.4 nm) photon flux of port AEK41 viewing a graphite surface and AEK11 viewing an open port for Program ID: 20181010.017.

However, these channels were not equipped with an H_α filter, but with a C-III (465.4 nm) filter, as shown in figure 3.8. For OP1.2 no pair with H_α filters existed. Port AEK41 is viewing graphite tiles while the line of sight of port AEK11 ends in an open port and therefore only measures the photon flux of the SOL without any surface contributions. The signal of AEK11 is only at 4 % of AEK41. The C-III photons are emitted by a higher charge state carbon, than the H_α radiation being emitted by neutrals. It is thus assumed that the surface effect would be even stronger for H_α measurements. The contribution of viewing the SOL in front of the camera, resembling an open port, is therefore assumed to be negligible and the entire photon flux is attributed to the surface of the plasma facing component.

The second concern was the incident angle of the PFC surface to the camera view angle, in particular when surfaces are viewed in a very shallow angle as it is the case for certain areas of the heat shield. When looking at a larger angle through the edge layer where the ionization occurs, one increases the line of sight length in this, and might collect more photons and therefore over estimating the actual particle flux. This effect was studied experimentally and results are shown in section 5.4.

3.2 Introduction to a global, single-reservoir particle balance

Determination of τ_p experimentally is non-trivial but insight is provided by the means of a single-reservoir particle balance. In such a single-reservoir balance the change in total number of ionized particles $\frac{dN_{tot}(t)}{dt}$ is described by the external particle sources while the outward flux is defined by the ratio of the number of particles N_{tot} and a particle confinement time τ_p. The external sources considered in this study are two gas fueling systems as well as the recycling of ions to neutrals at the plasma facing components (PFC). Since diagnostics like the interferometer measure the electron density, the particle balance is actually a sum of confined electrons. This is valid since we assume quasi neutrality for the plasma. Therefore all particle fluxes are converted into electrons per second.

$$\frac{dN_{tot}(t)}{dt} = ExternalSources - \frac{N_{tot}(t)}{\tau_p(t)} \tag{3.1}$$

Such 0-D single-reservoir models are commonly used [86][87][88] and include multiple sources, which shape and strength is device dependent. A typical particle balance for a device with a variety of fueling systems would look similar to:

$$\frac{dN_{tot}(t)}{dt} = -\frac{N_{tot}(t)}{\tau_p(t)} + f_{recy} \cdot \bar{R} \cdot \phi_{ion}(t) + f_{gas} \cdot \phi_{gas} + f_{pellet} \cdot \phi_{pellet} + f_{NBI} \cdot \phi_{NBI} \quad (3.2)$$

In this example there are terms for three fueling systems, gas injection, pellet, and neutral beam injection (NBI) as they are commonly found on fusion devices, each consisting out of the particle flux $\phi_{source}(t)$ and a fueling efficiency f_{gas}. When particles leave the confined plasma domain and hit the wall they are neutralized and are released as neutral atoms or molecules. Particles of this neutral cloud can join the neutral household or enter the SOL. There is a certain chance for the particles to penetrate the SOL and reenter the confined plasma domain. This process is also known as recycling. The recycling is expressed through the ion flux ϕ_{ion} hitting the wall and the global recycling coefficient $\bar{R}$ [14, P.180, Eq 4.75]:

$$\phi_{recy} = \bar{R} \cdot \phi_{ion} \quad (3.3)$$

Following the introduction of the PFCs based on figure 2.5 in section 2.1, the wall source was split into five different areas: Horizontal divertor target, vertical divertor target, baffle, the heat shield made out of carbon tiles on the high field side, and steel panels covering the vessel walls at the low field side. For this study the pellet and NBI system have not yet been included into the particle balance however the main gas system and the divertor gas system are treated separately.

Adjusting equation 3.2 for these conditions, τ_p can be expressed as

$$\tau_p(t) = \frac{N_{tot}(t)}{f_{Recy} \cdot \phi_{Wall}(t) + f_{main-gas} \cdot \phi_{main-gas}(t) + f_{divertor-gas} \cdot \phi_{divertor-gas}(t) - \frac{dN_{tot}(t)}{dt}} \quad (3.4)$$

with the wall flux, consisting of the wall source and Φ_{recy}, beeing

$$\phi_{Wall} = \phi_{H-Divertor}(t) + \phi_{V-Divertor}(t) + \phi_{Baffle}(t) + \phi_{Heatshield}(t) + \phi_{Steel}(t) \quad (3.5)$$

The individual inputs to the particle balance, their origin and uncertainty will be discussed in greater detail in the following subsections 3.2.1, 3.2.2, 3.2.3, and 3.2.4. The uncertainties of measurements have been discussed when the dedicated diagnostics were introduced in section 3.1. It is assumed

that all terms are governed by independent uncertainties and hence a Gaussian propagation of these uncertainties has been used. This was also done for the entire particle balance. Due to the fact that many different uncertainties are combined, the final uncertainty, especially for $\bar{R}$, gets rather large. A sensitivity study was conducted and the results are presented in section 5.4.

3.2.1 Total amount of particles

One of the key components to the particle balance is the total number of particles N_{tot} as well as its derivative. N_{tot} is being calculated from the plasma density n_e and the plasma volume V_{Plasma}. The density is measured as a line integrated value by the interferometer while the plasma volume is calculated by the Variational Moments Equilibrium Code - VMEC2000 or short VMEC [89]. The interferometer was explained in more detail in section 3.1.1. The VMEC2000 solves the magnetohydrodynamic force balance in a three-dimensional geometry. The numerical procedure of the code assumes that flux surfaces exist as a set of nested surfaces between the magnetic axis and the LCFS. For this reason effects in the SOL and also the islands can not be solved. One of the outputs of the code is the volume that is surrounded by the LCFS and is used as the plasma volume V_{Plasma}. Changes in volume due to increase in pressure within a configuration are small and within the given uncertainty.

$$N_{tot}(t) = n_e(t) \cdot V_{Plasma} \tag{3.6}$$

and

$$\Delta N_{tot}(t) = \Delta n_e(t) \cdot V_{Plasma} + n_e(t) \cdot \Delta V_{Plasma} \tag{3.7}$$

with

$$V_{Plasma} = 28.60 m^3 \pm 0.85 m^3 \tag{3.8}$$

3.2.2 Fueling efficiencies

For the particle sources, measurements only exist for the neutral particles released by the fueling system. However not all of these particles reach the confined plasma domain and can therefore be considered in the particle balance. Neutral particles might get pumped out before they can ionize or particles might ionize and get lost in the SOL. To account for these different losses each source term has its own fueling efficiency, which is defined as the fraction of particles that penetrate the SOL into the confined area, measured as

the change in N_{tot}, over the injected number of electrons e^-_{inj}. For the gas injections the difference in density was determined from the density after the injection $n_{e,2}$ and the density before $n_{e,1}$, as shown as an example in the electron density signal in figure 3.9.

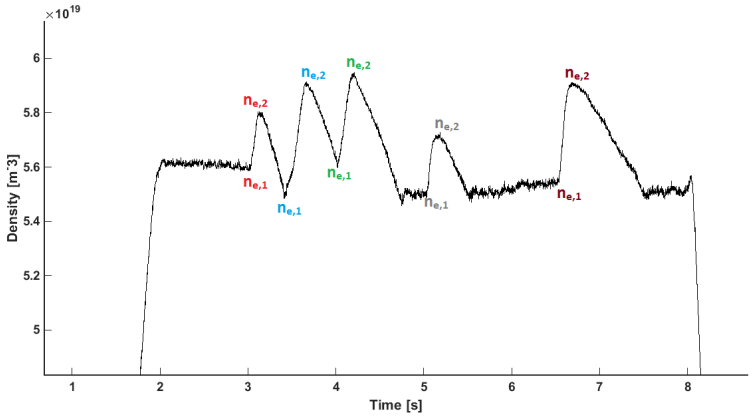

FIGURE 3.9: Electron density as a function of time for Program ID: 20181010.017. Points $n_{e,1}$ and $n_{e,2}$ for each puff used for fueling efficiency measurements are labeled.

$$f_{Source} = \frac{V_{Plasma} \cdot (n_{e,2} - n_{e,1})}{e^-_{inj}} \tag{3.9}$$

and

$$\Delta f_{Source} = (\Delta V_{Plasma} \cdot (n_{e,2} - n_{e,1}) + V_{Plasma} \cdot \Delta(n_{e,2} - n_{e,1})) \cdot e^-_{inj} + \frac{\Delta e^-_{inj} V_{Plasma}(n_{e,2} - n_{e,1})}{(e^-_{inj})^2} \tag{3.10}$$

Measuring the fueling efficiency of the recycling dominated wall source is less trivial. A time dependent version of equation 3.9 was used to analyze the plasma build up at the beginning of a discharge. Using the number of recycling electrons e^-_{Recy} instead of e^-_{inj}.

$$f_{Recy}(t) = \frac{V_{Plasma} \cdot \frac{dn_e(t)}{dt}}{e^-_{Recy}} \tag{3.11}$$

and

$$\Delta f_{Recy}(t) = \left(\Delta V_{Plasma} \cdot \frac{dn_e(t)}{dt} + V_{Plasma} \cdot \Delta \frac{dn_e(t)}{dt}\right) \cdot e^-_{Recy}(t) + \frac{\Delta e^-_{Recy}(t) V_{Plasma} \frac{dn_e(t)}{dt}}{(e^-_{Recy}(t))^2} \tag{3.12}$$

The experimental results of the fueling efficiencies will be discussed in section 5.1 and 5.2.

Pressure (mbar)	H2 (a/ms/mbar)	He (a/ms/mbar)	Ne (a/ms/mbar)	N2 (a/ms/mbar)
50	-	1.2E+14	-	-
100	-	-	2.0E+14	6.0E+14
250	3.0E+15	7.0E+14	3.5E+14	1.0E+15
500	3.0E+15	1.0E+15	5.0E+14	1.0E+15
1000	3.0E+15	1.2E+15	5.0E+14	1.0E+15
2000	3.0E+15	-	-	-
5000	4.0E+15	-	-	-

TABLE 3.1: Divertor gas box flow rates for OP1.2b, calibrated for valves AEH30, 5 and AEH51, 4. Other valves are assumed to behave similarly. Calibrated by M. Krychowiak [68].

3.2.3 Gas sources from gas injections

With the defined fueling efficiencies, the particle sources from the two gas fueling systems, $\phi_{main-gas}(t)$ and $\phi_{divertor-gas}(t)$ need to be defined as well. The particle source flow rate from the main gas system are available as calibrated standard signals and are stored in the ArchiveDB in [mbar l/s] with a measurement uncertainty of 20 %. With the assumption of the gas being at 298 K and the ideal gas law, this flow rate can be turned into neutral particles per second. With the atomic number Z as the number of electrons per neutral particle, it can be converted into electrons per second as it is needed for the particle balance.

$$PV = nRT \cdot Z \tag{3.13}$$

and for the case of H with one electron per neutral particle

$$\phi_{main-gas}(t) = n(t) = 4.8609 \cdot 10^{19} \cdot PV(t) \tag{3.14}$$

and

$$\Delta\phi_{main-gas}(t) = 0.2 \cdot \phi_{main-gas}(t) \tag{3.15}$$

For the divertor gas box, flow rates were calibrated at the beginning of the campaign as are listed in table 3.1. The flow rates are given in atoms per millisecond per mbar and simply have to be multiplied by the gas pressure which can be taken directly out of the ArchiveDB. The opening times of each valve are also stored in the ArchiveDB, as the voltage that is applied to the piezo crystal. Using the gas pressure $p_{divertor-gas}$, the correct flow rate $\phi_{divertor-gas}$ can be chosen and is used as a particle source over the opening time t, defined by the applied piezo voltage. The uncertainty for the gas flow is given as a factor of two resulting in an uncertainty window reaching from

- 50 % to + 100 % around the measured value.

$$\phi_{divertor-gas} = \phi_{divertor-gas}(p) \cdot t \tag{3.16}$$

It should be noted that the flow rates from table 3.1 are only valid for fully opened gas valves, which was only true in feed forward operation. When the system is run in density feedback the valves are only partially opened and the calibrated flow rates can not be used. However the number of released particles can still be calculated out of the pressure change in the gas-reservoir that feeds divertor gas box, assuming room temperature for the gas and the ideal gas law.

3.2.4 Φ_{wall} - A recycling dominated source term

The most challenging term in a particle balance is the neutral particle flux coming from the wall, ϕ_{wall}. In our case the wall term is dominated to 99 % by recycling, as later shown in figure 5.5 in section 5.3. Before the method is described in more detail, a short section about how particles collide with the PFCs is presented. Ions can leave the confined region either along field lines, perpendicular to them or by other processes, i.e. charge-exchange. The first two are called parallel and perpendicular transport. Section 2.1 and 2.2 describe the confinement and different losses in more detail and serves as background. The transport in the SOL is parallel within the standard range of edge densities and temperatures. This is discussed based on numerical modeling and experiments on the example of HSX in [90]. In charge exchange an ion receives an electron from a neutral particle which results in a low-energy ion and a high-energy neutral particle. The neutral particle keeps most of its momentum , causing a directed and sometimes localized particle flux on the wall.

Hydrogen ions striking the PFC may be energetically back-scattered as a neutral or be absorbed, subsequently combining with a second atom and thermally desorbing as a molecule [14, Section 1.8] as visualized in figure 3.10. On the left side a fast H ion strikes the surface. When interacting with the surface it is neutralized but keeps its magnitude of momentum and is energetically back scattered as a fast neutral atom. On the right size the H ion is first absorbed by the wall. It subsequently combines with a second atom and is then thermally released as a neutral slow molecule. This process is called wall recycling which results in the dominating wall source term in regards to the single-reservoir particle balance.

In general, the wall surface can also absorb the ion flux by bonding to free atomic or molecular bonds in the lattice. This is called an absorbing wall. On the other hand, the wall material can also release atoms and molecules if these bonds in the lattice are saturated. This is a desorbing wall situation. To explore if the wall is releasing or absorbing particles, so called wall pumping, one would have to consider a gas balance. The particle balance can not distinguish between recycling and particle release from the wall. Under the conditions for this study, the gas balance showed that the wall pumping was negligible compared to the recycling flux. The neutral particle flux from the wall ϕ_{Wall} is therefore assumed equal to the recycling flux ϕ_{recy} in this scenario and are used interchangeably. In general, the determined particle flux based on photon flux measurements does not distinguish between a recycling or a desorbing neutral. For this work the neutral wall flux will be determined spectroscopically from the H_α radiation from filtered cameras as well as the

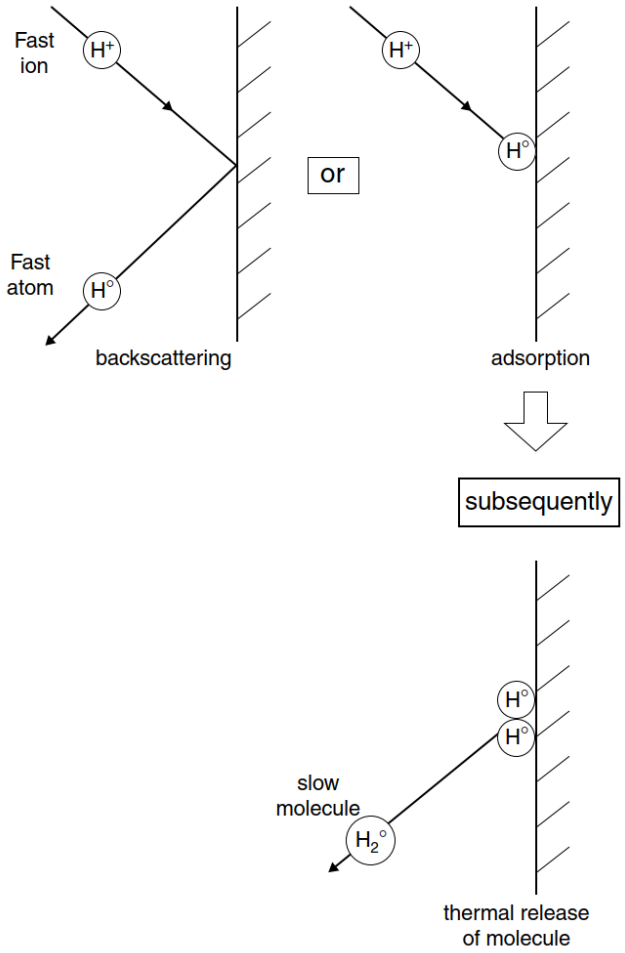

FIGURE 3.10: Recycling process of H atomic ions striking a PFC. Taken from [14, P. 39, Fig. 1.29].

Area	[$\mathbf{m^2}$]
Divertor	25
Baffle	33
Heatshield	68
Steel panels	97

TABLE 3.2: Surface areas of the different plasma facing components [77].

Filterscope diagnostic. The photon flux is then converted into a particle flux using the S/XB coefficient.

Photon flux from Cameras

H_α cameras are positioned in nine of the ten modules at W7-X. An average of the nine cameras will be used to simulate the missing camera half module 50. The camera signals are evaluated on the different areas of the PFCs as shown in figure 3.7 and are provided as integrated photon fluxes over the particular areas for horizontal and vertical divertor target, baffle and shield. While the divertor and shield can be observed in total by the camera, the heat shield is not. Obtaining line emission information from camera observations appears to be a trivial task, but when folded with the need for quantitative particle flux determination, several aspects in the experimental setup and the analysis of the data are crucial. First, the arrangement of the observations is important. For the total photon flux from the heatshield, the integrated photon flux is divided by the observed area to determine a photon flux density which is then assumed for the entire heat shield surface.

While the cameras look almost perpendicular on the target, this is not always given for the heat shield. A large angle compared to the surface could lead to a flawed measurement since the line of sight length in the SOL is increased. This effect is discussed in a sensitivity study in section 5.4. The surface areas of the different PFCs are shown in table 3.2.

Since the integrated photon flux for each camera and PFC area is given in [1/(s sr)] and calibrated over the solid angle steradian, the total photon flux for the horizontal and vertical divertor as well as the baffle is calculated as:

$$\phi_{Photon}\left[\frac{1}{s}\right] = \frac{10}{9} \cdot 4 \cdot \pi \cdot \sum H_\alpha \left[\frac{1}{s \cdot sr}\right] \tag{3.17}$$

and

$$\Delta\phi_{Photon}\left[\frac{1}{s}\right] = \frac{10}{9} \cdot 4 \cdot \pi \cdot \sum \Delta H_\alpha \left[\frac{1}{s \cdot sr}\right] \tag{3.18}$$

Here the total photon flux ϕ_{Photon} is the sum of the integrated photon flux H_α of each of the nine cameras multiplied by 4 π to account for the steradian and the photons that are being emitted in other directions and can't be measured by the camera. The missing camera module 50 is assumed as an average of all nine measured photon fluxes and is taken into account as the $\frac{10}{9}$ fraction. Since the total area of the heat shield can not be viewed by the cameras, a scaling has to be added to take this into account:

$$\phi_{Photon(Heatshield)}\left[\frac{1}{s}\right] = \frac{10}{9}\cdot 4\cdot\pi\cdot\sum H_\alpha\left[\frac{1}{s\cdot sr}\right]\cdot\frac{A_{Heatshield}}{A_{Observed}} \tag{3.19}$$

and

$$\Delta\phi_{Photon(Heatshield)}\left[\frac{1}{s}\right] = \frac{10}{9}\cdot 4\cdot\pi\cdot\sum \Delta H_\alpha\left[\frac{1}{s\cdot sr}\right]\cdot\frac{A_{Heatshield}}{A_{Observed}} \tag{3.20}$$

Filterscope

Unlike the cameras that observe a large area, each filterscope channel only observes a small spot size of ⌀5 cm. Due to this, it is a highly localized measurement and can be effected by local conditions, i.e. gas injection close to the area of observation or misalignment of tiles which cause too high or too low emissions that are not representative for the recycling conditions of the area. Four channels that view the steel panels were identified that all show comparable photon fluxes and are therefore assumed to serve as a good representation for all steel panels. Tube 28, 32, and 47 are all located on the midplane in port AEL10, AEL30, and AEL51. The view from the AEL port is from the inside of the machine onto the steel panels on the outboard side. The sight line of tube 47 in port AEL51 is close to the divertor gas injection system in that module and sees an increase of photon flux with each injection. This is an artifact and does not represent an increase in wall flux at that location. The fourth tube used, tube 45 is observing through port AEZ40 and is only calibrated within 10 % while the uncertainty for all other tubes is within 1 %. The combined uncertainty is therefore assumed to be 3.25 % An average of all four channels is taken an scaled to the surface of all combined steel panels.

$$\phi_{Photon(Steel)}\left[\frac{1}{s}\right] = \langle Filterscope_{Steel} H_\alpha\rangle\left[\frac{1}{cm^2 * s}\right] * A_{Steel} \tag{3.21}$$

and

$$\Delta\phi_{Photon(Steel)}\left[\frac{1}{s}\right] = 0.0325\cdot\langle Filterscope_{Steel} H_\alpha\rangle\left[\frac{1}{cm^2 * s}\right] * A_{Steel} \tag{3.22}$$

Determination of S/XB at W7-X

A standard method to determine atomic particle fluxes is passive spectroscopy of atomic lines, in our case for Hydrogen the H_α line at 656.28 nm. The conversion of photon fluxes takes place by means of inverse photon-efficiencies or the so called S/XB values for the observed electronic transition of the atom, as was previously discussed in more detail in section 2.5 [59] [60]. As shown in section 2.5 for the case of this study, the contribution from molecular particles can be assumed by multiplying the atomic S/XB by 2, instead of needing to rely on a D/XB coefficient that is specific to the inverse photon efficiency for molecules [61]. This assumption is valid for edge temperatures above 10 eV where the molecules ionize predominantly through dissociative excitation.

$$H_2^+ + e^- \rightarrow (H_2^+)^* + e^- \rightarrow H^+ + H + e^- \tag{3.23}$$

Here the excited H_2^+ is split into a neutral atom and an ion of which only the neutral particle can emit H_α radiation. Since there is one ion released for every neutral particle, the ion can be taken into account by multiplying the S/XB by two. At temperatures below 10 eV the dissociation process becomes more dominant.

$$H_2 + e^- \rightarrow H + H + e^- \tag{3.24}$$

In this process the molecule is split into two neutral particles that both emit H_α photons. Therefore the atomic S/XB coefficient is valid without multiplying it by two, when the dissociation process is dominant and every particle can emit H_α radiation.

The S/XB coefficient is temperature and density dependent and in its original form assumes temperature and density to be constant within the ionization length on which this line emission is only possible. In this section the edge temperature and density parameters that were present will be discussed and how S/XB changes with them. A method will be introduced how the atomic S/XB coefficient can be approximated under slightly varying T_e and n_e parameters.

The strong sensitivity to the upper density (Fig. 2.17)and lower temperature (Fig. 2.18)regime results in the need for accurate measurements of these parameters in the vicinity of the H_α emission origin. At W7-X two areas exist where edge temperature and density are measured. On the horizontal divertor target there a Langmuir probe array (3.1.4) is mounted along the target

and the He beam diagnostic (3.1.3) that can measure profiles above the target going into the plasma edge. The Langmuir probes measure right on the target, while the He beam starts measuring 1.5 cm above the target. The distance in between is linearly interpolated to create the full profile. The multi-purpose-manipulator (MPM) (3.1.5) that plunges into the SOL can measure profiles at the midplane position in module 4.

Based on these two areas, two S/XB coefficients are determined for the different areas. The combined Langmuir probe and He beam measurement is used to determine the S/XB coefficient for both divertor targets and the baffle, while the measurements from the MPM are used to determine the S/XB coefficient for the steel panels and the heat shield.

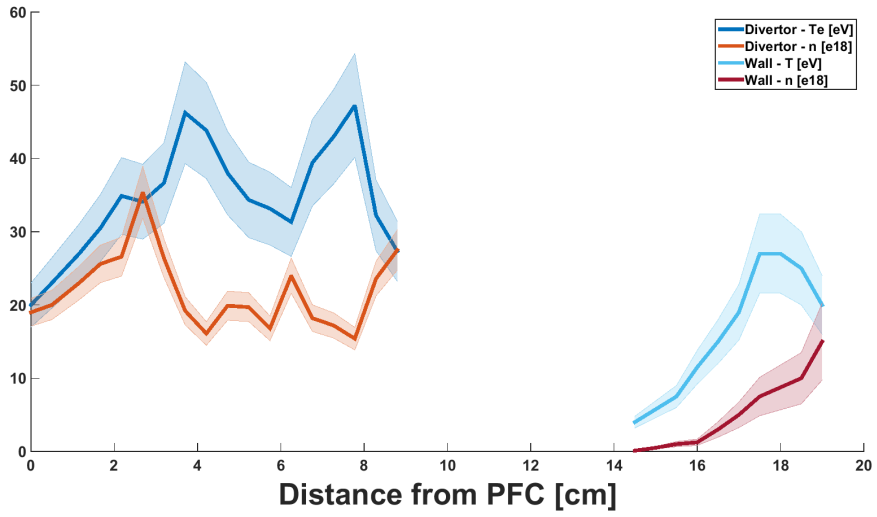

FIGURE 3.11: Edge temperature and density profiles for the divertor and wall areas. Temperatures are given in [eV] while the density is given in $[10^{18}m^{-3}]$. The LCFS is 22.7 cm away from the wall and around 8 cm away from the divertor.

The different temperature and density parameters can be seen in figure 3.11. Here temperature and density profiles that are used for the analysis are plotted over the distance from the PFC. These radial profiles are measured in front of the divertor target, starting at 0 cm, and with distance measured from the main chamber wall, in this case the steel panel at the upper midplane position. The profiles for the wall region are positioned much further out since the LCFS is 22.7 cm away from the steel panels, while it is only 8 cm above the target plates. Temperatures are shown in blue in eV while densities are shown in red in 10^{18} particles per cubic meter. In this attached scenario, the density and temperature are quite high directly on the target while the

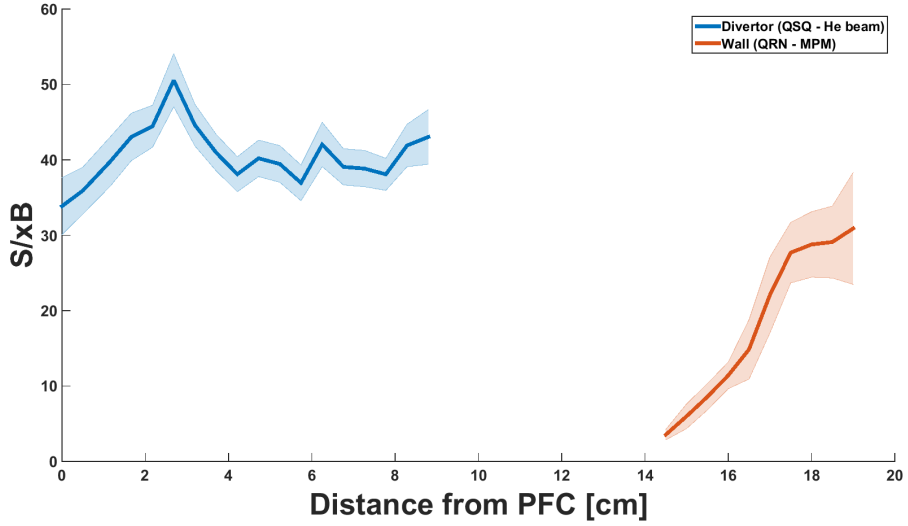

FIGURE 3.12: Local S/XB coefficients based on the local temperature and density as shown in 3.11 taken from the *Atomic Data and Analysis Structure - ADAS*.

distance between the plasma edge and the material surfaces is larger at the mid-plane where the MPM is measuring.

Therefore the density and temperature profiles start at much lower values. When using these profiles in combination with the ADAS data base to determine the S/XB values, S/XB profiles as shown in figure 3.12 can be plotted. The resulting S/XB profile for the divertor is shown in blue, while the S/XB based on the wall profiles is plotted in red. In particular for the resulting S/XB profile at the wall exhibits a constant rise due to the steady increase in T_e and n_e.

The question arises on how to determine one valid S/XB value out of the profiles which is non-trivial since it is not known where and for which temperature and density the neutral particle emitted the H_α photon. If one could localize the H_α emissions in the form of intensity profiles for the same two areas that the previous profiles were taken, one could determine the S/XB coefficient by integrating the S/XB profile by the normalized H_α emission profile. Such experimental emission profiles are not available for the discharges considered in this study. H_α profiles could also be modeled with the help of the 3D kinetic Monte Carlo neutral transport code EIRENE [91]. However, such modeling relies in the same way as the analytical derivation conducted here on the accuracy and availability of local experimental data. The analysis presented is considered as a reliable first order guidance on the S/XB values and hence the resulting fluxes as being accurate within the margins of the underlying plasma measurements. This data will in the future be used in a

3D attempt to reconstruct the fluxes using the appropriate modeling tools.

To make an assumption for the location of the H_α emission, calculations were done to determine the ionization length with the given T_e and n_e profiles. Since the H_α radiation is emitted by the neutrals, the S/XB profiles can be constrained to a relevant region by a deeper understanding of the degree of ionization α. This enables deeper insight how far neutrals can travel away from the PFC and how many neutrals are present at each point. The following procedure was established and used in this thesis.

For the calculation of the α-profiles, first the ionization rate coefficient $R(T_e(x))$ is taken from in ADAS for the temperature and density at each location. With this rate coefficient the ionization time at each step t(x) is calculated.

$$t(x) = \frac{1}{R(x) \cdot N_e(x)} \tag{3.25}$$

The velocity of the neutral particles is important in calculating the ionization length $\lambda(x)$. As discussed along figure 3.10 in section 3.2.4, there are two different recycling processes that result in either a fast atom, or a slow molecule being released from the wall. Studies at TEXTOR for similar edge parameters showed that 80 % of particles are released as molecules and 20 % as fast atoms [61]. Hence 80 % of the speed was accounted for by the slow molecules with a kinetic energy defined by the wall temperature and 20 % of fast ions with the Frank-Condon energy of 4.5 eV, resulting in a weighted averaged neutral velocity of v = 8272 m/s.

$$\lambda(x) = v \cdot t(x) \tag{3.26}$$

The percentage of particles that ionize in a spatial interval can then be calculated by dividing our interval dx by $\lambda(x)$. To get the degree of ionization α we simply integrate the percentage of ionized particles from 0 to 1.

$$\alpha(x) = \int_0^{\alpha=1} \frac{dx}{\lambda(x)} dx \tag{3.27}$$

The different plasma parameters for the divertor and the wall region result in different ionization lengths and hence degree of ionization profiles as shown in figure 3.13. The degree of ionization α is plotted in blue for the divertor and in red for the wall. Based on the previously discussed calculations we can see that in an attached scenario particles ionize almost directly on the target, while particles coming from the wall take about 3 cm to fully ionize. While the entire ionization length is comparably long, the ionization rate

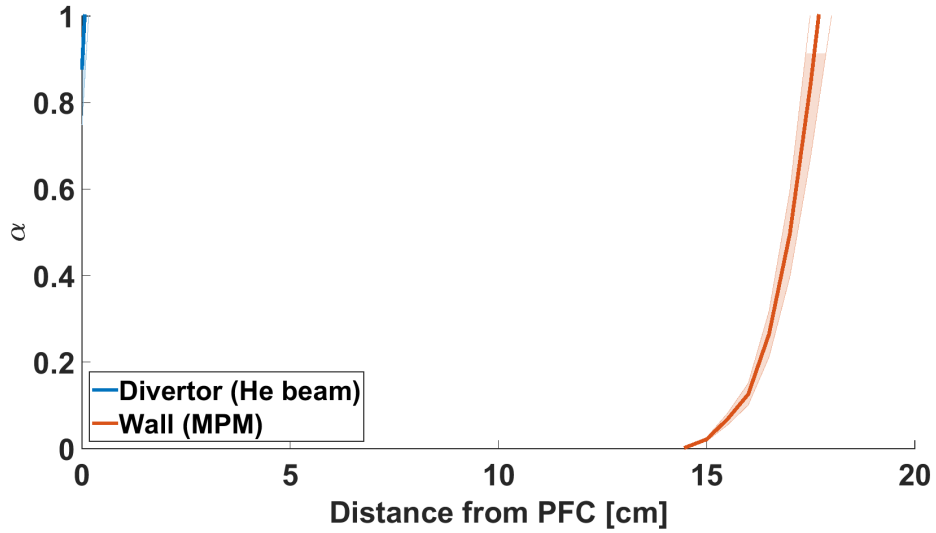

FIGURE 3.13: Degree of ionization α plotted over the distance from the PFC in blue for the Divertor target based on He beam data and in red for the wall, based on MPM data.

increases significantly along the profile, resulting in most particles ionizing within 0.5 cm.

Because of the fast ionization on the target, the surface values for T_e and n_e were taken to determine the S/XB coefficient for the divertor area. At the wall it is assumed that most of the H_α radiation is being emitted at half of the ionization length and the T_e and n_e measurements at that location were taken to determine the S/XB coefficient [92]. Following this approach different S/XB values have been identified:

$S/XB_{Divertor}$	S/XB_{Wall}
33.86 ± 3.78	22.07 ± 5.03

TABLE 3.3: The two different S/XB values that are used for this study in attached scenarios. $S/XB_{Divertor}$ is used for the horizontal and vertical divertor target as well as the baffle while S/XB_{Wall} is used for the steel panels and the heat shield.

In detached scenarios the plasma in front of the divertor target features much colder T_e in the 10 eV range with higher densities. Because of the reduced temperature, ion impact ionization as well as molecular ionization are reduced and hence the ionization length scale increases. The reduced temperatures also reduce the radial extent in which the He Beam can measure and hence larger extrapolation between the Helium beam measurement and the target Langmuir probe values is necessary. In figure 3.14 and 3.15, the interpolated plasma profiles and S/XB coefficients extracted are shown for a

detached discharge. The atomic S/XB value is still multiplied by a factor of two, since the temperatures are at the margin where the dissociation process becomes more dominant. The determined S/XB values are therefore overestimated.

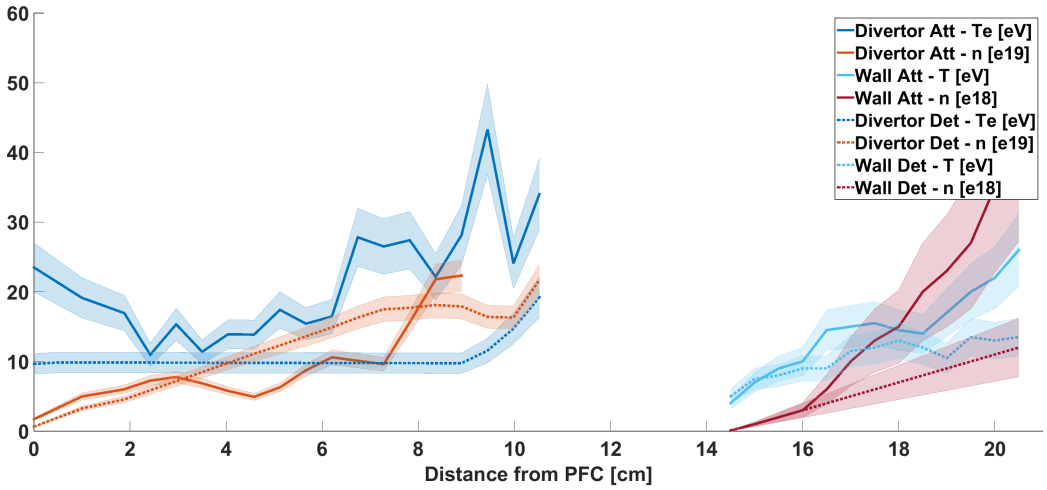

FIGURE 3.14: Edge temperature and density profiles for the divertor and wall areas in a detached scenario. Temperatures are given in [eV] while the density is given in $[10^{18}m^{-3}]$ for the wall and $[10^{19}m^{-3}]$ for the divertor. The LCFS is 22.7 cm away from the wall and around 8 cm away from the divertor. Values between the Langmuir probe and the first measurements of the He beam are interpolated

The divertor Langmuir probe at the strike line was used to infer the necessary density and temperature data and interpolated to the first available data point from the helium beam. The Langmuir probe data represent here the dominant factor, as the ionization length is defined by this diagnostic holding point on the target. However, as the plasma detaches, the Langmuir probe measurement is not necessarily representative for the actual plasma parameters at the position of the H_α line emission. Hence, this implies a level of uncertainty for the S/XB coefficient. When analyzing the helium beam, however, it is seen that at the separatrix temperatures of 10eV are measured. This supports that the S/XB range of around 15 chosen is not unreasonable. Also, the EMC3-EIRENE modeling mentioned finds a volume averaged S/XB value of 8. In conclusion, the diagnostic availability for the detached discharges is not as robust as for attached discharges, but a clear reduction of S/XB is expected based on the available diagnostics and in conjunction with the EMC3-EIRENE model.

The attached and detached phase within the same discharge are compared. When transitioning into detachment, the plasma parameters directly

above the target fall outside the measuring range of the He beam. Measurements of the He beam diagnostic, therefore start at ∼8 cm above the target. The values in between the measurements on the target by the Langmuir probes and the first measurements of the He beam are linearly interpolated. For this discharge T_e on the target is almost identical with the first He beam measurement at just below 10 eV. A flat profile without any temperature changes is therefore assumed.

The density on the target is measured at 6.5×10^{18} eV and increases to 1.7×10^{20} eV at 7.28 cm above the target for the detached phase. Even though the increase is probably not linear, it does not have a large effect on the S/XB determination, because the particles ionize close to the target due to relatively high temperatures.

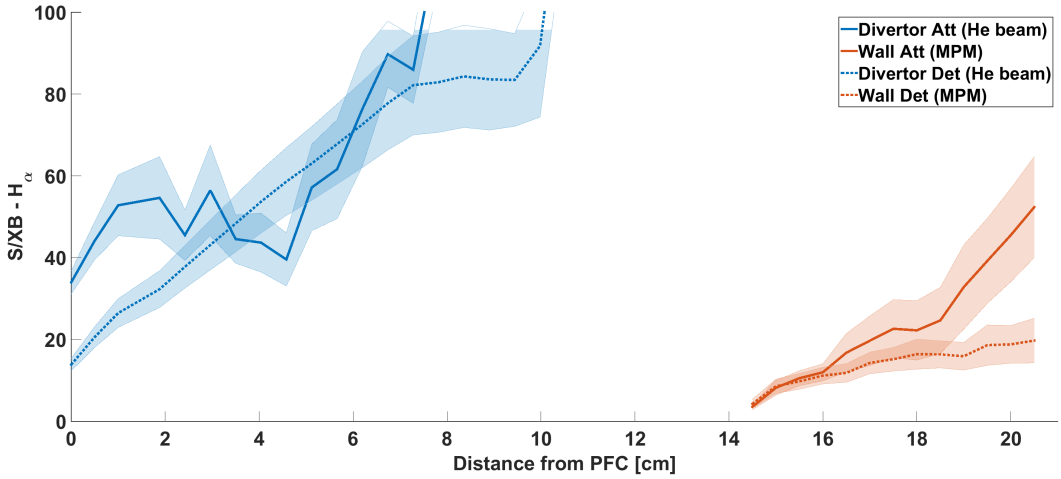

FIGURE 3.15: The two different S/XB values that are used for this study in attached scenarios. $S/XB_{Divertor}$ is used for the horizontal and vertical divertor target as well as the baffle while S/XB_{Wall} is used for the steel panels and the heat shield.

When determining the S/XB coefficients in figure 3.15, based on the plasma parameters shown in figure 3.14 the strong density dependence of the S/XB coefficient becomes visible. The divertor values are shown in blue, with the values in proximity to the wall in red. A solid line represents the attached phase of a discharge, while the dotted lines are used for the detached phase. The density dependence of the S/XB in the detached phase on the divertor target, leads to an increase by a factor of 4 over the first 8 cm above the target.

However, when considering the ionization length, and therefore the distance where neutrals and H_α radiation is present, these strong changes in S/XB become irrelevant for the analysis. The plasma parameters were combined with the rate coefficient, to determine the degree of ionization α, as shown in figure 3.16. Despite the decrease in T_e on the divertor target the

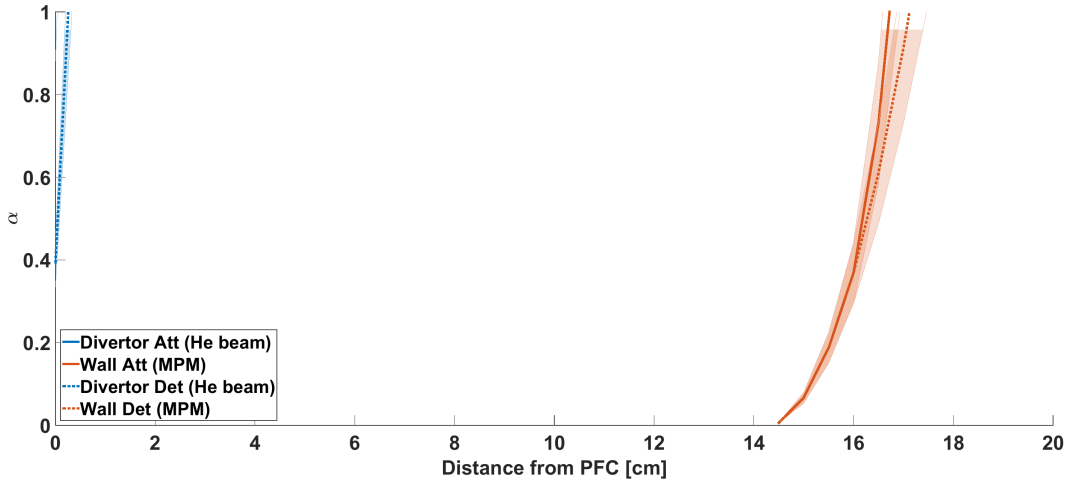

FIGURE 3.16: Degree of ionization α plotted over the distance from the PFC in blue for the Divertor target based on He beam data and in red for the wall, based on MPM data.

ionization length does not increase significantly, due to the increase in density.

The S/XB coefficients were determined at half of the ionization length, as done in previous studies [92]. For the detached discharge discussed in section 5.8, the following S/XB values in table 3.4 were determined for the different areas for the attached as well as the detached phase. Dissociative excitation is assumed as the dominant process for molecules and the atomic S/XB values are therefore multiplied by 2, which is already taken into account in the values presented in table 3.4.

	$S/XB_{Divertor}$	S/XB_{Wall}
Attached	33.98 ± 2.81	13.78 ± 3.12
Detached	15.26 ± 1.53	11.85 ± 2.28

TABLE 3.4: The S/XB values that are used for the detached discharge in this study. $S/XB_{Divertor}$ is used for the horizontal and vertical divertor target as well as the baffle while S/XB_{Wall} is used for the steel panels and the heat shield.

3.2.5 Effective confinement time τ_p^* and $\bar{R}$

Compared to the τ_p measurement described in section 3.2, the measurement of the effective confinement time τ_p^* is much simpler. τ_p^* is the decay time of a global particle-confinement related quantity rather than the confinement time of an individual particle τ_p and describes the global effective particle dwell time in the system. As a global measurement, it can not be used to

resolve local effects that arise through the 3D system at W7-X, but it stands as an effective system confinement time that defines recycling and density control [50]. If we assume a saturated wall that neither absorbs or outgases particles, external fueling is the only way to achieve a constant plasma density. If one turns off all external fueling, $\bar{n_e}$ will decay with a measured decay time τ_p^* [14, Section 4.6.3].

$$\frac{\bar{n_e}}{\tau_p^*} = -\frac{d(\bar{n_e})}{dt} \tag{3.28}$$

In practice perturbative gas injections are commonly used, and an exponential decay function is fit to the following density-related decay signal [50] [93] [94]. When using perturbative gas injections for τ_p^* measurements, care must be taken in the selection of the time interval that is used for the fit. In particular when using spectroscopic impurity emissions as a representation for their density, two different decay times can be found.

In the beginning the decay is dominated by a fast decay due to ionization, while the decay on a slower time scale represents the effective confinement time of the neutral species. When neutral gas is injected into the machine, it first increases the neutral household. In the beginning the neutral household gets depopulated by ionization on a fast time scale and pumping on a slow time scale. Particles which are ionized, leave the neutral household because they now populate higher charge states. The ionization serves as an additional sink to the neutral reservoir. This leads to a rapid decay of a neutral density related signal immediately after a gas injection. After an equilibrium is reached, another decay time can be found on a longer time scale, which actually represents the effective confinement time.

For this work the slow decay after the ionization reached equilibrium is fitted with:

$$\bar{n_e} = a \cdot e^{-\lambda * t} \tag{3.29}$$

And the effective confinement time can therefore be described as

$$\tau_p^* = \frac{1}{\lambda} \tag{3.30}$$

For the main plasma species, the effective confinement time is commonly determined by fitting the decay of the electron density. However this only applies to the main species at low impurity concentrations where $n_{mainspecies} \approx \bar{n_e}$. In the case of He as a low concentration impurity the spectroscopic lines can be assumed as a first order representative to the density. In this case the emission of the He-II line from electron collision excitation at $\lambda = 468.6nm$

can be used as the signal for singly ionized He while the He-I emission at $\lambda_1 = 667.8nm$ or $\lambda_2 = 587.4nm$ is used for the neutral He density.

When looking at the main plasma species, in this case H, equation 3.3 can be combined with equation 3.28. The change in line integrated density $\bar{n_e}$ can then be described as:

$$\frac{d\bar{n_e}}{dt} = \phi_{recy} - \phi_{ion} = \bar{R} \cdot \phi_{ion} - \phi_{ion} \tag{3.31}$$

and since

$$\frac{\bar{n_e}}{\tau_p} = \phi_{ion} \tag{3.32}$$

we obtain [14]:

$$\tau_p^* = \frac{\tau_p}{1 - \bar{R}} \tag{3.33}$$

or:

$$\bar{R} = 1 - \frac{\tau_p}{\tau_p^*} \tag{3.34}$$

and

$$\Delta\bar{R} = \bar{R} \cdot \sqrt{\left(\frac{\Delta\tau_p}{\tau_p}\right)^2 + \left(\frac{\Delta\tau_p^*}{\tau_p^*}\right)^2} \tag{3.35}$$

According to these equations a very long or no decay, $\tau_p^* \to \infty$ leads to $\bar{R} \to 1$, therefore 100 % recycling while if τ_p^* and τ_p are about equal $\bar{R} \to 0$ would correspond to very powerful pumping and zero recycling [14].

3.3 Proof-of-principle of a spectroscopically assisted Penning gauge at W7-X

Even though W7-X was only recently started, several standard and advanced diagnostics are available, as previously discussed. While the He concentration can be measured in the edge by charge exchange spectroscopy there is no diagnostic that can measure partial neutral gas pressures of H, He, and other impurity species in the divertor. Residual gas analyzers (RGA) are typically used for partial neutral gas pressure measurements. One RGA was operated at W7-X during OP1.2, taking one mass spectrum every second, but also had to be mounted close to the turbo pumps and far away from the magnetic field to avoid interference.

A diagnostic for in-situ partial pressures was missing. Penning gauges assisted by spectroscopy are a powerful tool to obtain the total neutral pressure as well as fractional neutral pressures of the main species as well as

specific impurities. This section applies the background presented in section 2.4 on a proof-of-principle during OP1.1. The results of this proof-of-principle were then refined and form the groundwork for the development of the WISP probe head in chapter 4.

For the first operational phase OP1.1, a commercial Penning gauge that was coupled with a spectroscopic observation was implemented as part of this thesis work. It was mounted on the outside of the cryostat about 2.2 m away from the LCFS. Such a system is suited to measure the total neutral pressure and the partial pressures of the spectroscopically observed components. The goal was to demonstrate that the basic principle of residual gas analysis by spectroscopy on a Penning gauge can be applied to W7-X.

The spectroscopic lines were observed with a compact CCD overview spectrometer that covered wavelengths from 350 nm to 700 nm. Atomic lines of neutral particles are used to determine the neutral partial pressures of the observed species [15]. For hydrogen or deuterium the H_α/D_α line at 656.3/656.1 nm was used. A selection of He-I lines at 587.6 nm, 667.8 nm, 706.5 nm, and 728.1 nm was used. While all lines could be calibrated for He partial pressure measurements, the 587.6 nm and 667.8 nm lines were the strongest in this set up. Since the background light from molecular hydrogen and deuterium is much larger for 587.6 nm than at the 667.8 nm transition, the 667.8 nm line was preferred for the He partial pressure measurement.

Since the main task of the system was to determine the He and H partial pressures, OP1.1 which started on August 24th 2016 with He discharges and later switched to H, was ideally suited to commission such a diagnostic. The versatile USB spectrometer enabled monitoring of residual impurity signals during wall conditioning.

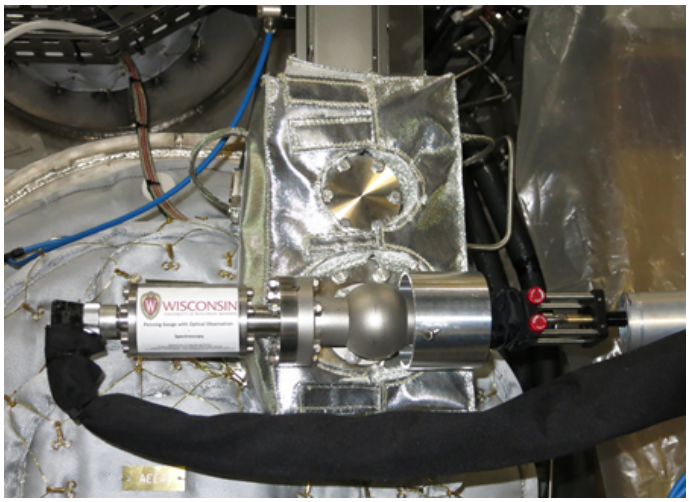

FIGURE 3.17: OP1.1 set up

A commercial Penning gauge "CF2P" by Alcatel was chosen, since it was already used successfully on TEXTOR and other devices [15]. The gauges' vacuum seals and flange had to be modified to comply with W7-X regulations. The KF flange had to be replaced with a CF flange of low cobalt steel and the lead string vacuum seals had to be replaced with dead soft aluminum to comply with bake out temperatures of 150° C.

The hardware as it was mounted on W7-X is shown in Figure 3.17. The gauge was mounted on a CF40 T-piece with a view port across from the gauge. A movable lens assembly was mounted on the view port that allowed the focal point to be positioned for maximum light intake. To protect the Penning discharge from the EC radiation from the heating system, a gasket was manufactured out of a solid copper disk with numerous 0.7 mm holes in it. These would let neutral gas pass but block radiation from ECRH and was placed between the T-piece and W7-X.

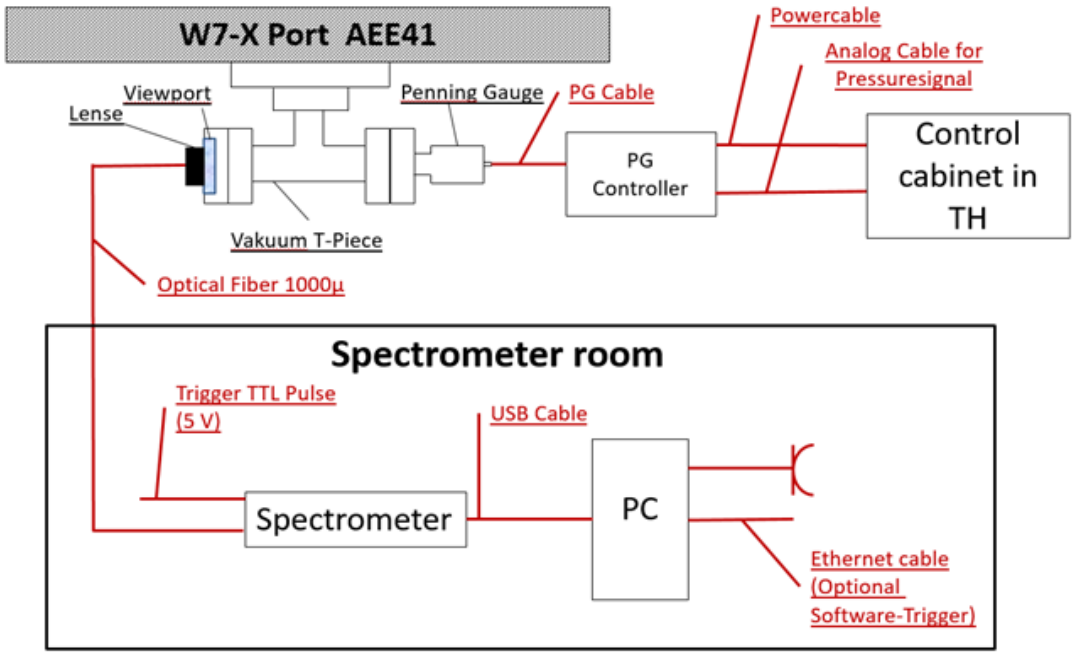

FIGURE 3.18: Schematics of OP1.1 set up

The schematics of this system are shown in Figure 3.18. The gauge was connected to a controller which has a 0-10 V analog output which was digitized in the control cabinet. The lens is attached to a long 100 m optical multimode fiber which lead to the spectrometer room where it was connected to a USB CCD spectrometer.

The commercial Penning gauge is rated for a pressure range from 10^{-7} to 10^{-2} mbar with an accuracy of ± 10 % and a 0.6 s response time. The spectrometer has a wavelength range from 500 – 1000 nm with a FWHM

accuracy of < 0.6 nm @ 633 nm and a CCD sensitivity of 160 V / (lx * s). The integration time could be set between 10 μs to 60 s. Due to the low light output of the commercial Penning gauge as well as low neutral pressures, the integration time was usually set to 15 s which meant that per discharge only one integrated spectrum could be collected. With a long integration time of 25 s, He lines could be seen down to 10^{-5} mbar and the H_α line down to 10^{-6} mbar. The total neutral pressure measurement provided by the gauge controller was constantly sampled with a sampling rate of 1 kHz. Partial neutral pressure effects during a discharge could not be measured but the results were sufficient as a proof-of-principle.

Chapter 4

The Wisconsin In-situ Penning (WISP) Probe Head

This chapter starts with a presentation of an anode design study that resulted in the final probe head design in section 4.2. The MDPX experimental set up is introduced in section 4.3 followed by the experimental results in section 4.4. A discussion about the implementation of the diagnostic at W7-X completes the chapter in section 4.5.

4.1 Anode design

The shortcomings of the OP1.1 set up of a spectroscopically assisted Penning gauge at W7-X drove the development of a new diagnostic by establishing the two major design criteria of in-situ operation and increase of light output 3.3. The OP1.1 set up has been shown to be a reliable approach, but was limited in time resolution by moderate light output. In addition, this gauge can only be mounted on the outer periphery of the device, so the vacuum time scale defines the measurement quality and interpretation. It was therefore necessary, to develop a vacuum gauge using the Penning trap principle, which can be inserted deep into the vacuum volume, i.e. directly into the divertor housing, in order to obtain full in-situ measurements. To accomplish this, the in-situ gauge must be small enough to be mounted near the divertor and edge regions, which will necessitate its use of the inherent external field [95]. The National Spherical Tokamak Experiment-Upgrade (NSTX-U) already has a custom gauge that can make fast total neutral pressure measurements located at various points around the torus, which was the starting point for this study [96].

The goal was to develop a miniaturized Penning gauge that could be operated at high magnetic fields with an Anode geometry optimized for light output and optical observation.

The three versions of the first anode design study are presented in figure 4.1. Different anode geometries are shown with the schematic on the left with

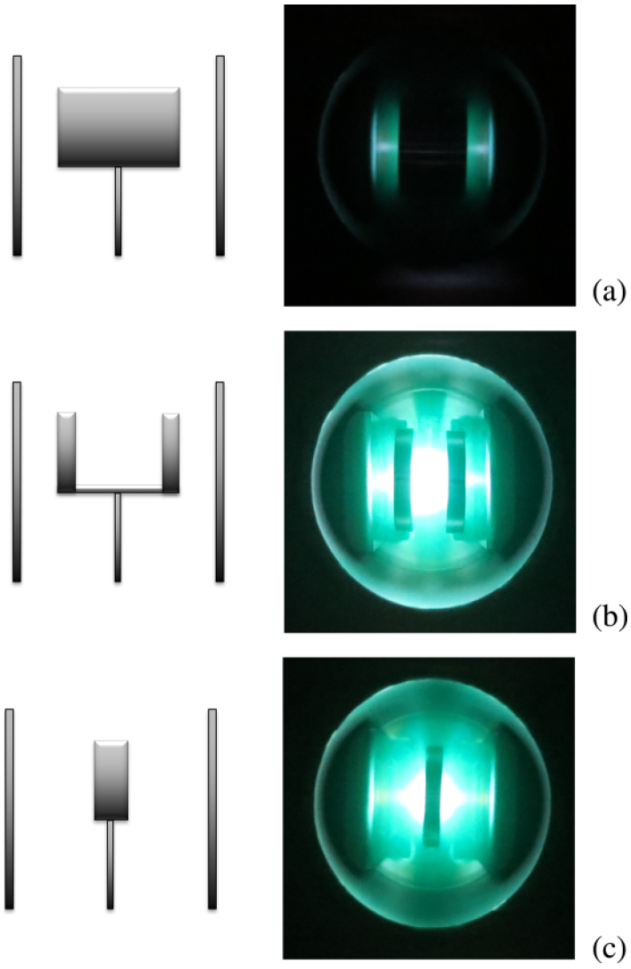

FIGURE 4.1: Anode design schematics (not to scale) and pictures taken of a He discharge of the (a) NSTX-U anode, (b) double ring anode, and (c) single ring anode. Magnetic field is horizontal for this view. Taken from [95, Fig. 2].

a picture of a He discharge on the right. The schematics on the left picture different anode designs in the center, surrounded by two cathode plates on either end. On the top is the NSTX-U anode geometry which used a long tube as an anode (a). This allowed a stable Penning discharge but also obstructed the view on the discharge which would hinder optical observation. A section of this tube was taken out for the double ring anode shown in the middle (b). This increased the observable discharge volume but came with the caveat of instabilities in the range of operation. The ring anode is shown on the bottom, which was designed with the aim of preserving the magnetic field topology of the NSTX-U gauge for stability reasons while revealing a larger fraction of the plasma volume for optical observation [95].

This study was later extended to develop the final probe head. The 70 mT field of the previous study, created by permanent magnets resting directly on the cathode plates, was not homogeneous and led to mode switching. It was replaced with larger permanent magnets that were mounted outside of the vacuum vessel and created a measured magnetic field of 250 mT at the probe head position. Another anode design, a double ring anode based of (b) in figure 4.1 with wider rings and a thinner gap, was added and all designs were compared regarding their ion current behavior and light intensity.

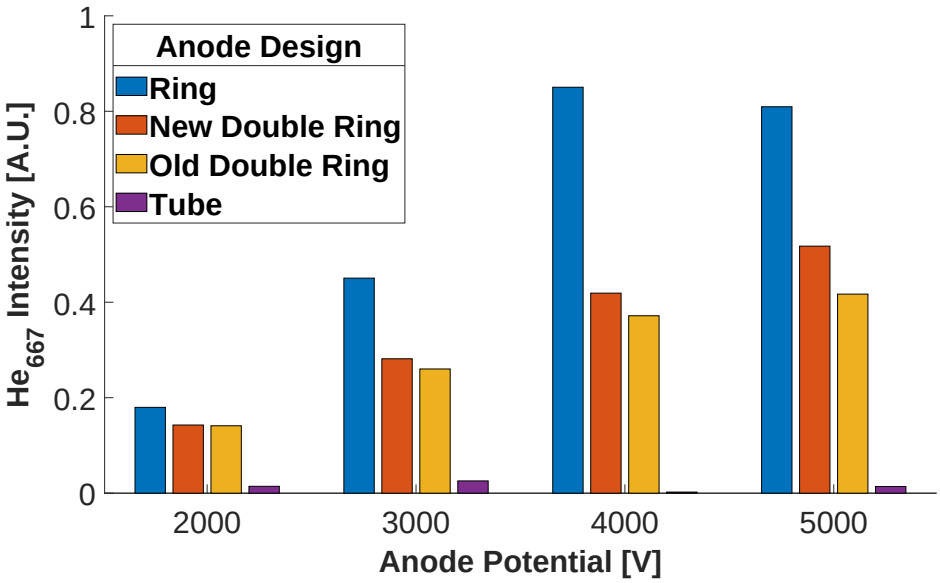

FIGURE 4.2: Light intensity of the He_{667} line with constant pressure at $T_{int} = 0.1s$ with a USB CCD spectrometer, left to right at different voltages: Ring, New Double Ring, Old Double Ring, Tube Anode.

A comparison of the four different anode designs in regard to the He-I line intensity at 667 nm at a constant pressure and with different anode potentials is shown in figure 4.2. The light intensity increases for all four anode designs with an increase in potential. The effect of the tube anode blocking the view on the main discharge volume is obvious. Every new design surpasses the photon yield of the tube anode tremendously. The ring anode was superior to the other designs in light intensity, as well as ion current behavior at every anode potential and was chosen for the final probe head design.

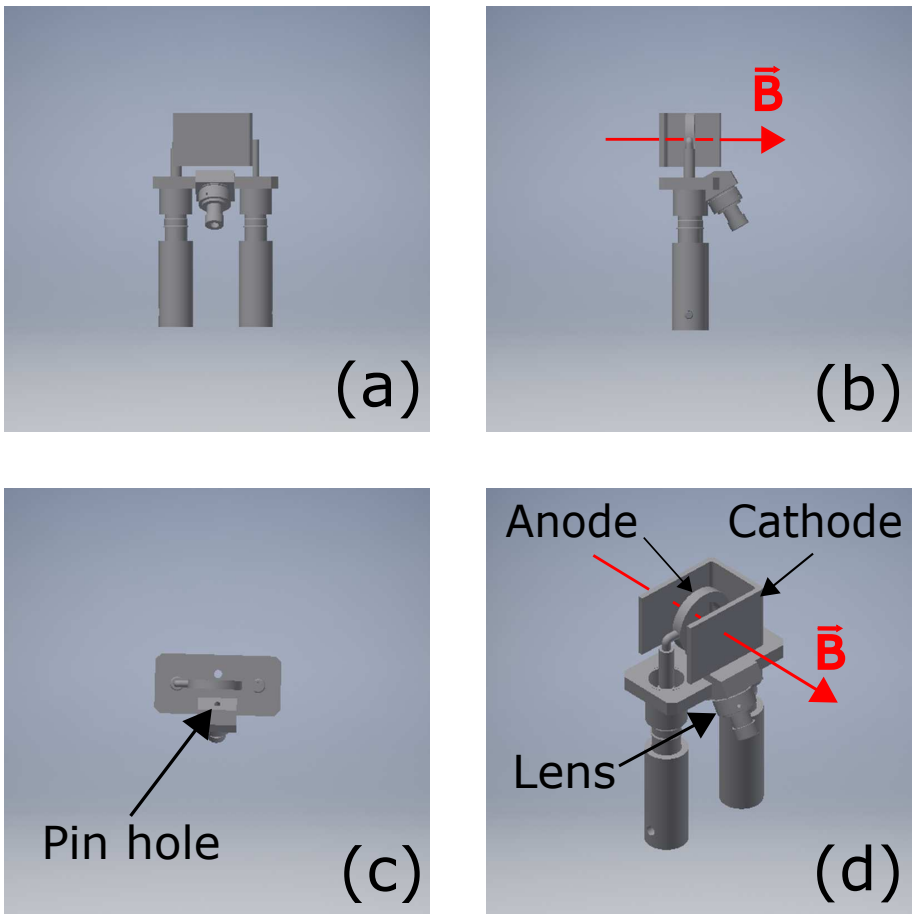

FIGURE 4.3: CAD model of WISP Probe Head showing (a) front, (b) side, (c) top, and (d) isometric view.

4.2 The WISP probe head

The WISP probe head consists of a ring anode surrounded by a cathode plate as shown in figure 4.3. The anode and cathode are mechanically connected by a base plate where a lens is mounted and protected by a pin hole. To create the quadrupole field necessary to enable a discharge the magnetic field has to be aligned co-axially with the anode as sketched with the magnetic field vector in red. The anode ring has an outer diameter of 9 mm and a 3 mm by 3 mm cross section. The cathode plate is made out of a bent plate with a thickness of 1.5 mm. The anode, cathode, and base plate are all made out of stainless steel. The electrical insulation is achieved by custom boron nitride pieces and ceramic beads. The cathode plates are 17 mm apart from each other with the ring anode mounted in the center. The anode and cathode are supported from the side to keep the bottom view clear for the optical observation.

To create a well-defined optical observation area, a combination of a pin

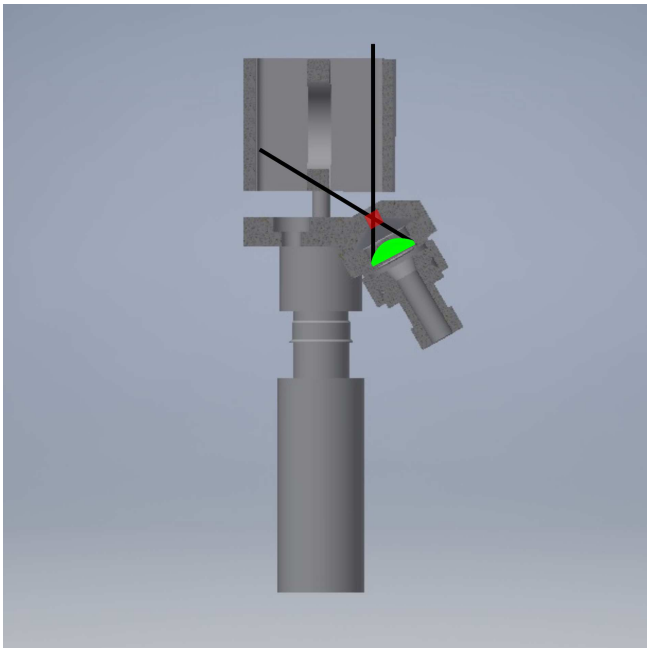

FIGURE 4.4: Picture of a cross section of the WISP probe head with the lens in green, pin hole section in red and the field of view lines in black.

hole camera with a collimator lens is used, as visualized in a cross section in 4.4. The cross section is positioned through the center of the probe head, revealing the optical set up and the field of view. The pin hole is marked in red with the collimator lens in green. In combination they form a pin hole camera with the field of view sketched in black. The pin hole camera serves two functions. The main purpose is to protect the lens from deposition, which is achieved by making the hole as deep as its 2 mm diameter. The lens was then moved further back to increase the screening effect. The second function is that the combination of the pinhole together with the lens enables a well-defined field of view. The lens was positioned in a way that the lines of sight go through the anode ring and the majority of the discharge can be observed.

Commercial Penning gauges use permanent magnets to create their magnetic field for electron trapping. This can lead to interference when the gauge is operated close to the field of magnetic confinement machines. The WISP probe head avoids this issue by utilizing the ambient magnetic field of the device, and therefore can be placed directly inside the machine as long as the magnetic field vector is co-axial to the anode ring. A potential misalignment due to tolerances in the assembly or changes in the magnetic field are discussed in subsection 4.4.5.

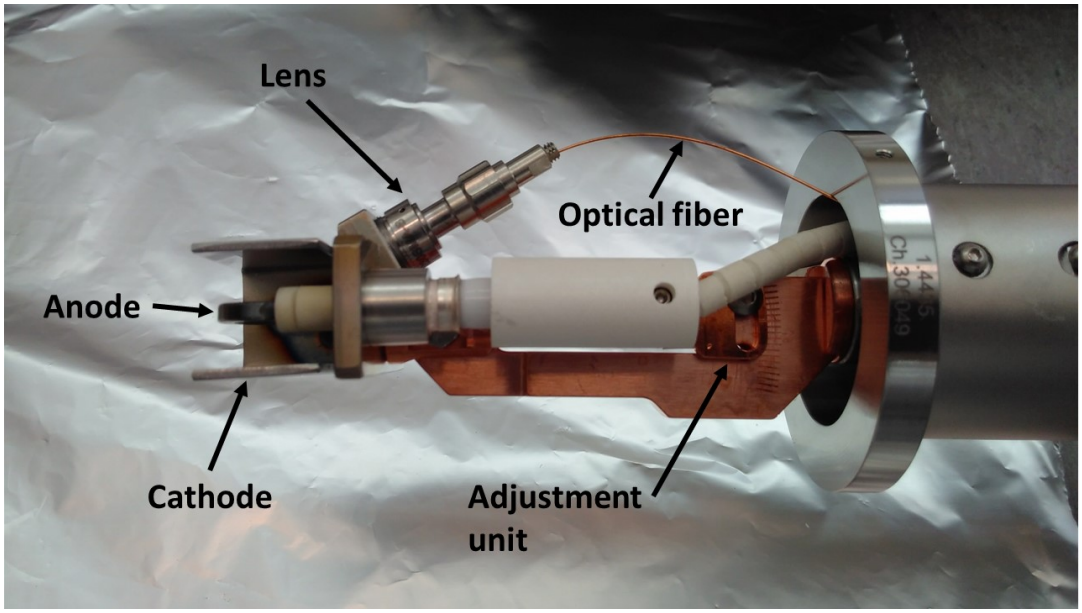

FIGURE 4.5: Picture of a WISP probe head on top of an adjustment unit to align it to the magnetic field vector.

A picture of the probe head on an adjustment unit to align it in the magnetic field is shown in figure 4.5. Here the probe head is shown as it was installed at W7-X for OP1.2b. The probe head with the anode and cathode are seen on the left with the lens and the optical fiber attached to the probe head. The copper parts shown, form together the adjustment unit, partly covered by the boron nitride insulators. The major components of the adjustment unit are two large copper pieces that can rotate around a common joint that is used to select the angle these two pieces have to each other. One piece is attached to the probe head, while the other is mounted co-axially in the immersion tube. The piece in the immersion tube can also be rotated freely. The grating seen on the right side of the adjustment unit is used to measure the selected angle. The combination of the co-axial rotation with the angular adjustment grants full flexibility in the probe head alignment.

For easier installation all connections were moved to the bottom of the base plate. In operation, high voltage is applied to the anode to create the electric field. For noise reduction the cathode plate is also insulated from the base plate, therefore also from machine ground, and has its own return. A vacuum optical fiber is connected to the collimator lens via an SMA connector and transmits the light to the spectroscopic device of choice.

4.3 Experimental set up at MDPX

The WISP probe head went through an in depth testing at the Magnetized Dusty Plasma Experiments (MDPX) at Auburn University [16]. The superconducting MDPX magnet offers the unique capability of a freely adjustable magnetic field strength between 0 and 3.5 T.

FIGURE 4.6: Picture of the super conducting magnets of MDPX in black. The two sets of magnets are separated by a large air gap housing the UHV chamber used for this study.

The MDPX device with the vacuum chamber used for this study is shown in figure 4.6. Two sets of super conducting coils, shown in black, are separated by an air gap that allows easy access to the vacuum chamber in the center of the device. The regular vacuum chamber was replaced for the systematic testing described in this thesis with an ultra high vacuum chamber based on a 6-way ConFlat cross and ConFlat components shown in figure 4.7. A miniature version of the immersion tube that was used at W7-X 4.5 is seen on the left. The 6-way ConFlat cross was held in the center of the MDPX magnet system by aluminum holders. The flanges on the front and on the right side were equipped with viewports enabling optical observation. The bellow that connected the UHV chamber to the vacuum pumping system in the adjacent room was attached on the bottom and is not visible here. The

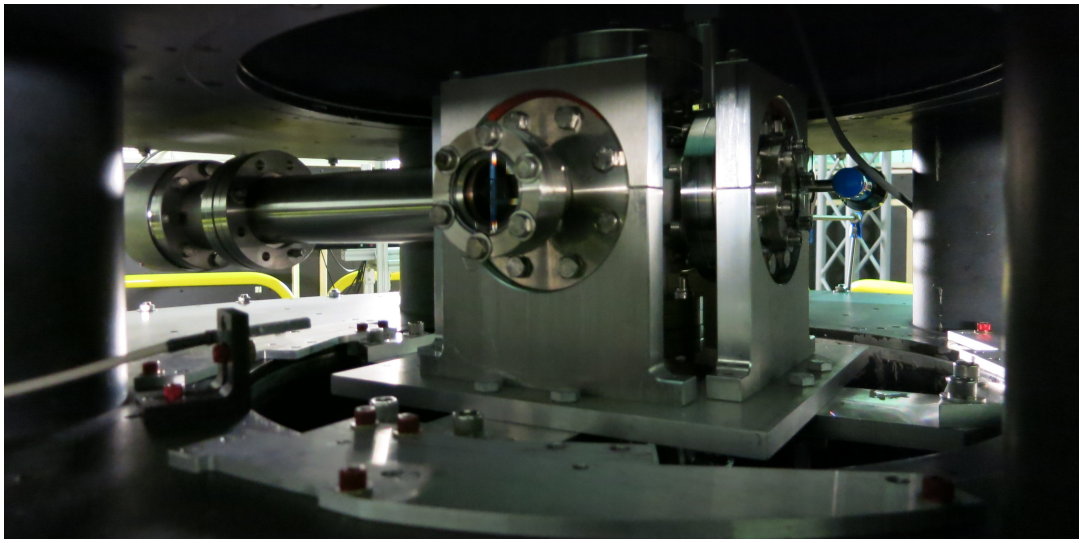

FIGURE 4.7: Picture of the UHV chamber used for this study with the immersion tube on the left, viewports in the front and on the right, as well as pressure gauges in the back. The vacuum chamber was mounted in the center of MDPX using aluminum holders.

port facing to the back equipped with valves used for the gas inlet as well as pressure gauges.

For pressure measurements and vacuum monitoring an FRG-700 Pirani Inverted Magnetron gauge together with an RGA were mounted, away from the field, close to the pump. The actual chamber was equipped with a MKS 722 B baratron (1×10^3 mbar to 1×10^{-4} mbar) and an KJLC 354 ion gauge (6.7×10^{-2} mbar to 1.3×10^{-9} mbar) measuring a base pressure of 2.6×10^{-6} mbar. All following pressure measurements were performed with the baratron since the ion gauge could not be operated in magnetic fields and was only used for vacuum verification before the field was ramped up. The baratron was positioned in close vicinity of the WISP probe head so that dynamic effects can be neglected. A He and a H gas feed were connected to the chamber, that were controlled using mass flow controllers (MFC). Two high voltage power supplies were used to apply the high voltage to the anode and to measure the ion current. Most measurements were taken with a 0 - 5 kV at a maximum of 60 mA power supply while a 0 - 2 kV at a maximum of 150 mA power supply was used to determine the maximum measurable pressure. The spectroscopy was done using a USB CCD spectrometer with an integration time of 600 ms and monitored the H_α line and four different He-I lines at 587 nm, 668 nm, 706 nm, and 728 nm.

4.4 WISP behavior in different scenarios

Results of the in depth testing at MDPX are discussed in this section. The WISP probe head was tested at 8 different field strengths (Subsection 4.4.1), at 7 different anode potentials (Subsection 4.4.2), and in H and He (Subsection 4.4.3). Different mixtures of H and He were tested (Subsection 4.4.4) as well as a systematic misalignment of the probe head to the field to determine mounting tolerances as well as effects of changes in the magnetic field direction (Subsection 4.4.5).

At W7-X a calibration was performed at the beginning and at the end of the campaign and the aging effects are discussed in subsection 4.4.6. The ion current behavior, which is the measurement proportional to the neutral pressure, can be approximated by a power law scaling. Such a power law scaling is expected for the anode current and is typical for Penning discharges [97].

$$I = f(Gas, V) \cdot p^{n(Gas,B)} \tag{4.1}$$

However, at the lower end of the operating regime in H, the currents are lower than predicted by the scaling. This was only seen at MDPX and could not be reproduced in other tests nor at W7-X. These deviations from the power law scaling are therefore seen as a unique MDPX dependent property. The cause for this deviation is still under investigation. The line intensities are proportional to the ion current.

4.4.1 Magnetic field scan

Current (Fig. 4.8) as well as line intensity (Fig. 4.9) measurements over neutral pressure were taken at eight different magnetic field strengths, starting at 0.25 T, 0.5 T and then going up in half Tesla steps, up to 3.5 T. Each curve represents a different magnetic field strength going from weaker to stronger field from left to right. The deviation of the fit in the lower pressures of each curve are clearly visible. For the 0.25 T and 0.5 T cases the lowest four to five data points are clearly above the fit while the data of the 1 T case is very close to the fit. When going to stronger fields above the 1 T a deviation at lower pressures can be seen again. However this time for the 2 T and 3 T cases the data points fall below the fit. This behavior is only seen at MDPX and could not be recorded at experiments in other devices or vacuum chambers. The

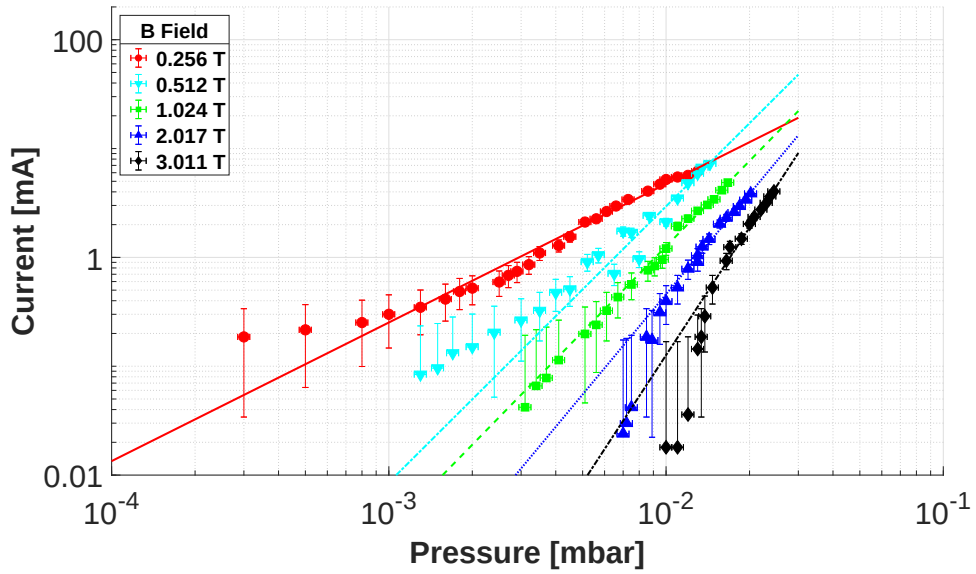

FIGURE 4.8: Measured ion current for pressure sweeps in He at various B field strengths with anode at 1500 V.

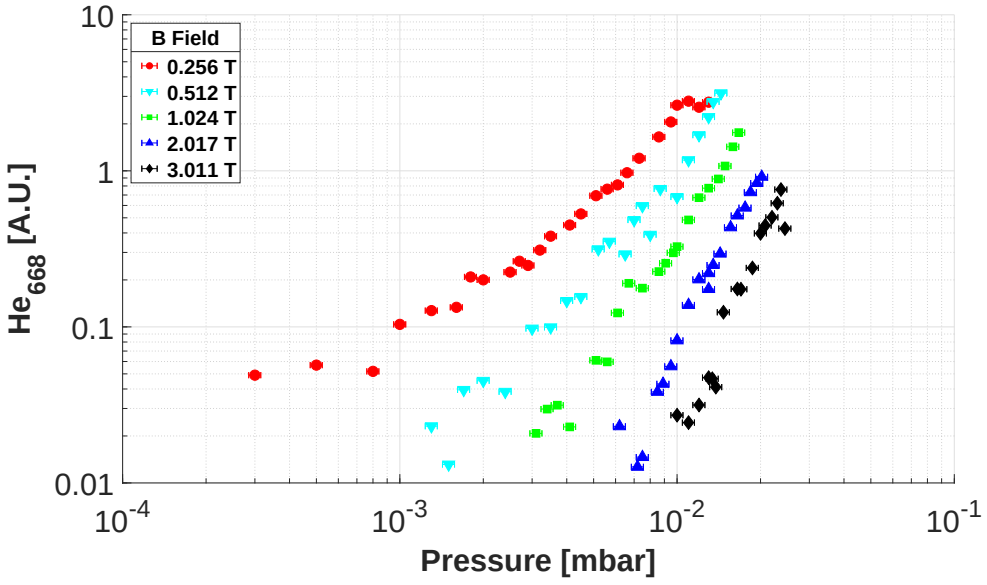

FIGURE 4.9: B field comparison of He-I (668 nm) line intensity measurements over pressure of WISP probe head in He at 1500 V with an integration time $T_{int} = 600ms$.

cause for this deviation is unknown but is considered a unique MDPX dependent property. Also it is important to note that for these data points the measurement uncertainties are high, due to small ion current levels.

Despite these deviations the power law scaling from equation (4.1) fits well with all adjusted R-square values above 0.95 with the exception of the 0.512 T case, shown in light blue, which has an adjusted R-squared value of

0.78 and is likely due to a systematic uncertainty in the gas inlet/pressure measurement of that data set in addition to the previously described deviation. The uncertainty in the current measurement increases relative to the measured current at lower currents due to a systematic uncertainty of the ammeter which is constant throughout its operating range. A more sensitive ammeter with a higher resolution below 1 mA and even below 0.01 mA could be used to increase accuracy at lower pressures. With increasing field the lower end of the operating regime shrinks, in this case for MDPX from 1×10^{-4} mbar to 1×10^{-2} mbar. While the general effect of the shrinking field was true with measurements on different devices, the MDPX data sets show the strongest effect. While the lowest achievable pressure at MDPX with a 2.5 T field was in the higher 10^{-3} mbar range, pressures below 1×10^{-4} mbar could be measured at the 2.5 T field of W7-X. The $I(p)$ curves are getting steeper while reaching comparable upper pressures at around 1×10^{-2} mbar. The data in figure 4.9 is from the same settings as that in figure 4.8, but displays the 668 nm He-I line instead of ion current. The line intensity is proportional to the ion current shown in Fig 4.8 and follows the same characteristics. The curves get steeper with an increase in magnetic field strength and the operating range shrinks. The deviation at lower pressures is clearly present in the 0.25 T case but does not seem to be as prominent as in the current measurement.

The exponent $n(Gas, B)$ of the power law scaling in equation (4.1) can be approximated as equation (4.2) for H and equation (4.3) for He based on fit parameters.

$$n = 1.8 \cdot B[T] + 0.96 \tag{4.2}$$

$$n = 0.8 \cdot B[T] + 1.45 \tag{4.3}$$

4.4.2 Anode potential scan

The WISP probe head was run at 7 different anode potentials: 1.25 kV, 1.5 kV, 1.75 kV, 2 kV, 3 kV, 4 kV, and 5 kV, as seen in figure 4.10. In this figure the ion current is plotted over the neutral pressure in H at a constant field of 1.024 T for these voltages. The pressure sweeps were conducted for each of the 7 anode potentials. The pressure curves can be described by the power law scaling (4.1) starting with the curve of the lowest potential on the right, going to the one with the highest potential on the left. The adjusted R-square values are above 0.95 for all fits, however the power law scaling (4.1) overestimates the ion current at the lower end of the operating regime below 2×10^{-3} mbar.

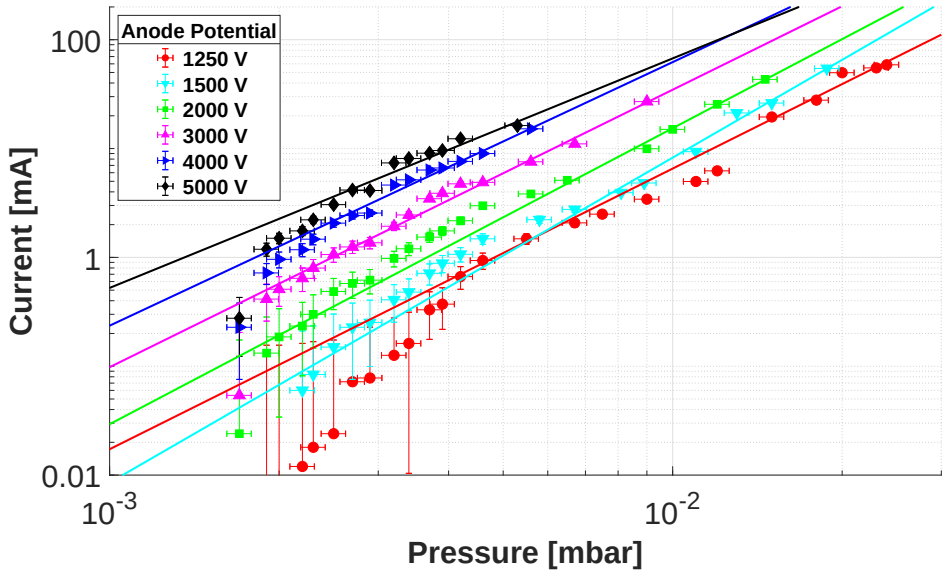

FIGURE 4.10: Ion current over pressure of WISP probe head in H at 1.024 T at different potentials.

This effect is only seen in H, the cause for this is still under investigation. The anode potential V can be used as an easy tool to shift the operating regime. A higher potential will increase the ion current, ignite a discharge at lower pressures and therefore shift the measurement range to the left.

The ion current scales linearly as shown in equation (4.4).

$$f(V) = 3.6 \cdot V[kV] \tag{4.4}$$

For high pressures a lower potential is desirable to minimize the power that is being deposited in the probe head and prevent overheating. A lower potential will generate a lower ion current at the same pressure as a higher potential. A lower potential directly lowers the power and also lowers the ion current at a given pressure and therefore decreases the input power $P = V * I$ significantly.

4.4.3 Gas dependency of ion current measurement

Like any ion gauge, the WISP gauges ion current measurement is gas dependent. At the same neutral pressure nitrogen (N) results in a larger ion current than H which is larger than He. This order is true for all ion gauges and is due to the different ionization probabilities of the various gases [98, Section 5.1.2].

For the WISP gauge, a comparison of H and He measurements at different

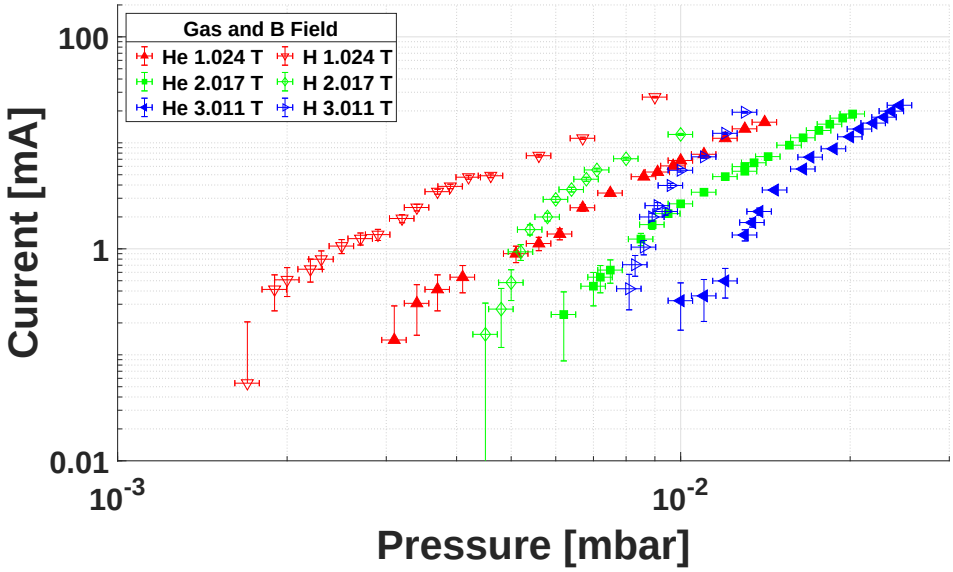

FIGURE 4.11: Comparison of H and He ion current measurements over pressure of WISP probe head at 3000 V.

magnetic field strengths is shown in figure 4.11 . While commercial Penning gauges are usually calibrated to Nitrogen and use a calibration factor for different gases, such a factor could not be identified for the WISP gauge. One reason for this is the gas dependence of the exponent as shown in equation (4.2) and (4.3). However, for a certain magnetic field strength and anode potential an approximation can be made where, depending on the case, the ion current scales between $I_H = 4 \cdot I_{He}$ and $I_H = 8 \cdot I_{He}$, however no general function between the gas species and the factor $f(Gas, V)$ from equation (4.1) could be found.

While an ion gauge can use a calibration factor, or like in the case of the WISP gauge, can be calibrated for each gas species, all ion gauges struggle with accurate measurements in gas mixtures. While the effect is negligible for trace amounts it becomes more severe with an increasing fraction of the other gases. The WISP gauge can avoid this problem by using the spectroscopic signal as a partial pressure measurement as described in the following subsection 4.4.4.

4.4.4 Partial pressure scan

For exhaust measurements, H/D and He partial pressure measurements are the most important but Ne, N, and Ar measurements can be important since they are used for diagnostic use [74] and edge cooling [99]. Possible lines

for partial pressure measurements, which were actually observed with the existing spectrometer in the gauge at MDPX, are listed in Table 4.1.

H [nm]	He [nm]	Ne [nm]	N [nm]	Ar [nm]
656.1	667.8	586.8	391.9	812.8
	587.6	640.2	469.5	751.6
	706.5	614.3	869.3	764.7
	728.1	650.7	524.9	773.4

TABLE 4.1: Observed atomic spectral lines in the visible range inside the WISP head in nm. Lines are listed from strongest to weakest.

As described in subsection 4.4.3, the gas dependency of the ion current measurement increases the systematic uncertainty of an ion gauge measurement in gas mixtures. The WISP gauge can avoid this uncertainty by measuring the partial pressures of the present gases individually. As long as all present species are accounted for, adding all the partial pressures together will result in an accurate total neutral pressure measurement independent of gas.

$$\begin{pmatrix} p_H \\ p_{Impurity} \end{pmatrix} = A \cdot \begin{pmatrix} I_{H\alpha} \\ I_{Impurity} \end{pmatrix} \tag{4.5}$$

$$A = \begin{pmatrix} Linear\ H\ response & Impurity\ cross\ talk\ into\ H\ line \\ H\ cross\ talk\ into\ impurity\ line & Linear\ impurity\ response \end{pmatrix} \tag{4.6}$$

A pressure scan of He with a constant background pressure of H to study the cross-talk between the two gas species is shown in figure 4.12. In this figure, four He-I lines and the H_α line are plotted over the He partial pressure. All He-I line intensities increase with pressure while the H_α line intensity stays constant within normal variations in the H flow from the mass flow controller.

For partial pressure measurements the lines have to be chosen carefully to avoid contamination through neighboring lines, like the 586.8 nm Ne line and the 587.6 nm He line. There can also be cross-talk from molecular hydrogen at this wavelength but negligible amount at the 667.8 nm line [15]. This could lead to an overestimation of the partial pressure, because the contributions of those neighboring lines would be accounted for the partial pressure of a different species. Since all listed He-I lines show a very similar line intensity behavior as seen in figure 4.12, any other line, except the 667.8 nm line is preferred for partial neutral measurements of He with H present. The

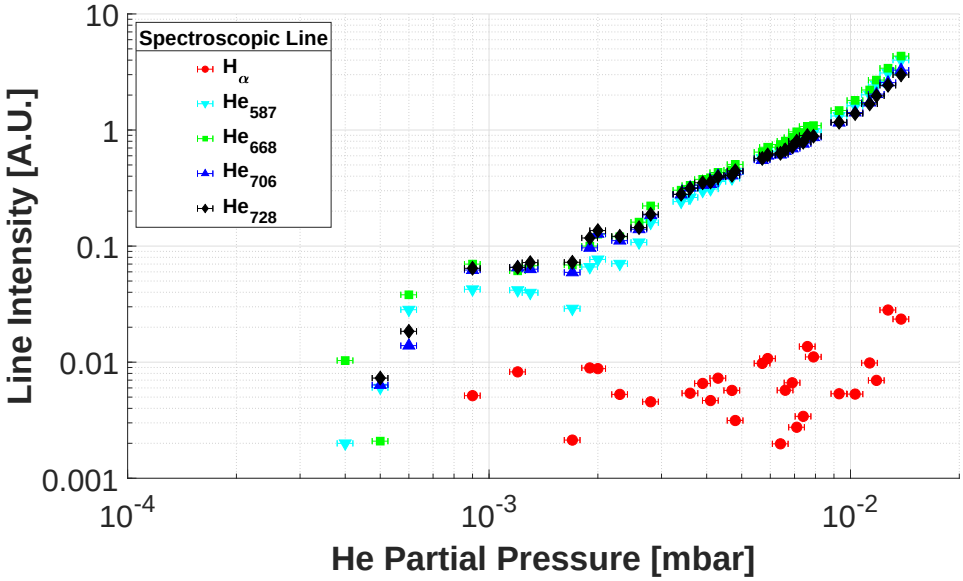

FIGURE 4.12: H_α and He-I line intensities at $T_{int} = 600ms$ over pressure of WISP probe head at 2 kV, 1.024 T and 1.7×10^{-3} mbar of H.

data presented in figure 4.12 also supports that the H_α signal is not significantly affected by He. The H_2 pressure is linear to the intensity of the H_α line directly determined from the measured spectra, as seen in figure 4.9. If the cross talk cannot be avoided by the selection of lines, it will have to be accounted for with a calibration matrix (Eq. 4.6) as shown in equation (4.5).

To empirically test for cross talk between H and He, He pressure scans were performed with different constant H background pressures as shown in figure 4.13 . When focusing on the higher pressure range above 2×10^{-3} mbar the data sets of the He-I line agree with each other very closely, despite the difference in H pressure. It can be deducted that the H partial pressure has little effect on the 668 nm line emission of He, and that it can be used as a valid metric for He neutral partial pressures in a H environment. The other He-I lines that were considered show a similar behavior. Based on this, any line intensity is proportional to the partial pressure of He and can be used for partial pressure measurements. This is valid, as long as there are no other species with line emission in a neighboring wavelength that can be spectroscopically resolved.

4.4.5 Misalignment test

In magnetic confinement machines, the magnetic field topology can change during discharges due to a number of reasons, including bootstrap currents

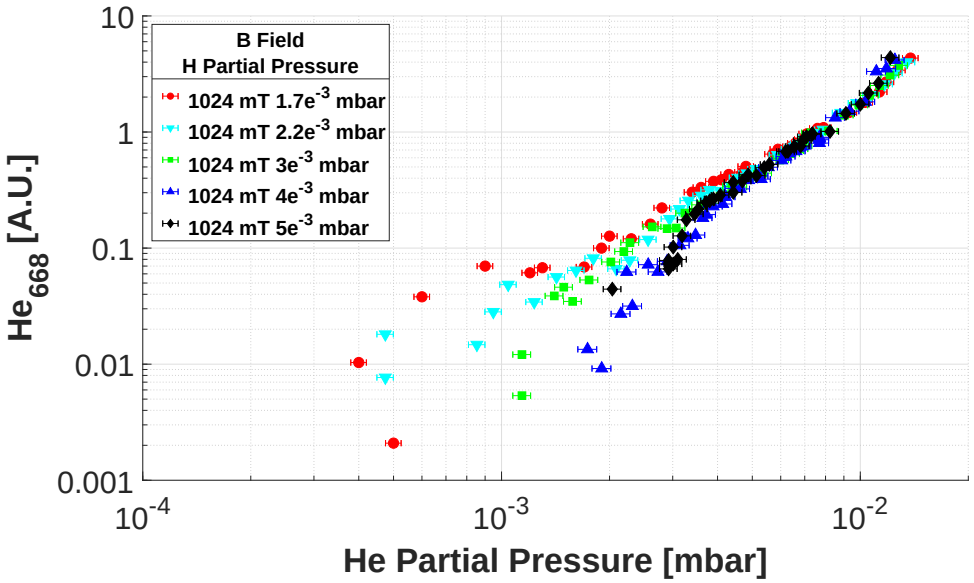

FIGURE 4.13: He_{668} line intensity at $T_{int} = 600ms$ over pressure of WISP probe head at 2 kV and different partial pressures of H.

or running a different field configuration. This can result in the magnetic field vector to not be co-axially aligned to the WISP probe head anymore. To study what change in field direction is tolerable and to be able to define mounting tolerances, a systematic misalignment test was conducted at 0°, 5°,10°, and 15°. Due to constraints with the vacuum system, these tests were done with a base pressure of 1×10^{-3} mbar. Helium was used to sweep the pressure beyond this value, but because of the residual water and air in the system, these measurements are only comparable among each other.

Therefore, measurements were repeated with these conditions for the 0° alignment. The four different angles were tested at all seven anode potentials described in subsection 4.4.2. In figure 4.14 the results at 1.5 kV anode potential are plotted, showing the measured ion current during pressure curves for the four different angles. The behavior is exemplary for all other tested anode potentials. The curves of 0°, 5°, and 10° lay on top of each other, while the 15° curve exhibits a higher ion current.

This supports that small change in alignment of up to ± 10° does not seem to have an effect on the ion current measurement while the current at 15° increases by a factor of about 2.4. When changing the magnetic field direction relative to the probe head, the plasma column (Fig. 4.15) inside the ring anode follows the tilt of the field. The shape of the column is defined by the trapped electron cloud and is a result of the electron movement described

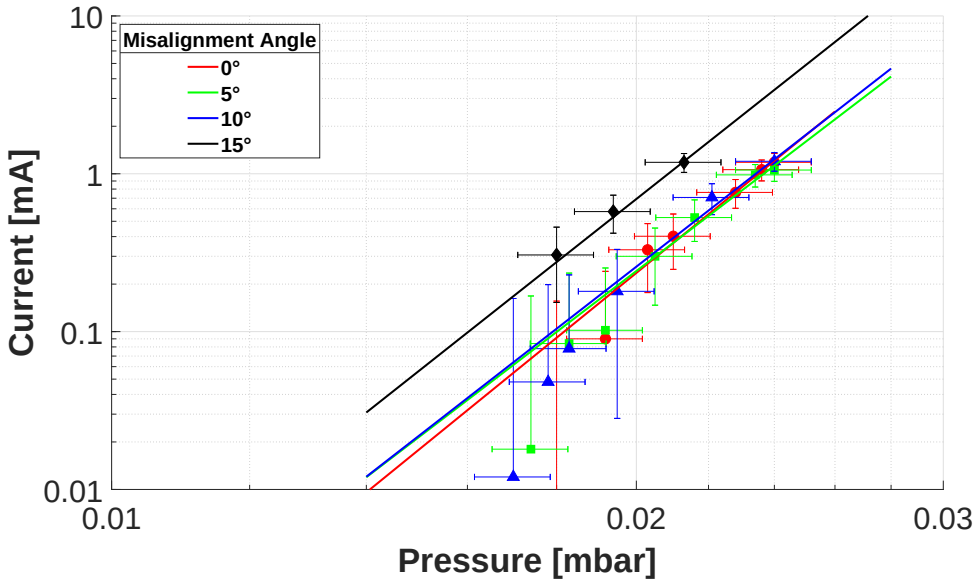

FIGURE 4.14: WISP probe head at 1.5 kV and relative misalignment of 0°, 5°,10°, and 15° to magnetic field vector.

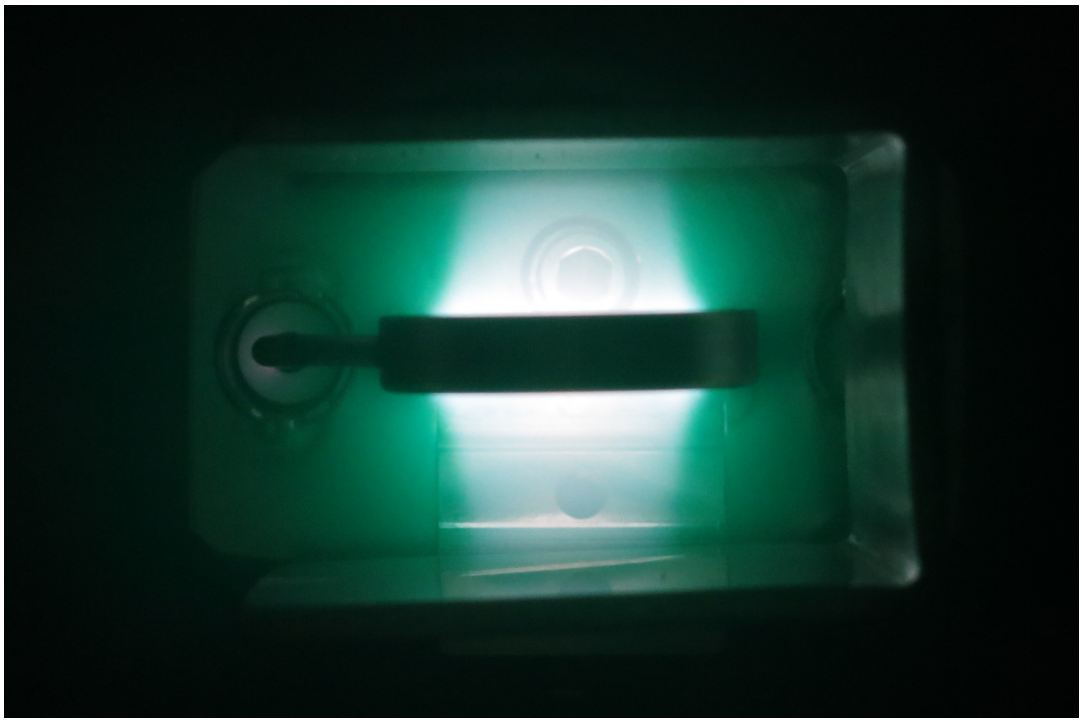

FIGURE 4.15: Picture of a the plasma column inside the anode ring in He. The opening of the pinhole camera can be seen between the anode and the lower cathode plate.

in section 2.4. At 15° the plasma column is tilted so far that it touches the anode and brings the contact spot to a glow. The glowing metal leads to secondary electron emissions, which is a likely reason for the increase in ion current.

4.4.6 Aging

Penning gauges are known to deteriorate over time, making a re-calibration or an exchange of the anode and cathode necessary. Since the WISP probe head itself is cheap and anode and cathode are welded in, it is more cost effective to change the entire probe head if necessary. When using a new probe head, the inside of the anode ring has some initial roughness to it that the plasma slowly polishes off. This was observed through the release of sparks in the first minutes of running a new probe head. This effect can be minimized by polishing the anode ring during manufacturing, however it is recommended to run the probe head for 5-10 minutes at a relatively high pressure before calibrating it. A non polished probe head will show a higher ion current than a polished one. If calibration is done before this pre aging process, it will quickly be invalid.

To study the effect of long term operation on the probe head, multiple in-situ calibrations (Subsec. 4.5.3) were performed at W7-X throughout the operation phase 1.2b [100]. While the gauges were running throughout an entire runday, the pressure was only high enough to enable a discharge inside the probe head and measure the ion current during plasma discharges, but not during the intermittent times. The standard neutral gas calibration

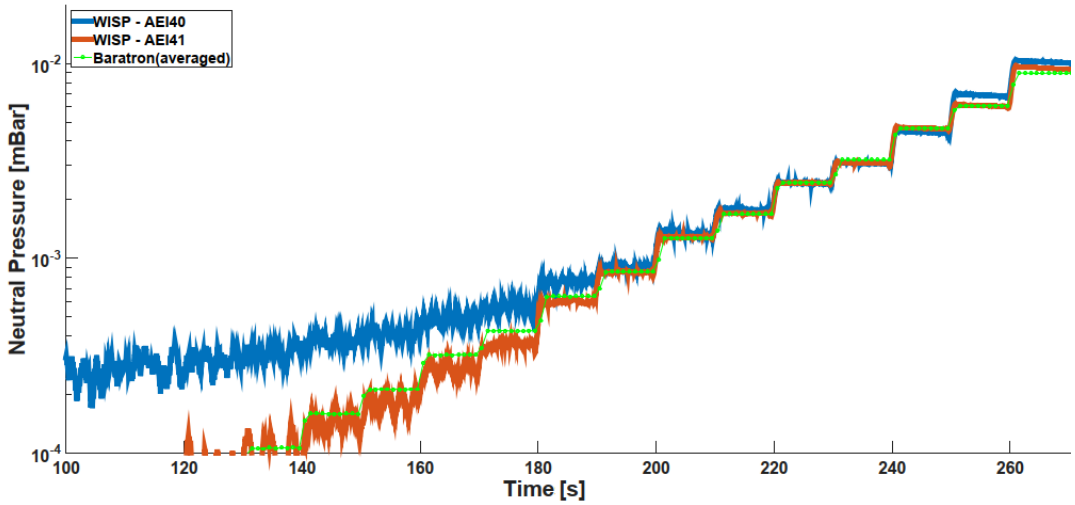

FIGURE 4.16: Pressure calibration curve that was conducted at the end of the campaign (ID: 20181010.001). The commercial baratrons serve as a reference that the other neutral gas gauges are calibrated against. In this plot the WISP signal is calibrated to the same calibration curve that was conducted at the beginning of the campaign (ID: 20180703.507).

program at W7-X, in this case from the end of the campaign is shown in figure 4.16. The calibration procedure will be discussed in more detail in subsection

4.5.3. The WISP signals from port AEI40 and AEI41 have the calibration factor from the very first calibration of the campaign applied, but still agree with the pressure measured by the baratrons. The WISP gauge still measures the correct pressures and therefore was not affected by a significant aging throughout the 127 minutes of measurements. The calibration from the beginning of the campaign was still valid at the end. The noise and the offset in AEI40 at lower pressures are due to the ammeters used and will be replaced by more sensitive ones for future campaigns.

4.5 Successful implementation at W7-X

At W7-X the WISP manometers were mounted at three positions in module 4, as shown in figure 4.17. Due to the easier removal of the probe head for maintenance purposes, a plugin design based on the design for the hot cathode ion gauges [101], was chosen. One of these immersion pipes was mounted in the top divertor pump gap (AEI41), one in the bottom divertor pump gap (AEI40), and one on the midplane (AEE41), allowing a good poloidal coverage in the module.

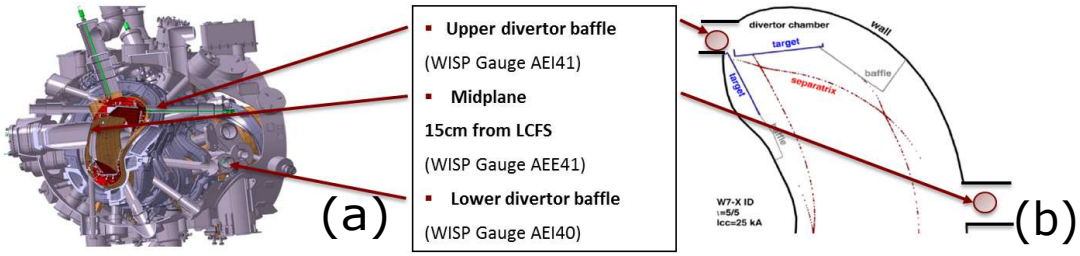

FIGURE 4.17: (a) Cross section of module 4 of W7-X with the three mounting positions of the WISP gauge. (b) Cross section as a sketch with the plasma facing components and the relative positions of the WISP gauge. Sketch (b) based on a graphic from reference [32, Fig. 1].

4.5.1 Setup of assembly

The plugins were mounted on DN63CF flanges and can be split into three main components. The actual probe head space in the front, an immersion tube which holds the probe head in place and provides the infrastructure, and an interface section which also serves as a vacuum barrier. Everything on the vacuum side is covered by stainless steel components with gaps < 0.7 mm between parts to allow pumping but shield from electron cyclotron

resonance heating (ECRH) stray radiation. To reduce the amount of noise in the signal of the current measurement, both the high voltage anode and the ground cathode return were completely insulated from the machine.

Probe head space

The probe head space is confined by a 100 mm by ⌀58 mm stainless steel cylinder. The front plate is designed as a hole diaphragm (Fig. 4.18) made up

FIGURE 4.18: Picture of a the hole diaphragm on the front plate of the probe head space

of 75 ⌀0.7 mm holes that block out EC radiation from ECRH but allow a gas exchange. The probe head is mounted on an adjustment unit, introduced in section 4.2, to be aligned to the magnetic field of the standard configuration. The maximum directional change of magnetic field between different configurations is 2.5° and is therefore well within the misalignment tolerances as discussed in subsection 4.4.5. The adjustment unit was manufactured out of copper to allow for a better heat transfer from the probe head to the immersion tube.

Immersion tube

The immersion tube holds the probe head in its designated place and guides two copper wires and the fiber over 2.2 m from the feed-through, through the

cryostat, to the probe head space. The copper wires are insulated by ceramic tubes, ceramic pearls, and custom boron nitride covers at the screw joints. The center tube is at atmospheric pressure and could later be upgraded for active water cooling. This tube is surrounded by fins for stability with slits that guide the fiber and wires as seen in figure 4.19

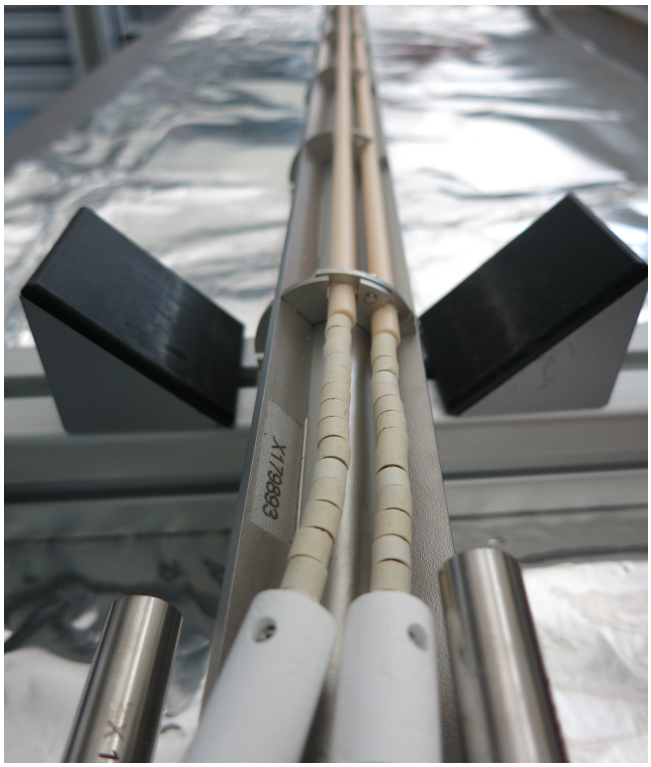

FIGURE 4.19: Picture of the inside of the immersion tube without the surrounding ECRH cover. The fins as well as the insulated copper wires can be seen from the feed-through looking towards the probe head space.

Interface

The DN63CF flange serves as the vacuum barrier and has two electrical feed-throughs, one for the anode potential and one for the cathode return, which are both rated for 5 kV. A DN16CF flange was added for the SMA fiber feed-through. On the air side the two electrical feed-throughs are connected to an SHV connector.

4.5.2 Spectroscopic set-up at W7-X

On the air side a 1 mm fiber is attached to the DN16CF fiber feedthrough, which guides the light of the WISP discharge into a Filterscope [102] in the

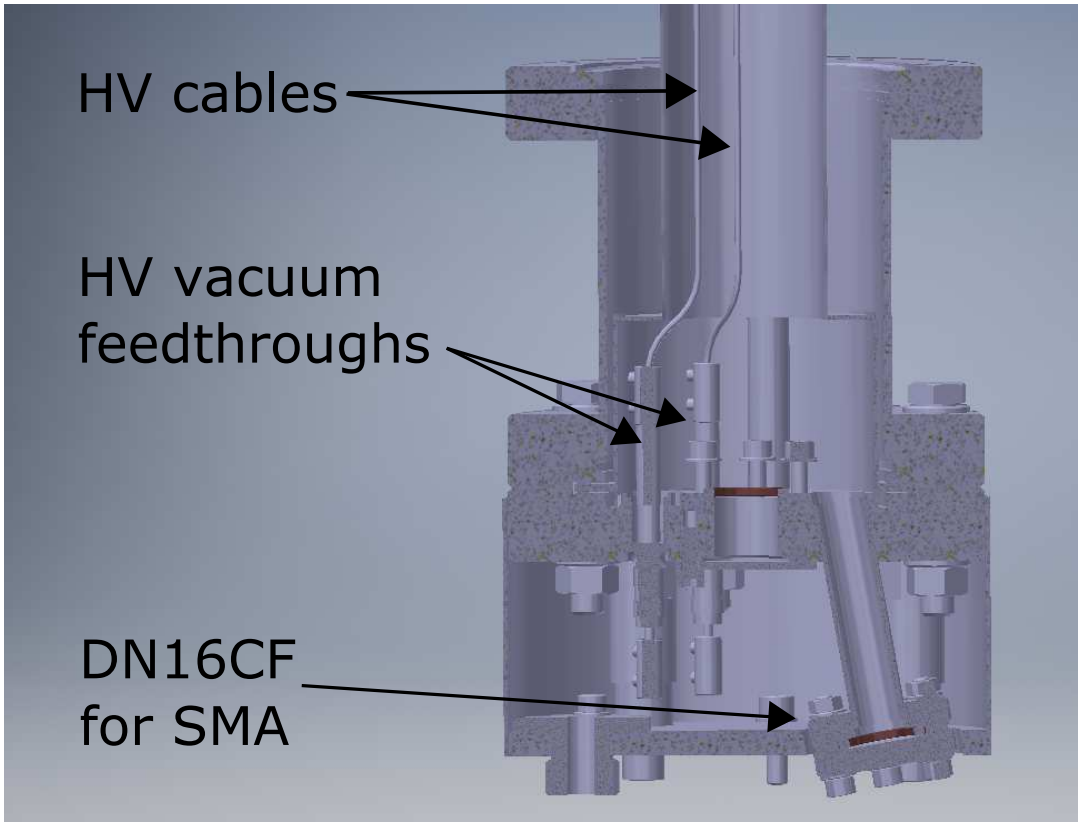

FIGURE 4.20: Cross-section of the interface section with the SHV and SMA connectors.

spectroscopy laboratory. The incoming light is split into four separate beams for the four Filterscope channels each gauge uses. Each channel is equipped with a narrow band pass filter ($\pm$1nm) so that the photo-multiplier tubes will only detect the desired wavelengths. For H measurements an H_α filter and for He a 667.8 nm, a 706.5 nm, and a 728.1 nm filter were used. Therefore, each channel monitors one single spectral line and measures its intensity.

4.5.3 Calibration at W7-X

The calibration of the WISP gauges for OP1.2b was conducted in-situ, due to the magnetic field dependence of the measurement principle. This allowed each gauge to be individually corrected for potential misalignment along the magnetic field vector. The calibration was conducted multiple times for 100 % Hydrogen and 100 % Helium, once at the beginning and once at the end of the campaign. Additionally, partial pressure calibrations were conducted for 5 %, 10 %, 20 %, and 50 % Helium in Hydrogen during the first calibration. The calibration was conducted in increasing steps of constant pressure, starting at background pressure of about 1×10^{-7} mbar

up to 8×10^{-3} mbar in 21 logarithmic equidistant steps. Of these 22 steps, not all were realized due to insufficient response of the gas valves, however 17 steps starting at 1×10^{-6} mbar could reliably be realized. Constant pressure was achieved by closing all gate valves from the plasma vessel to the vacuum pumps and injecting defined amounts of gas into the plasma vessel. Each step had a flat top duration of 10s with an additional 1 s for equilibration of gas throughout the torus system after the asymmetrical gas injection. The gas was let in through one of the valves of the main gas system, introduced in section 3.1.2. The gas flux was therefore deposited localy in one location resulting in an asymmetrical gas injection.

The receded vacuum monitoring systems, consisting of a commercial Penning/Pirani combination gauge and partially augmented with two capacitance manometers, were used as pressure reference. Especially the capacitance manometers provided a high-reliable, gas species independent, total pressure reference. These were mounted throughout the machine and were averaged to create the stair curve seen in figure 4.16 that was used as a calibration reference. The resulting ion current as a function of neutral pressure for the range between 1×10^{-4} mbar and 1×10^{-2} mbar is shown in figure 4.21. The calibration was conducted for pure H and He at multiple times during the campaign, as well as gas mixtures of 50 %, 25 %, 10 %, as well as 5 % He in H. In addition to the ion current measurements, the light intensities of the H_α and three He-I line emissions were measured and calibrated to the partial pressures of the two species. No deviation from the power law scaling 4.1 at low pressures could be observed at W7-X.

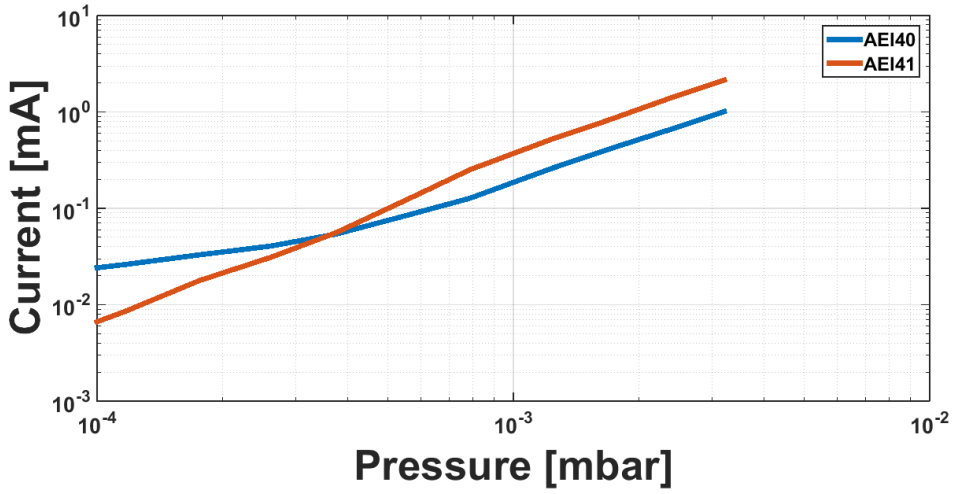

FIGURE 4.21: Ion current as a function of pressure of two WISP gauges in W7-X during calibration Program ID. 20180816.006.

4.5.4 Comparison with ASDEX pressure gauges

At W7-X, the WISP gauge was operated in the 2.5 T field at 2 kV anode potential and provided reliable pressure measurements between 1×10^{-1} mbar and 1×10^{-4} mbar at a time resolution of up to 1 kHz at higher pressures. All gauges worked reliably throughout OP1.2b without failures. The ASDEX-type pressure gauges (APG) at W7-X [101] can measure at a lower pressure, starting at 5×10^{-7} mbar up to 4×10^{-2} mbar at a time resolution of up to 5 kHz. Both gauges have an accuracy of about 15 %. The APG's are suitable for a lower pressure range and can provide a faster time resolution, while the WISP gauges are superior in the higher pressure range above 1×10^{-2} mbar.

While the APG's with tungsten filament experienced many failures in steady-state operation, the issue was resolved with the LaB_6 electron emitters in the now called crystal cathode pressure gauge (CCPG) [103]. The current in the tungsten filament necessary for sufficient electron emission reached up to 18 A. The resulting j x B forces in combination with the magnetic field of W7-X led to bends and shortages in the probe head that resulted in multiple losses of these gauges throughout the campaign. This could be avoided by using a LaB_6 crystal as an electron source which only needed 3 A for the same electron emission, decreasing the j x B forces significantly.

The WISP gauges have their advantages in the capability to reliably measure at high pressure values above 1×10^{-2} mbar, which occur inside the divertor. WISP manometers provide measurements at a higher pressure than CCPG, are gas species independent using the optical measurement and can resolve partial pressures, which is crucial for exhaust studies.

Pressure measurements and line integrated density of a discharge are shown in figure 4.22. In the first three seconds the plasma starts up with a density ramp up, after which the density is kept constant until the last few seconds of the discharge. The pressure measurements are from a set of two WISP gauges in module four and two CCPG's in the same ports in module five. Both diagnostics scale comparably and show similar effects. WISP in AEI41 and CCPG in AEI51, which are both mounted in the top divertor pump gap, measure a constant decay of the divertor pressure with an oscilation at second 20, while the two gauges in the lower divertor AEI40 and AEI50 show a rather constant divertor pressure. Differences in pressure can be explained through local effects in the different modules based on asymmetries or i.e. the strong peak in AEI51 at 3 s, due to localized gas injections close to the gauge. Under consideration of these effects, it is reasonable to conclude that measurements from both diagnostics are comparable.

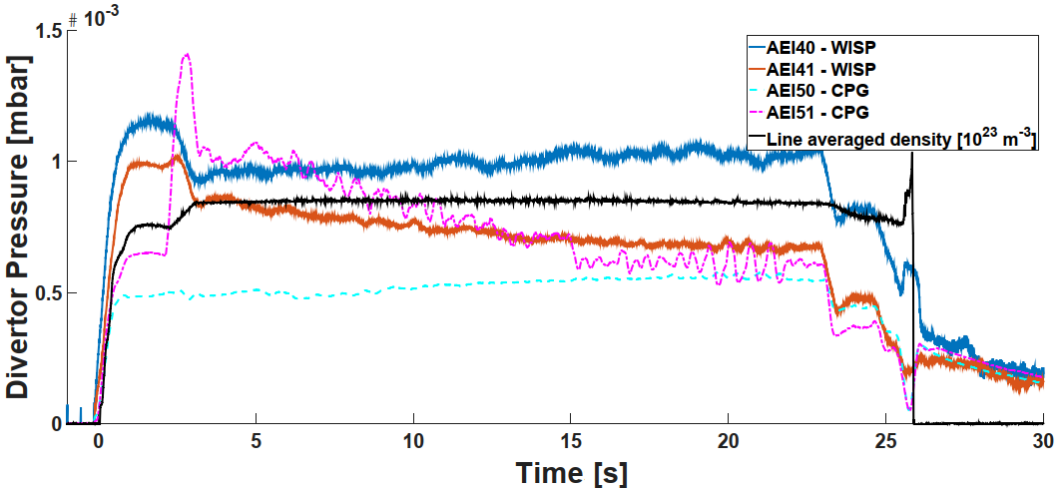

FIGURE 4.22: Comparison of divertor pump gap pressure measurements in module 4 (WISP) and module 5 (CCPG) of program ID 20181016.018 shows a general agreement between WISP and CCPG.

While the time resolution of the WISP gauges is slower than of the ASDEX-type gauges, it is fast enough to see the effect of individual pellets on the neutral pressure at 10 Hz. This effect is shown in figure 4.23 where the line averaged density is shown on the right-hand side and the H partial pressure measured by the WISP gauge in port AEI40 on the left-hand side. The density increases with the plasma start up during the first second and steep spiked density increase starting at 3 s can be seen. Each spike is an individual pellet entering the plasma and a density decay afterwards until the next pellet enters the plasma. These spikes that are formed by individual pellets can also be seen in the partial pressure measurement of the WISP gauge. While the exact time response of the WISP gauge is still under investigation, this shows that effects from pellets entering at 10 Hz can be studied. Based on the pressure measurements during the 10 Hz pellet injection, a time resolution of 10 ms is a reasonable conclusion.

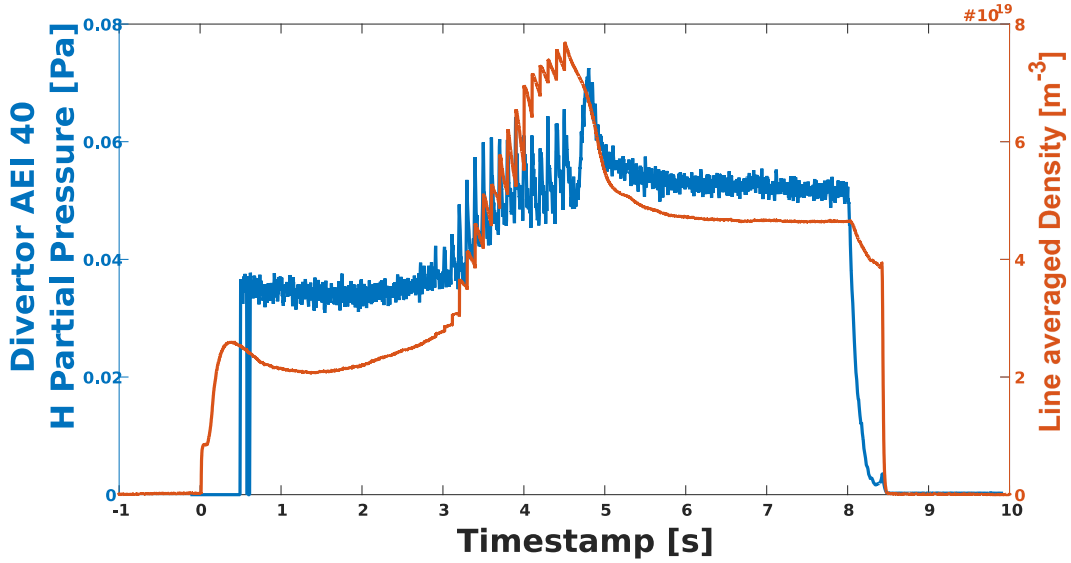

FIGURE 4.23: H_α partial pressure and line averaged density over time of program ID 20181010.025 with 10 Hz pellets.

Chapter 5

Single-Reservoir Particle Balance for Hydrogen

The results of the particle balance, introduced in section 3.2, are presented in this chapter. First the results of the different fueling efficiencies for gas injection fueling as well as the recycling particles will be discussed. With the fueling efficiencies determined, the particle balance can be solved for τ_p. The sensitivity of τ_p as the output of the particle balance to three different inputs is discussed. The particle balance is used to analyze changes in confinement time and recycling with an increase in island size. The chapter ends with a section of how the particle balance can be applied to detached scenarios. First an overview of the conducted experiments is given.

To investigate the particle balance, dedicated experiments were planned and conducted. During experimental campaign OP1.2b, experiments were conducted two or three days per week on alternate weeks. An experiment day started with the first discharge around 9 am and lasted until 5:45 pm being split into two sessions. On October 10th 2018, Session 63 was conducted in the morning session with a focus on fueling and exhaust. The experiments were designed to enable a first rigorous assessment of the particle balance. This includes fueling and exhaust terms and aims on obtaining the particle confinement time as the central integrated value. τ_p is then used to discuss the stability of the particle balance as well as relative changes in sources and sinks to it with (a) changes due to adjustment of the island divertor size and shape and (b) between attached and detached discharges. The first goal was to determine the fueling efficiencies of the two gas injection systems. The main gas system being on the inboard mid-plane side is seen as an upstream source, while the He beam with its valves in the divertor is taken as the down stream gas source.

The fueling efficiencies were measured by short gas injections of known particle numbers as described in section 3.2.2. The gas injections lead to a

sudden increase in density. The decay of the density signal was used to measure τ_p^* so that the global recycling coefficient $\bar{R}$ could be calculated together with τ_p from the particle balance. Since this was a contingency session and there was no chance to re-do discharges a later day, heating power and density were set to what proved to be stable and reliable parameters. The heating power was set to 4.5 MW with the density in the mid $10^{19} m^{-3}$ for 8 seconds.

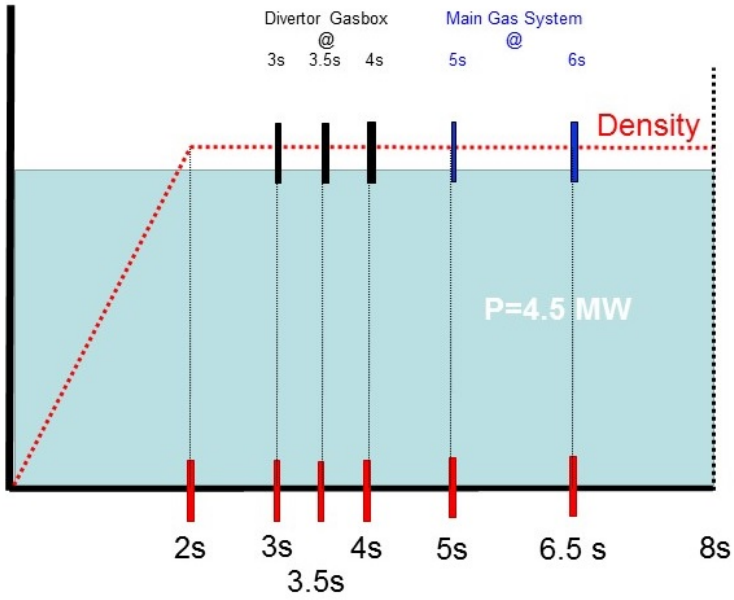

FIGURE 5.1: Discharge layout sketch as it was often used for session planing during OP1.2. Time on the x-axis while the large blue box displays the constant 4.5 MW heating power over time. The red dotted line resembles the density.

An example layout for these discharges is shown in figure 5.1. After the first two seconds of plasma ramp up, one second of flat top density is followed by three gas injections of different flux, injected by the divertor gas box, with half a second in between for τ_p^* measurements. One second after the last injection from the divertor gas box, two injections from the main gas system were executed at second 5 and second 6.5. The injected particle fluxes were changed throughout the session since the density in some of the early discharges increased beyond the ECRH cut off density. The density cut off of the X-mode ECRH heating is at $1.2 * 10^{20} m^{-3}$ and once reached, a safety interlock is triggered that terminates the discharge [104]. These experiments were conducted at the normal island size with the control coil current $I_{cc} = 0kA$ and the large island with $I_{cc} = 2kA$ to study the effects of this manipulation of the divertor geometry as discussed in 2.2.1.

Program ID	ECRH	Density [m^{-3}]	I_{cc}[kA]	Comment
20181919.008	4.5 MW	5.0×10^{19}	0	Reference discharge
20181919.010	4.5 MW	4.8×10^{19}	0	Density rise to 5.8×10^{19}
20181919.011	4.5 MW	5.8×10^{19}	2	Density rise to 1.2×10^{20}
20181919.017	4.5 MW	5.8×10^{19}	0	/
20181919.018	4.5 MW	5.6×10^{19}	2	/

TABLE 5.1: Discharge overview.

The analysis for H focuses on a set of five discharges, one reference discharge (Program ID: 20181010.008), two with normal island size (Program ID: 20181010.010 & 20181010.017), and two with a large island (Program ID: 20181010.011 & 20181010.018). Program ID 10 and 11 of that day experienced a rise in density throughout the discharge.

The interlock was triggered in program ID 11, while the density for ID 17 and 18 was consistently stable at $5.8 * 10^{19} m^{-3}$. For this reason discharge 17 and 18 will be used when directly comparing island sizes. Discharge 17 will be used in this chapter to introduce the particle balance and discuss the basic properties. To study island size effects on measurements, relative changes will be used that compare the particular measurement as:

$$\frac{Large \quad Island}{Small \quad Island} = \frac{I_{cc} = 2kA}{I_{cc} = 0kA} = \frac{20181010.018}{20181010.017} \tag{5.1}$$

An overview plot of relevant plasma parameters for discharge 17 is shown in figure 5.2. The 4.5 MW input power of the ECRH system together with the radiated power , P_{Rad}, is shown in the first panel. The input power was held constant over the discharge length with small modulations at 3 s, 5 s, and 9 s, that were included for other experiments. P_{Rad} stayed below 1 MW, and therefore never exceed 25 % of the total heating power. The line integrated electron density, as measured by the interferometer is pictured in blue in the second panel. The density ramp up from 1 s to 2 s is clearly visible with small local maxima resulting from the gas injections. Electron temperatures, T_e, measured by Thomson scattering as a function over time is shown in the third panel. The gas injections, cause only minimal signatures in the diamagnetic energy in panel four. Finally the torroidal current is shown to increase up to 4 kA throughout the discharge, in the last panel.

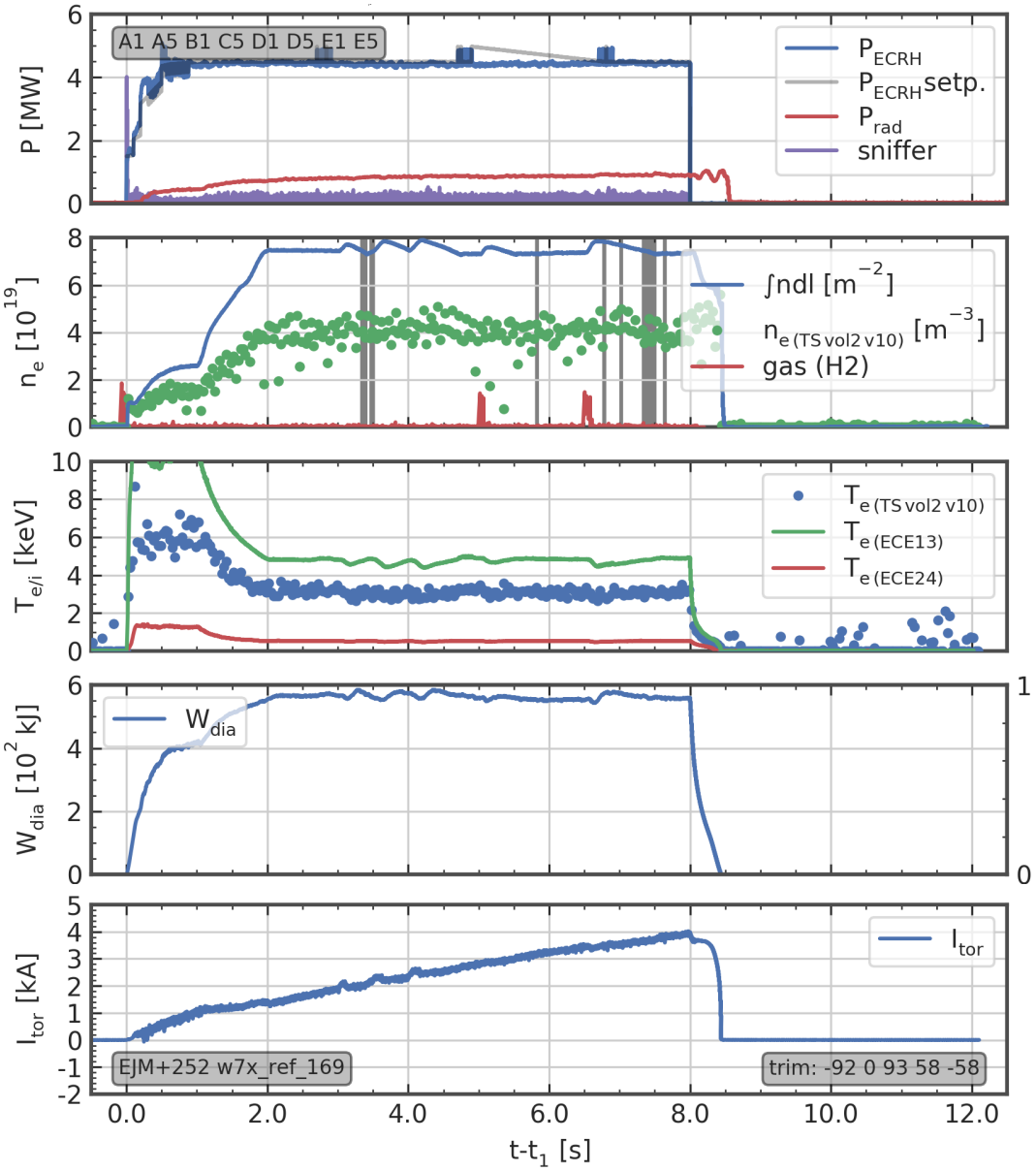

FIGURE 5.2: Overview plot for Program ID 20181010.017.

5.1 Gas injection fueling is unaffected by island size and fueling location

The fueling efficiencies for the two different gas fueling systems were measured experimentally by monitoring the density change during short gas injections which were conducted with He and H. In total 30 gas injections were conducted and the different scenarios were averaged to resolve the fueling efficiencies needed for the particle balance. The averaged values with the

standard deviation as a measurement uncertainty estimation are listed in table 5.2. No effect of the island size on the fueling efficiency could be measured so the average was taken over both island sizes. As seen in table 5.2, the fueling efficiencies for Hydrogen have no significant difference between the two systems.

	Main System	**Divertor System**
Hydrogen	0.30 ± 0.09	0.36 ± 0.12

TABLE 5.2: Measured fueling efficiencies for the main and divertor gas fueling system for Hydrogen.

5.2 Fueling efficiency of recycled H particles

Compared to gas injection fueling efficiencies, the recycling fueling efficiency is less trivial to be determined experimentally. The recycling source can not be controlled in a way to cause a sudden change in density where a density change could be measured and associated to a well quantified change in the recycling source or the total wall source. To still resolve f_{recy} experimentally a closer look at the start up of the plasma is needed. The technique that was applied to all discharges will be showcased based on figure 5.3.

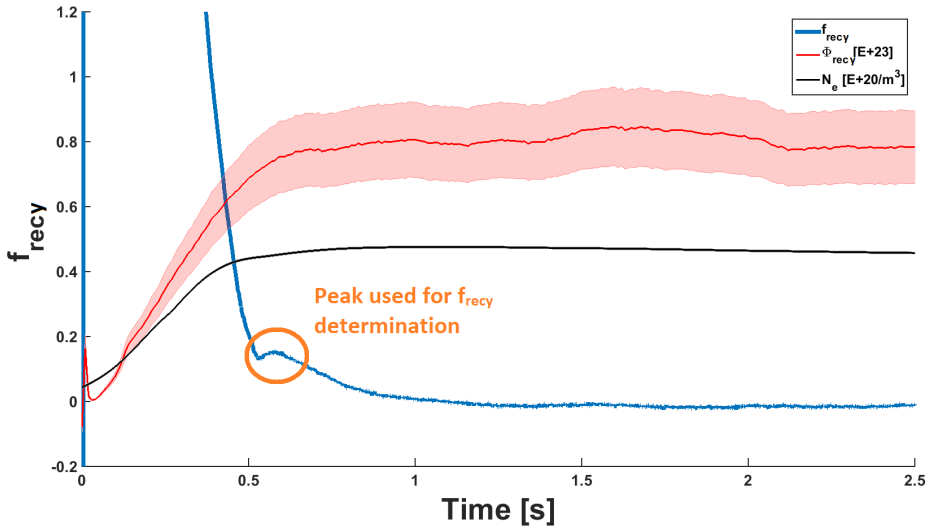

FIGURE 5.3: Density (black), Recycling flux (red), and the continous recycling fueling efficiency (blue) during plasma start up for discharge 20181010.010. The local maximum used for the determination of the value for f_{recy} is marked with an orange circle.

Here the plasma density N_e, the recycling flux Φ_{recy}, and the recycling fueling efficiency based as described in section 3.2.2, f_{recy} are plotted over time for the first seconds of program ID 20181010.010. During plasma start up, gas is injected into the torus before the start of the ECRH heating. Once the ECRH is turned on at t = 0 s, the plasma density increases within the first 0.5 s, due to more and more particles ionizing. During this start up phase, there is no additional gas fueling and the plasma is solely fueled by the recycling particles of the initial gas injection. The wall outgasing was below 1 % of the recycling flux. Eventually an equilibrium is reached and a stable flat top plasma density is reached (> 1 s).

At first, the calculated f_{recy} is highly overestimated since the main reason for the rise in density is the ongoing ionization of the initial gas injection. f_{recy} goes towards zero after the first second of the discharge, because there is no change in density anymore. However a recycling fueling efficiency can be measured during the transitioning into the flat top density around 0.6 s. At the inflection point of the density at about 0.5 s almost all particles are ionized and the density transitions from the build up into the equilibrium phase. The recycling flux follows this behavior with some delay, seen by a later inflection point at around 0.7 s. In between these two points it can be assumed that all particles are ionized and the plasma is only fueled by the recycling. Since the recycling flux and density are still increasing, values for f_{recy} can be measured. This can be seen in the time trace of f_{recy}, which reaches a local minimum at the time of the density inflection until it rises again to a local maximum, marked by an orange circle, before density and recycling flux reach their equilibrium.

The value of f_{recy} at the local maximum is thus assumed as the actual recycling fueling efficiency. For the particle balance an average of this value for the considered discharges is used, with the standard deviation as the uncertainty.

$$f_{recy} = 0.16 \pm 0.02 \tag{5.2}$$

Previous work during the OP1.1 limiter campaign based on EMC3-EIRENE modeling to resolve f_{recy}, and support this experimentally measured value [105].

5.3 Particle confinement based on the single-reservoir particle balance

With all fueling efficiencies determined, the particle balance can be solved for τ_p. In the case of H, one electron is injected with every neutral particle.

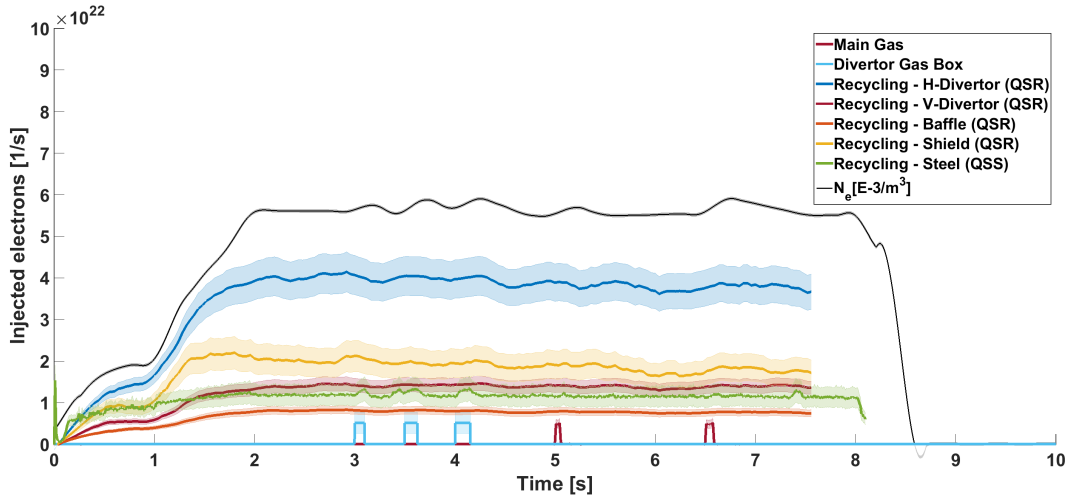

FIGURE 5.4: Time trace of all the source terms for the particle balance as well as line integrated density (Program ID: 20181010.017).

Assuming pure H plasmas, the number of electrons is equal to the number of particles. Since the interferometer is used to determine the electron density and all particle sources are converted into the electrons being released rather than particles, all particle sources can be compared based on the number of electrons a given source is injecting into the plasma. The time traces of the different sources are plotted in figure 5.4. These source terms show the number of injected electrons over time which correspond to the particles that are emitted from the sources and not the particles that actually reach the confined region. To resolve the particles that maintain density in the confined region these values are multiplied with the corresponding fueling efficiency in the particle balance.

The density ramp up in the first two seconds is followed by a one second flat top period before the density response to the three gas injections from the divertor gas box at 3 s, 3.5 s, and 4 s can be seen. These are followed by two injections from the main gas system at 5 s and 6.5 s. The fluxes that cause these bumps in the density can be seen as sharp defined fluxes in light blue for the divertor and in dark red for the main gas system.

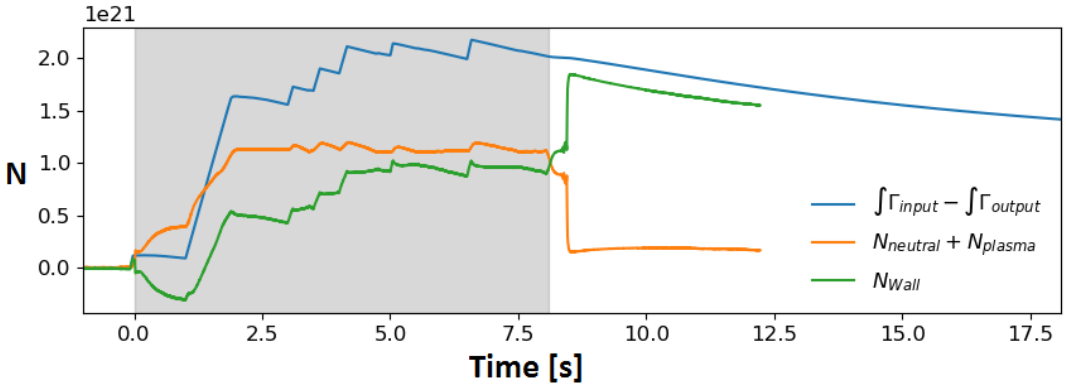

FIGURE 5.5: Preliminary gas balance for Program ID: 20181010.017. Courtesy of G. Schlisio.

The single-reservoir particle balance, as stated in section 3.2.4, can not distinguish between the recycling flux and particle desorbing from the wall. In contrast, the gas balance, that balances the neutral and plasma reservoir with the fueled and pumped neutral flux, can determine if the wall is desorbing or absorbing, and is shown in figure 5.5. The difference between the integrated input and output flux, as a function over time is shown in blue, with the combined neutral and plasma reservoir in orange. The determined wall flux is shown in green, where a negative value represents particles being released by the wall. Positive values therefore represent an absorbing wall. Throughout the discharges considered in this thesis, the wall was changing between desorbing and absorbing. However, N_{wall} determined by the gas balance stayed below 1 % of the total wall flux that was previously determined for the particle balance. This means that, as the recycling contributes 99 % of the neutral particle flux from the wall in the particle balance, the measured neutral particle source from the wall will be treated as the recycling flux in this work.

Even though the gas injection fluxes fuel about twice as well as the recycling fluxes, it is obvious that the plasma fueling was dominated by recycling particles. When considering the different recycling sources, it was measured that most of the recycling comes from the horizontal divertor target. This is expected since the horizontal target is the primary surface where the particle flux is supposed to strike the PFC. It is more surprising, that the second largest recycling contribution comes from the heat shield. Even though the flux density on the shield is a lot lower compared to the divertor, the shield has about three times the area than the target plates, leading to this large contribution.

This becomes even more evident when looking at the recycling fluxes normalized to the total recycling flux as shown in figure 5.6. Here time traces of

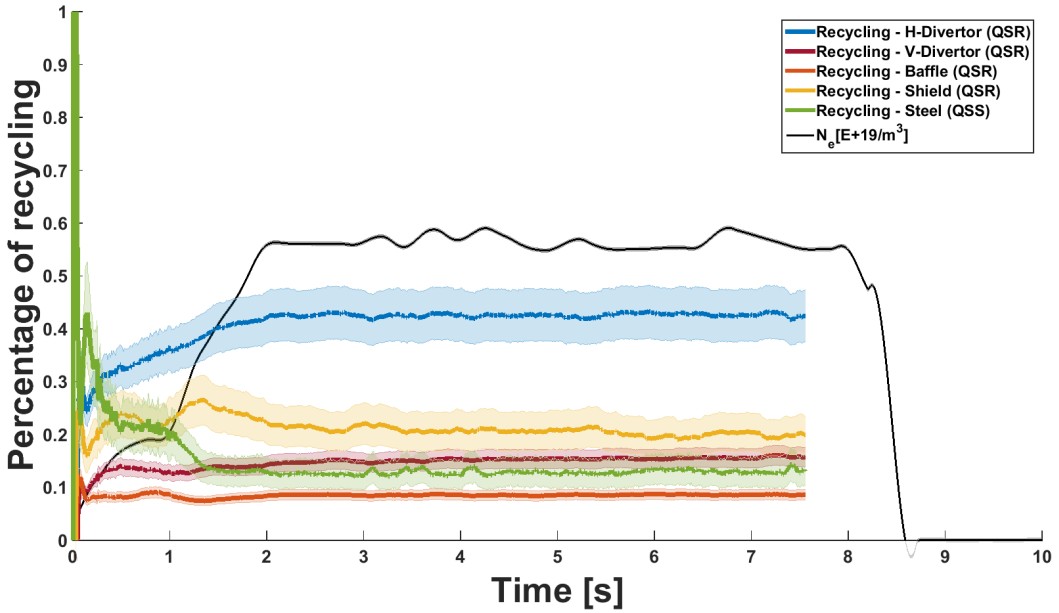

FIGURE 5.6: Recycling sources normalized to the total recycling flux (Program ID: 20181010.017).

all five normalized recycling sources can be seen, resulting in the percentile distribution of the total recycling flux. Since the recycling flux is connected to the ion flux Φ_{ion} by the global recycling coefficient $\bar{R}$ (Equation 3.3), this distribution also resembles the particle load on the different surfaces. For the first time at W7-X the particle load distribution on the different PFCs can be resolved. With the normal island size ≈ 55 % of the recycled particles come from the divertor targets, while 20 % come from the shield and 13 % from the steel panels on the low field side, with the rest of the load coming from the baffle.

With the different source and density time traces together with the measured fueling efficiencies the particle balance is fully constrained and τ_p resolved as shown in figure 5.7. After some small fluctuations during plasma start up and density ramp up, τ_p reaches a stable flat top of $0.108 \pm 0.036s$ until the gas injections start. τ_p suddenly drops during the gas injection and returns to a little higher value after the injection is completed. This does not necessarily reflect the actual particle confinement but is an artifact due to the very sharp and sudden particle increase in the balance and the delay of the density response to that injection.

A stable τ_p shows, that the sources and sinks quickly reach a stable equilibrium, once the density ramp at the beginning of the discharge is completed. This shows a finite value of τ_p, for which a particle is confined in

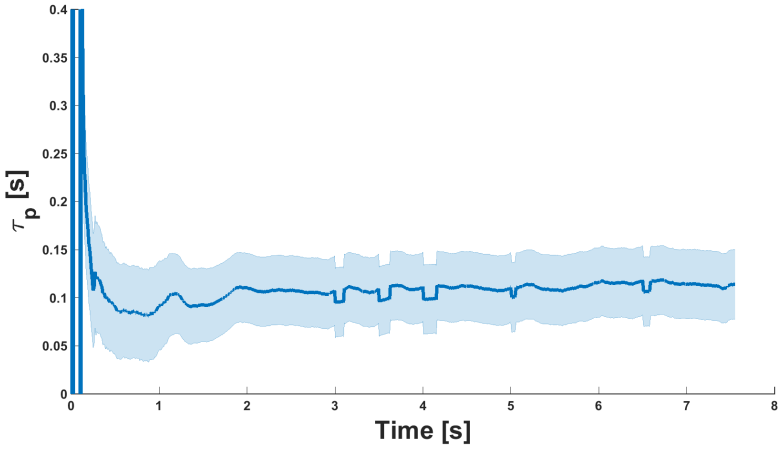

FIGURE 5.7: Particle confinement time τ_p for Program ID: 20181010.017.

the plasma. Particles that leave the confined space can refuel as recycling particles or get exhausted and removed from the system.

5.4 Sensitivity of τ_p to key input parameters: S/XB_{Wall}, f_{recy}, and camera view angle

While some measurements for this analysis are straight forward, others are prone to subject a higher level of uncertainty. To increase the understanding on how τ_p as the result of the particle balance is affected by the input parameters with the highest uncertainty, three sensitivity studies were conducted to test the robustness of the analysis.

5.4.1 Sensitivity to S/XB_{Wall}

As discussed before in section 2.5, the local plasma parameters define the photon conversion factor S/XB. In front of the divertor target the ionisation length scale is short, which results in a localized emission region, that aids to extract local plasma parameters with some reasonable uncertainty. However, because of an order of magnitude difference in density and cold plasma conditions in front of the wall, here much longer ionisation length scales are found. This results in a wide domain in which the H_α emission can be produced and hence a large variability in the plasma parameters to define S/XB. The question arises on how robust the particle balance is towards changes in the S/XB_{Wall}.

On the distance of the ionisation length scale from the wall (figure 3.13) the S/XB coefficient increases from 10 to around 30. For this reason S/XB_{Wall} was changed to 10 as an extreme minimum and 30 as an extreme maximum. The changes in τ_p compared to the value defined in chapter 3 are shown in table 5.3. A decrease in S/XB_{Wall} by 55 % leads to an increase of τ_p by 21 %,

S/XB_{Wall}	$\Delta S/XB$	$\tau_p[s]$	$\Delta\tau_p$	$\frac{\Delta\tau_p}{\Delta S/XB}$
10	- 55 %	0.131 ± 0.044	+ 21 %	- 0.38
22		0.108 ± 0.036		
30	+ 36 %	0.094 ± 0.031	- 13 %	- 0.36

TABLE 5.3: Sensitivity of the output of the particle balance, τ_p in relationship to the S/XB coefficient for the wall. Changes are in comparison to the $S/XB_{Wall} = 22$ standard case, which is used in this work.

while an increase by 36 % leads to a decrease in confinement time by 13 %. The output response is significantly smaller than the change in input. A good metric to measure the sensitivity is the error ratio, the ratio of output change over input change, as done in the last column of the table. Since both values are so close, $\frac{\Delta\tau_p}{\Delta S/XB} = -0.37$ is assumed as the error ratio for the S/XB range in this study. This means that for a 100 % change in S/XB_{Wall}, - 37 % change in τ_p is assumed or that the change in τ_p is 63 % weaker than the change in the S/XB_{Wall} input.

The uncertainty in S/XB is predominantly systematic. As long as there is no large deviation in the plasma edge parameters between compared discharges, measurements of relative changes with the particle balance are not sensitive to the uncertainty in S/XB.

5.4.2 Sensitivity to recycling fueling efficiency f_{recy}

Another difficult metric to determine is the recycling fueling efficiency since it can not be measured directly but has to be inferred from the plasma start up (section 5.2) or through simulations [105]. A broad variety of f_{recy} were tested and the response in τ_p was monitored in a similar way as done previously with the S/XB coefficients. Unlike the S/XB, the error ratios change systematically in almost an exponential decay pattern. However f_{recy} was also changed by a factor of 30 beyond realistic values and S/XB only by a factor of three. Based on previous work and modeling values between 0.1 and 0.25 for f_{recy} seem reasonable. Values below and above this range serve as an extreme test. While a strong unrealistic decrease in f_{recy} results in an

f_{recy}	Δf_{recy}	$\tau_p[s]$	$\Delta\tau_p$	$\frac{\Delta\tau_p}{\Delta f_{recy}}$
0.01	- 94 %	1.563 ± 0.521	+ 1347 %	- 14.32
0.05	- 69 %	0.325 ± 0.108	+ 201 %	- 2.91
0.1	- 38 %	0.163 ± 0.054	+ 51 %	- 1.34
0.16		0.108 ± 0.036		
0.2	+ 25 %	0.082 ± 0.027	- 24 %	- 0.96
0.25	+ 56 %	0.066 ± 0.022	- 39 %	- 0.70
0.3	+ 88 %	0.055 ± 0.018	- 49 %	- 0.55

TABLE 5.4: Sensitivity of the output of the particle balance, τ_p, in relationship to the recycling fueling efficiency. Changes are in comparison to the $f_{recy} = 0.16$ standard case as it is used in this work.

even larger percentage increase in τ_p, increasing f_{recy} results in a moderate decrease in τ_p. When decreasing f_{recy} compared to the standard case the input change is amplified for the output, but for an increase in f_{recy} the opposite is true and the output change is weaker than the input change.

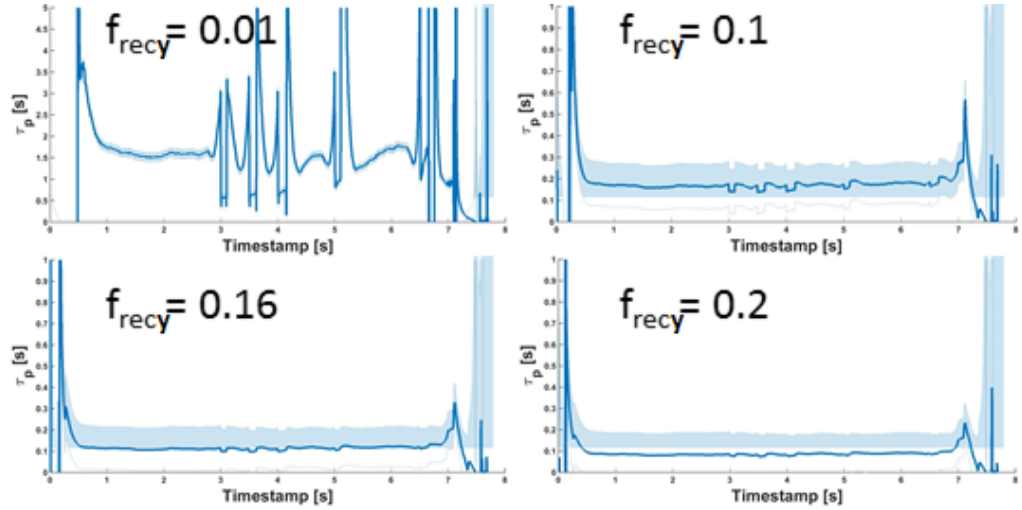

FIGURE 5.8: Effect of different f_{recy} on particle confinement time τ_p. Values for $f_{recy} = 0.01$ (top-left); = 0.1 (top-right); = 0.16 (bottom-left (standard)); = 0.2 (bottom-right)(Program ID: 20181010.017).

Another effect can be see in figure 5.8. The previously discussed artifacts from gas injections get more dominant with very low f_{recy} as seen on the top left. By decreasing f_{recy}, the overall contribution of the recycling source in the particle balance is reduced, thus increasing the effect of other particle sources. Therefore artifacts from gas injection get amplified, indicating an unrealistic value of f_{recy}. On the other hand, a higher f_{recy} flattens out the gas injection effects, because the recycling particle source contribution is increased.

As seen in table 5.4 and figure 5.8 the particle balance is very sensitive to f_{recy} and just a small decrease can change the particle confinement time tremendously. Because the recycling particle source is the dominating source term in the particle balance, it is very important to determine this value as accurate as possible. However, the fact that f_{recy} doesn't change for the experimental program considered and that it is in close agreement to simulations of the previous limiter study [105] increases the confidence in the determined value. Similar to the influence of S/XB, the sensitivity to f_{recy} causes a systematic uncertainty, which effects the absolute value of τ_p, but not the comparison of relative changes.

A comparison to more up to date EMC3-EIRENE simulations with the TDU would be beneficial to increase confidence even further. However, presently the wall is not considered as recycling surface in EMC3-EIRENE, which as we saw earlier contributes to around a third of the total recycling. These surfaces would need to be added, before the model could be used to determine f_{recy}. This is suggested as future work in chapter 7.

5.4.3 Sensitivity to the camera view angle

In an ideal scenario to calculate a photon flux into a particle flux, one would look perpendicular onto the surface with T_e and n_e being constant on the scale of the ionization length. The effect of changing T_e and n_e on the S/XB coefficient and how it is determined were discussed in section 2.5 and a sensitivity study was just presented.

The effect of camera sight lines that are not perpendicular to the surface will also be discussed in this sub-section. When looking at a larger angle through the edge layer where the ionization occurs, the line of sight length increases, and might collect more photons and therefore over estimating the actual particle flux. Another effect can be that close to the border of the defined regions of interest (ROI) in the camera field one might take photons into account that were released from a neighboring ROI. For the divertor target and baffle, the camera camera view angle is almost perpendicular to the PFC. The same is true for the filter scopes view angle on the steel panels. The heat shield, however is viewed almost entirely and the orientation of the PFC surface towards the camera change from perpendicular to very shallow angles.

To study the magnitude of this effect for H_α three different photon flux densities for the heat shield were compared for discharge 20181010.017. Two

ROIs were picked on the heat shield that have the same area of 100 x 100 pixels in the image but change drastically in the observed surface area due to the difference of the angle of incidence. While ROI1 looks almost perpendicular onto the PFC with an observed area of $0.035m^2$, ROI2 looks onto the PFC in a much shallower angle resulting in an observed area of $0.098m^2$. The position of the two ROIs relative to the strike line location can be seen in selected frames in figure 5.9.

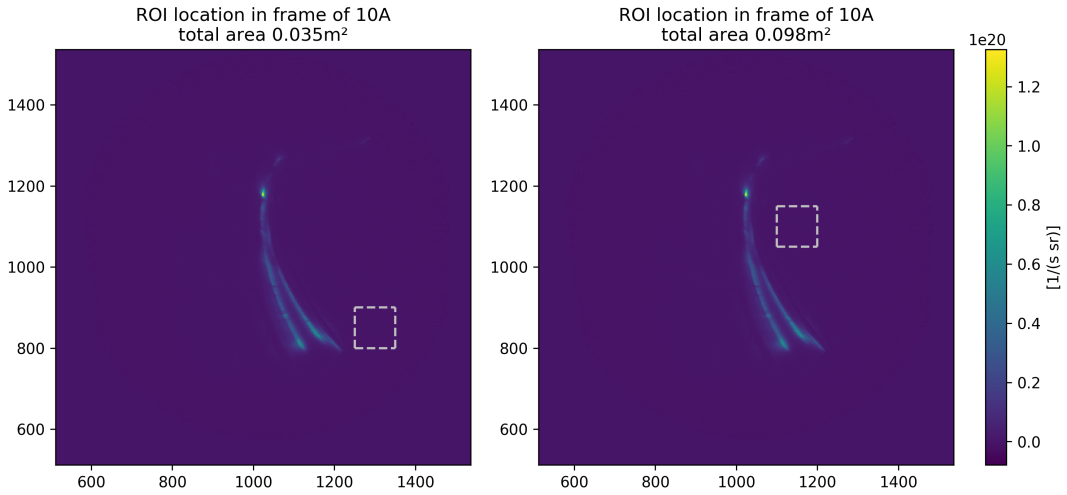

FIGURE 5.9: ROI1 on the left at pixel x = 1250 y = 800 (100x100 pixel) with an observed area of $0.035m^2$ and ROI2 on the right at pixel x = 1100 y = 1050 (100x100 pixel) with an observed area of $0.098m^2$ (P. Drewelow).

The photon flux from each ROI is then divided by the observed area to get a photon flux density. These photon flux densities are then compared to flux density from the entire shield in figure 5.10. While the three time traces rise at different speeds during plasma start up they all reach their flat top together with the density at 2 s. After 2 s a systematic difference can be seen with ROI1 having a higher flux density than ROI2 but a smaller one than the entire shield. The difference however is within the uncertainty of the integrated photon flux. Averaged from 2 s to 8 s, the flux density on the entire heat shield is 8 % higher than ROI1, while the flux density on ROI2 is 8.5 % lower. Many of the local maxima and minima are located at the same times indicating that these are indeed fluctuations in the flux density and not just random noise. Since all three ROIs differ only slightly it can be assumed that there is little sensitivity in the viewing angle and taking the entire shield as an observed area is a valid approach. This is therefore used for the determination of $\phi_{Heatshield}$.

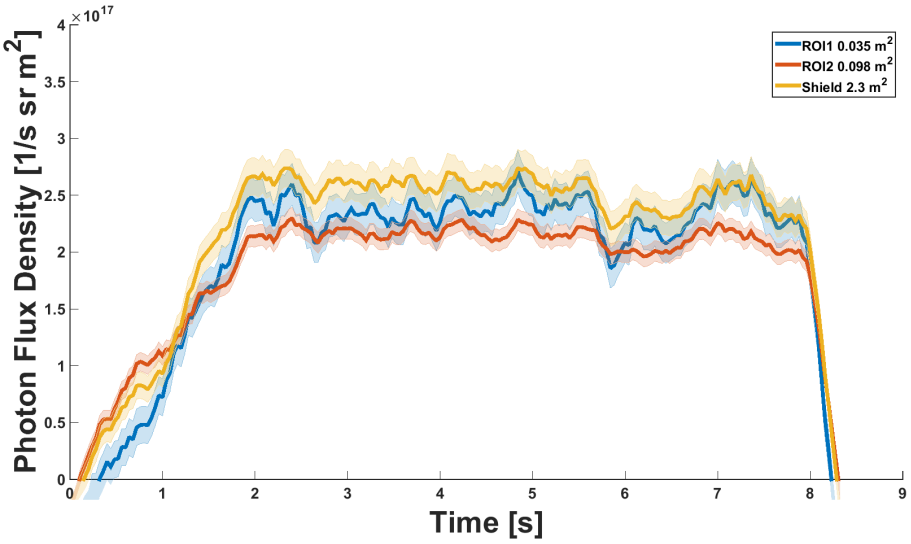

FIGURE 5.10: ROI1 on the left at pixel x = 1250 y = 800 (100x100 pixel) with an observed area of $0.035m^2$ and ROI2 on the right at pixel x = 1100 y = 1050 (100x100 pixel) with an observed area of $0.098m^2$(Program ID: 20181010.017).

5.5 τ_p, τ_e, and τ_p^* behavior with increase in island size

To study the impact of the island size as a major actuator for the divertor functionality, as discussed in section 2.2, the particle confinement time τ_p, energy confinement time τ_e, and the effective particle confinement time τ_p* have been analyzed and the results are presented in this section. The particle confinement time as the major output of the particle balance is analyzed first, followed by the energy confinement time τ_e [106]. Effective confinement time measurements are presented and are used to calculate the recycling coefficient $\bar{R}$.

In figure 5.11, τ_p is plotted over time for all four discharges that were introduced at the beginning of this chapter. The discharges with the normal island size are plotted in blue, while the large island size discharges with I_{cc} are plotted in red. The uncertainties were not plotted to keep the figure simple. Even without the ∼30 % uncertainty plotted it is obvious that all four time traces are well within the uncertainty limits and basically lay on top of each other. The increase in island size and the change in the edge topology shows no significant effect on the particle confinement time!

When considering particle confinement times, they are often compared to the energy confinement time τ_e [106] [107]. τ_e is plotted over time for the four selected discharges in figure 5.12. While the τ_e time traces for discharge

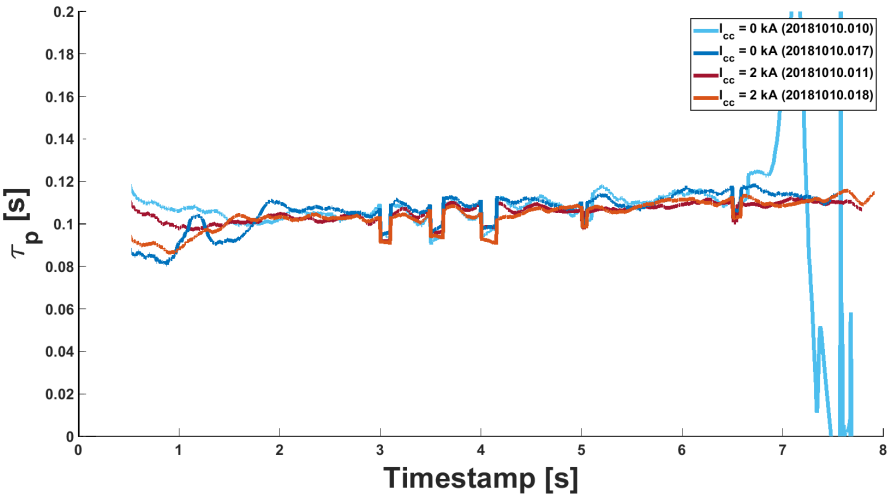

FIGURE 5.11: Plot of tau_p for all four discharges introduced at the beginning of chapter 5. Discharges with the larger island with $I_{cc} = 2kA$ are plotted in red, while the normal island size with $I_{cc} = 0kA$ are plotted in blue colors.

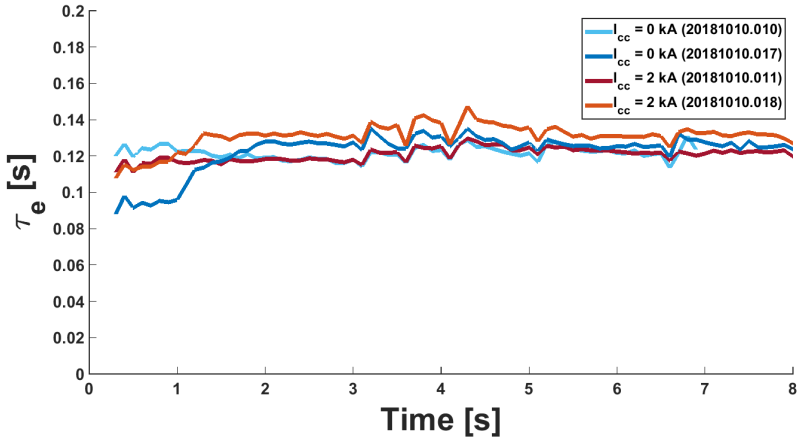

FIGURE 5.12: Plot of τ_e of all four selected discharges. Discharges with the larger island with $I_{cc} = 2kA$ are plotted in red, while the normal island size with $I_{cc} = 0kA$ are plotted in blue colors. Data courtesy of G. Fuchert

10 and 11 are practically identical from 2 s to 7 s, a slight increase is seen from discharge 17 to 18. The five gas injections can clearly be seen by a local minima of one measurement point for each gas injection in each discharge. τ_e was averaged between 2 s and 3 s, which is considered as the τ_e of each discharge since the plasma was fully developed and in a stable flat top density regime. The uncertainty for τ_e measurements is given as ± 10 % and is dominated by the power measurement of the gyrotrons.

Since there is no change in τ_e in regards to island size in discharge 10 and

Program ID	Island Size	$I_{cc}[kA]$	$\tau_e[s]$
20181010.010	Normal	0	0.1179 ± 0.0118
20181010.011	Large	2	0.1179 ± 0.0118
20181010.017	Normal	0	0.1270 ± 0.0127
20181010.018	Large	2	0.1315 ± 0.0132

TABLE 5.5: Energy confinement time τ_e averaged between 2 s and 3 s.

11 and the change between discharge 17 and 18 is well within the 10 % uncertainty it can be assumed that in this scenario the island size has no significant effect on the energy confinement time and that τ_e just like τ_p are not significantly affected by the change in island size and the resulting change in edge topology.

Since all discharges were conducted with multiple perturbative gas injections in them, the decay of the density signal after the injection can be fitted to determine τ_p^* as discussed in section 3.2.5 and are shown in figure 5.13. Here the measured τ_p^* values are plotted over time for each discharge. The

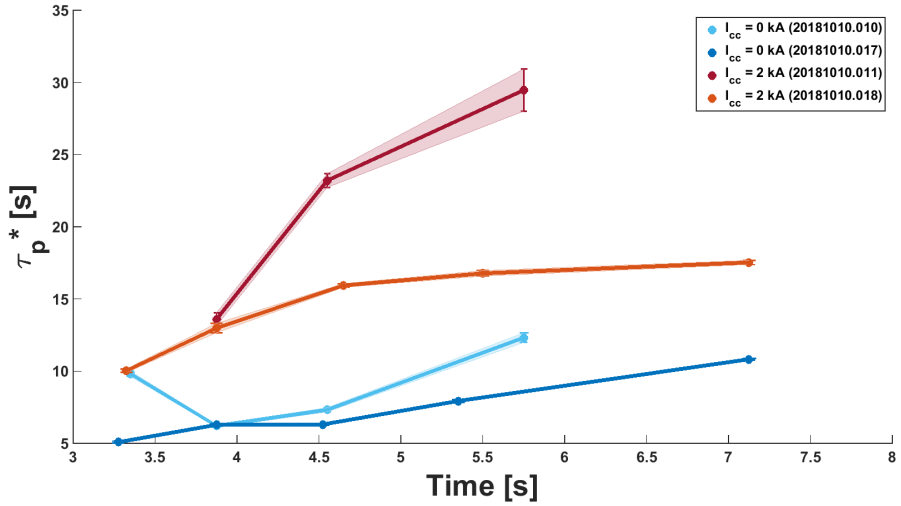

FIGURE 5.13: Plot of τ_p^* for all four discharges. Discharges with the larger island with $I_{cc} = 2kA$ are plotted in red, while the normal island size with $I_{cc} = 0kA$ are plotted in blue colors.

first three measurements are from gas injections from the divertor gas box at 3 s, 3.5 s and 4 s while the last two are from the main gas system. The points are marked at the time of the best fit of the decay signal and therefore vary slightly between discharges. The systematic increase in τ_p^* with the larger island size in red can clearly be seen.

A density rise was seen throughout the discharge for program ID 10 and 11. A density dependence of τ_p^* can therefore not be ruled out for those two

discharges. When directly comparing the large island with the normal island size we will look at discharge 17 and 18. The systematic increase of the effective confinement time is also clearly visible in this case, even if not as extreme as with the other two discharges. When comparing at these two discharges it appears that τ_p^* increases in the beginning of the discharge but flattens out with the later injections. For a comparison the last three measurements were averaged and compared. While the average τ_p^* for the normal case is at 8.1 s with $\sigma = 0.13$, it increased by 127 % to 18.37 $\sigma = 0.49$ for the large island case.

This means that with a larger island, particles spend the same time confined in the plasma, as shown with the τ_p measurement, but their effective dwell time in the system doubles, as seen in the τ_p^* measurements.

Together with the τ_p measurements, the global recycling coefficient $\bar{R}$ can be calculated for every τ_p^* measurement.

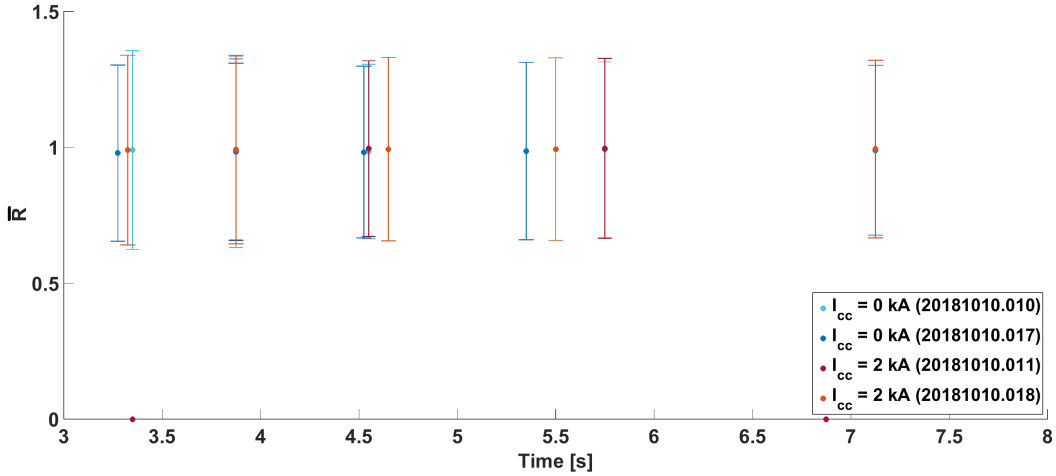

FIGURE 5.14: Plot of global recycling coefficient $\bar{R}$ for all four discharges. The data points for the discharges with the larger island with $I_{cc} = 2kA$ are plotted in red, while the normal island size with $I_{cc} = 0kA$ are plotted in blue colors.

A comparison of the different $\bar{R}$ over time with the same color code as in the previous plots is shown in figure 5.14. The first observation is that very large uncertainties of around 20 % are seen, which is simply a consequence of uncertainty propagation. To better compare the two island sizes and look for systematic changes, $\bar{R}$ was averaged over each discharge as shown in table 5.6. Even though τ_p^* is over a factor of two larger for the larger island, $\bar{R}$ varies only slightly, a systematic increase of about 1 % can be seen. This might seem counter intuitive but is compatible with equation 3.3. The explanation is that the ratio of τ_p over τ_p^* is very small. Therefore subtracting a very small ratio,

Program ID	Island Size	$I_{cc}[kA]$	$\bar{R}$
20181010.010	Normal	0	0.979 ± 0.215
20181010.011	Large	2	0.991 ± 0.209
20181010.017	Normal	0	0.975 ± 0.202
20181010.018	Large	2	0.988 ± 0.213

TABLE 5.6: Global recycling coefficient $\bar{R}$ averaged over each discharge.

or half that ratio from one will in either way result in something very close to one. A global recycling coefficient $\bar{R}$ close to unity corresponds to 100 % recycling. This indicates that the wall reservoir was in the transition between small absorption or small desorption, depending on the density level of the previous discharge and the duration of the current discharge, which is also supported by analysis of the gas balance. The gas balance showed a change in wall absorption or desorption depending on the discharge at a level of 1 % of the total recycling flux.

The finite τ_p measurement shows a stable equilibrium between particles leaving the confined area and the refueling particle flux. Since the particles spend much longer times in the system than in the confined plasma, seen in the τ_p^* measurements, the particles can recycle back into the plasma many times before being removed from the system. The recycling flux is therefore the dominating particle source and only the small amount of particles that is being removed from the system has to be compensated with external fueling.

5.6 Increased island size leads to a shift of particle loads onto main wall components

To understand the significant changes in τ^* with an increase in island size at constant τ_p, a closer look was taken at the behavior of the different recycling sources. This is shown for the normal island size in figure 5.6, this time for the large island size in figure 5.15. Just like in figure 5.6 the percentage of recycling throughout the discharge is plotted. The order and general behavior is also very similar. The largest fraction of recycling comes from the horizontal divertor target, followed by the shield, with the vertical divertor and the steel panels almost on the same level. At the steel panels we can see artifacts from the three gas injections from the divertor. This is an overestimation of the gas injection effect, since one of the four filterscope channels is very close to the gas injection location. One might already notice that compared to the

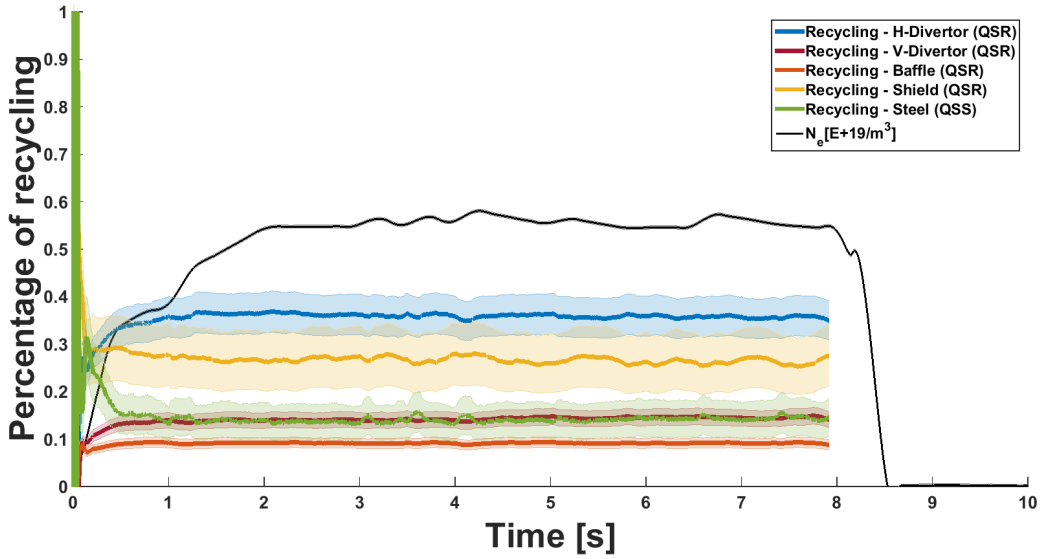

FIGURE 5.15: Recycling sources normalized to the total recycling flux with a large island with $I_{cc} = 2kA$ (Program ID: 20181010.018).

normal island size the divertor flux seems to decrease while the shield seems to increase. For a better comparison the normalized recycling fluxes were averaged for one second at flat top density between plasma start up and the first injection, from 2 s to 3 s.

ROI	**Normal Island** ($I_{cc} = 0kA$)	**Large Island** ($I_{cc} = 2kA$)	$\frac{Large-island}{Small-island}$
H-Divertor	0.42 ± 0.05	0.36 ± 0.05	0.86
V-Divertor	0.15 ± 0.02	0.14 ± 0.02	0.93
Baffle	0.09 ± 0.01	0.09 ± 0.01	1.00
Shield	0.22 ± 0.03	0.28 ± 0.04	1.27
Steel	0.12 ± 0.03	0.13 ± 0.03	1.08
N_{Recy}	$9 \times 10^{22} \pm 1 \times 10^{22}$	$9 \times 10^{22} \pm 1 \times 10^{22}$	1.00

TABLE 5.7: Normalized recycling fluxes, averaged between 2 s and 3 s, for the normal island case (Program ID: 20181010.017) and large island case (Program ID: 20181010.018) with the ratio of $\frac{Large-island}{Small-island}$ as a tool to quantify changes.

Since the given uncertainty for the normalized recycling is a systematic uncertainty that is the same for both discharges it does not need to be considered when looking at the ratios of how the recycling fluxes changed. Since the number of total recycled particles stays the same, any change in the normalized recycling represents a shift of particle loads from one area to another. Small changes are seen on the vertical divertor which looses one percent of

the total flux and the steel panels which gain one. The largest change however is seen on the horizontal target which decreases by 14 % from 0.42 to 0.36 while the flux on the shield increases by 27 % from 0.22 to 0.27. While with the normal island size the divertor receives 57 % of the total recycling flux this decreases to 50 % with the large island size. This means that 7 % of the total recycling flux is shifted from the divertor target plates onto the wall when increasing the island size to $I_{cc} = 2kA$.

With the recycling fueling efficiency at 16 %, a load shift from the divertor onto the wall should lead to an increase in neutral pressure on the mid-plane. And indeed, when comparing the mid-plane pressure, averaged over all mid-plane gauges, a systematic increase can be seen as shown in figure 5.16. For a better quantitative comparison, averaged values between 2 s and

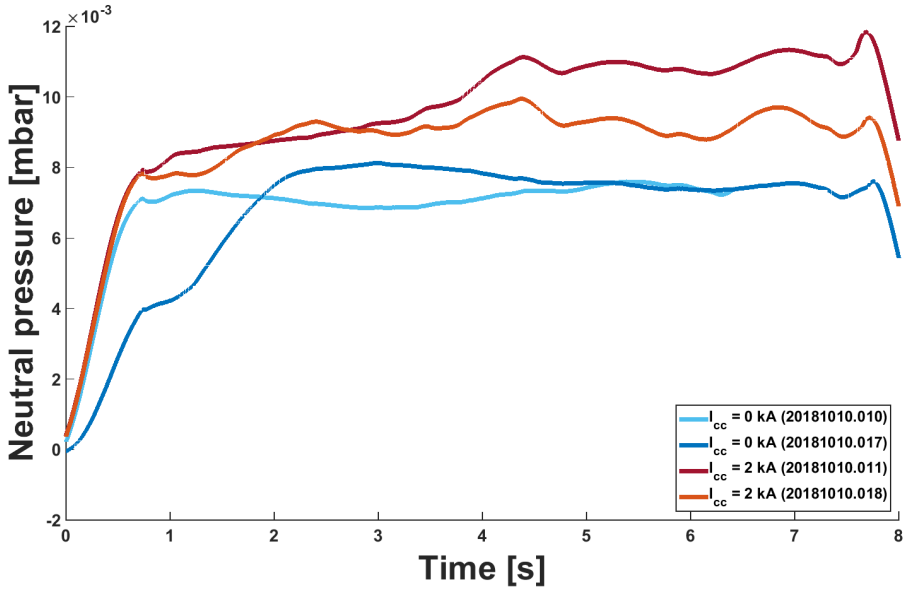

FIGURE 5.16: Comparison of midplane neutral pressure, averaged over all midplane gauges, of the four selected discharges. Discharges with the larger island with $I_{cc} = 2kA$ are plotted in red, while the normal island size with $I_{cc} = 0kA$ are plotted in blue colors.

3 s will be used, as done in table 5.8. Here and increase from 7.5×10^{-3} mbar to 9.3×10^{-3} mbar can be measured. An increase in island size which increases the load on the shield by 27 %, also leads to an increase in mid-plane neutral pressure by 24 %. This could indicate a decrease in divertor performance if the divertor pressure would stay constant, since this would result in a decreased compression ratio, which is an important metric in bench-marking divertor performance. However a similar increase by 23 % in divertor pressure from $7.0 * 10^{-2} mbar$ to $8.6 * 10^{-2} mbar$, likely due to a shift of the strike

	$p_{Midplane}$	$p_{Divertor}$	C_n
Normal Island	7.5×10^{-3} mbar	7.0×10^{-2} mbar	9.41
Large Island	9.3×10^{-3} mbar	8.6×10^{-2} mbar	9.26
$\frac{Large-island}{Small-island}$	1.23	1.24	0.98

TABLE 5.8: Neutral pressures, averaged between 2 s and 3 s, for the normal island case (Program ID: 20181010.017) and large island case (Program ID: 20181010.018) with the ratio of $\frac{Large-island}{Small-island}$ as a tool to quantify changes.

line as discussed in section 2.2 can be measured. This leads to only to a small decrease in compression ratio C_n from 9.41 for the normal case to 9.26 for the large island case. For a better overview, the neutral gas results are summarized in table 5.8. Since the divertor has a significant leak rate, it is possible that neutrals leak out of the divertor closure and also contribute to the neutral pressure on the mid-plane.

The previously discussed changes of the confinement, recycling, neutral pressure, and radiated power in regards to the control coil current are summarized in table 5.9. The values are averaged between 2 s and 3 s of stable plasma operation in the discharge.

	Normal Island	**Large Island**	$\frac{Large\ island}{Normal\ island}$
τ_p	0.104 s	0.102 s	0.96
τ_p^*	8.17 s	16.38 s	2.04
$\bar{R}$	0.986	0.993	1.01
$P_{Rad-core}$	0.29 MW	0.36 MW	1.24
$P_{Rad-SOL}$	0.50 MW	0.75 MW	1.51
p_{div}	7.0×10^{-2} mbar	8.6×10^{-2} mbar	1.23
p_{mid}	7.5×10^{-3} mbar	9.3×10^{-3} mbar	1.24
C_n	9.41	9.26	0.98
τ_e	0.127 s	0.133 s	1.05

TABLE 5.9: Parameter changes in regards to control coil currents, based on Program ID: 20181010.017 (normal island) and 20181010.018 (large island)

5.7 Increase of P_{Rad} likely due to increased sputtering on the shield

To get a better understanding of the consequences of the shift of particle flux from divertor onto the shield area, standard measurements were investigated, like measurements from the bolometer, P_{Rad} [108]. On the horizontal

bolometer array the outlying measurements are considered as the radiated power coming from the SOL while the rest is interpreted as power that is radiated from the core [108].

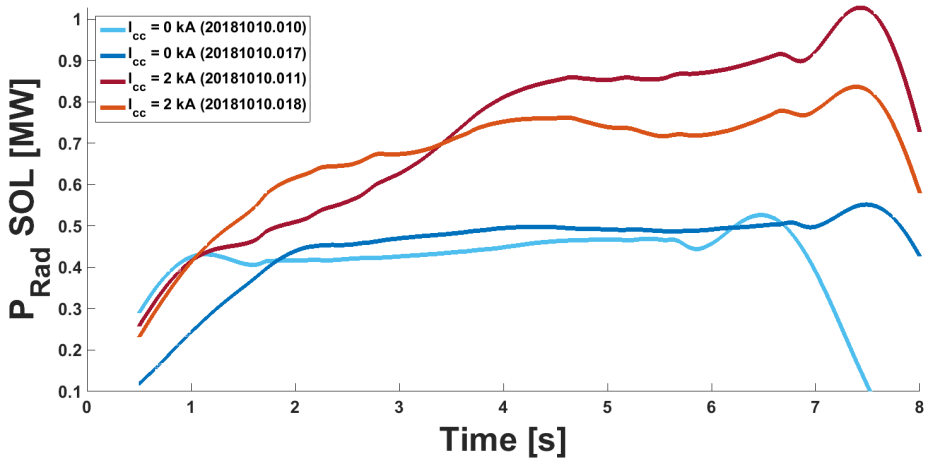

FIGURE 5.17: P_{Rad} from the SOL horizontal bolometer channels of the four selected discharges. Discharges with the larger island with $I_{cc} = 2kA$ are plotted in red, while the normal island size with $I_{cc} = 0kA$ are plotted in blue colors.

A plot of P_{Rad} from the SOL for the discharges of this study is shown in figure 5.17. Here $P_{Rad-SOL}$ is shown to increase during plasma start up until a stable value is reached for most cases after 2 s. $P_{Rad-SOL}$ seems to increase until 4 s for discharge 11, however this discharge went through a significant rise in n_e. Assuming a constant impurity concentration, P_{Rad} scales linearly with density n_e and an increase of P_{Rad} is thus expected. At the end of a discharge the maximum of $P_{Rad-SOL}$ is reached, which is due to the rise in recombination at the end of the discharges.

The two cases for the normal island size, shown in blue, are very similar during the stable part of the discharge from 2 s to 6 s where discharge 10 was terminated early. In general a strong systematic increase of P_{Rad} with increase in island size can be seen. A similar effect can also be seen for $P_{Rad-Core}$, however less extreme as shown in table 5.10.

While $P_{Rad-Core}$ increases significantly by 23 % with island size, the effect is seen even stronger in the SOL where $P_{Rad-SOL}$ increases by 51 %. Such an increase in radiated power is likely due to the introduction of a strongly radiating impurity. It is hypothesized that the measured increase of the particle loading of the shield yields an increase in the carbon sputtering source from this area that provides higher access probability of the impurities of the SOL and spearatrix region. Hence the shift of the particle flux induces an

	$P_{Rad-SOL}$	$P_{Rad-Core}$
Normal Island	0.50 MW	0.29 MW
Large Island	0.75 MW	0.36 MW
$\frac{Large\ island}{Small\ island}$	1.51	1.24

TABLE 5.10: Averaged radiated power, averaged between 2 s and 3 s, for the normal island case (Program ID: 20181010.017) and large island case (Program ID: 20181010.018) with the ratio of $\frac{Large-island}{Small-island}$ as a tool to quantify changes.

increase of the available impurities which is detected also in increasing radiative power losses from the SOL domain. Z_{eff} is a volume averaged effective charge, and as such is not very sensitive to changes to the plasma edge and SOL impurity content. Therefore, impurity line radiation in the UV range of the spectrum was analyzed using the High Efficiency XUV Overview Spectrometer system (HEXOS) with a line integrated measurement over a wavelength range from 2.47 - 161 nm [109] [110]. Since sputtering on the heat shield was the suspected cause for the increase in P_{Rad} all Carbon lines of different ionization levels were considered with HEXOS. The Carbon signals can be compared directly and do not have to be normalized for comparison, because the main plasma density was the same for discharge 20181010.017 and 20181010.018.

The change of the different Carbon lines throughout the discharge, measured by the HEXOS diagnostic is presented in figure 5.18. The line intensities of the large island case were divided by the small island case to make the changes in carbon radiation more visible. During the first two seconds of plasma start up a prominent increase in the C-III signal was measured. After the plasma build up at 2 s this, however, relaxes back to the same level as the signals from the higher charge states. The ratios of all these higher charge states stay constant throughout the discharge, all between 0.8 and 0.87 with the exception of small local maxima at the time of the gas injections.

The ratio of the C-II line shows a completely different behavior. At the beginning of plasma start up the signal is 8 times stronger than in the standard island size case as it reaches a local minimum in time at ≈1.5 s with 1/3 of the maximum value before. Then the discharge becomes stable at about 2 s and a constant increase can be seen going from 4 s up to 10 s. This shows not only that with a larger island size, more carbon is present in the machine, but also that the Carbon concentration increases throughout the entire discharge at the line integrated measurement location of HEXOS.

Two C-II lines at 678 nm and 711 nm and one C-III line at 704 nm are also

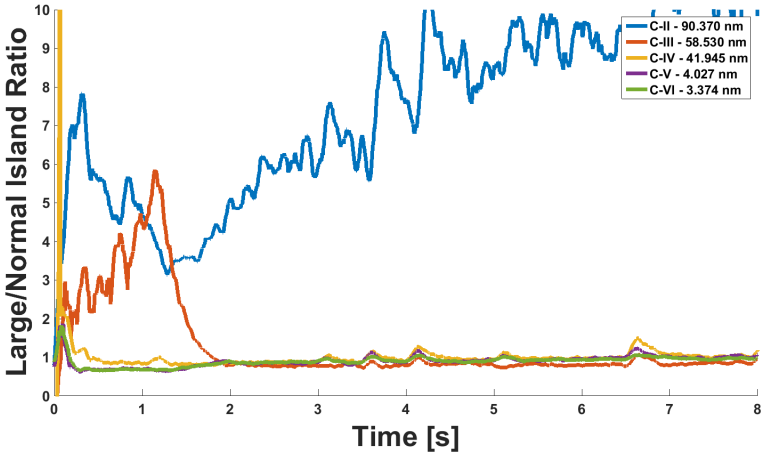

FIGURE 5.18: Ratio of HEXOS line integrated line intensities of different charge states of carbon. Ratio = $\frac{ProgramID{:}20181010.018}{ProgramID{:}20181010.017}$

observed using the high resolution spectrometer of the He beam diagnostic. These are also line integrated measurements, but unlike HEXOS, where the line of sight goes through the entire plasma, the lines of sight of the He beam are parallel to the horizontal target as shown in figure 3.1. These measurements are only in the edge outside the LCFS and intersect the island. To get the profiles from figure 5.19 the line intensities were averaged over time from 2 s to 3 s and they are plotted in dependence the distance above the target. The measured line intensity between the two discharges had to be corrected for the effect of a 22 % increase in the density in front of the target, that was also measured with the He beam diagnostic.

The lines are color coded with C-II at 678 nm in blue, C-II at 711 nm in red, and C-III at 704 nm in yellow. The normal island size is plotted as solid lines, while the large island scenario is plotted as dashed lines over the distance above the target. All lines have their maxima closest to the target and then decay as the distance increases. There is no significant change in the C-III intensity, however the C-II line intensities decrease with a larger island for the first 2.5 cm above the target. For the large island case the C-II line intensities are higher than the normal case at distances of 3 cm and above with the largest increase between 3 and 4 cm. The ratio of the line intensity for the 711 nm C-II line of the large island case over the small one is plotted in figure 5.20.

Here the increase of the carbon radiation within the 3 - 4 cm range can clearly be seen. At larger distances above 5 cm there is very little change as already shown in figure 5.19, while a decrease is seen close to the target. Comparable features are seen also for the two other carbon lines. To quantify

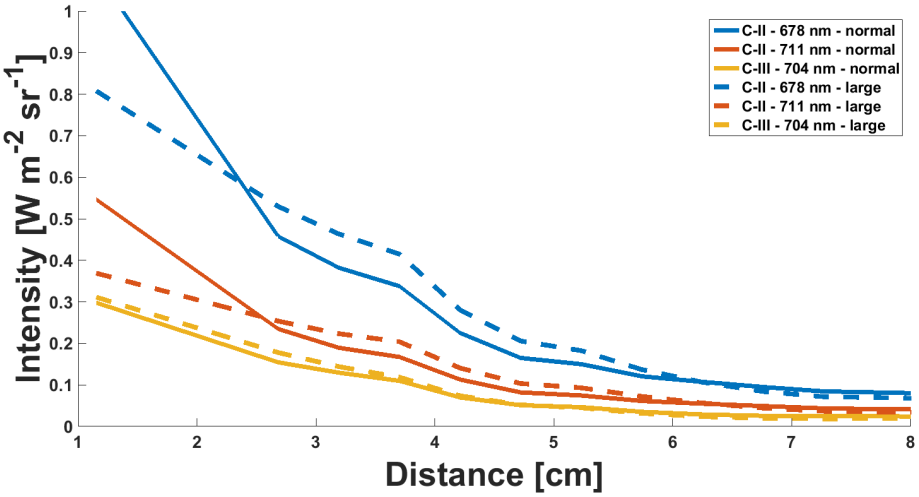

FIGURE 5.19: Carbon profiles from the He beam diagnostic over the distance above the horizontal target. Values are averaged over time from 2 s to 3 s. Solid lines are for the normal island size (Program ID: 20181010.017) while the dashed lines are from the large island size (Program ID: 20181010.018). The large island case is normalized to the change in edge density.

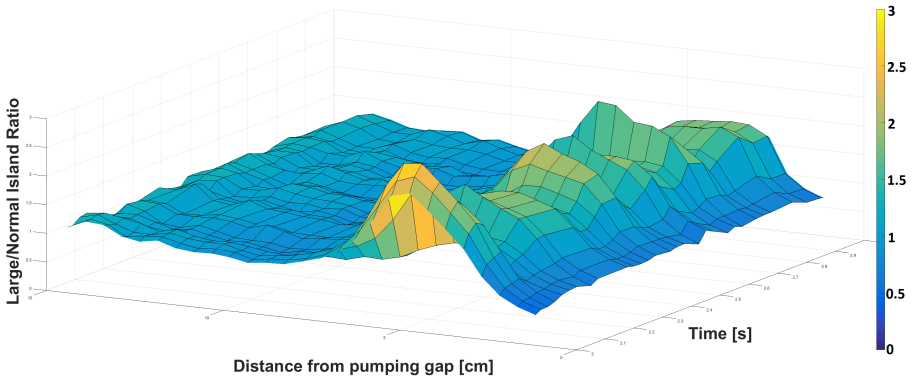

FIGURE 5.20: Change in C-II line intensity at 711 nm between 2 s and 3 s measured with the He beam diagnostic. Ratio = $\frac{ProgramID{:}20181010.018}{ProgramID{:}20181010.017}$

the change, the ratio was averaged over time from 2 s to 3 s and over distance from 3 cm to 4 cm. The C-II line intensities at this location both increase by about 44 % while no significant change is detected for the C-III line intensity, as shown in table 5.11.

The change in edge density measured by the He beam has already been mentioned briefly. A decrease by 22 % was measured resulting from the island size increase. Besides the He beam, changes in edge T_e and n_e were also monitored using the Langmuir probes. There is no significant overall change on the target, but a shift of the peak loads is measured. The maximum of T_e

Line	C-II 678 nm	C-II 711 nm	C-III 704 nm
$\frac{Large-island}{Small-island}$	1.46	1.42	1.07

TABLE 5.11: Change in carbon line intensity for the large island scenario (Program ID: 20181010.018) compared to the normal island size (Program ID: 20181010.017) measured by the He beam diagnostic. The values were averaged over time from 2 s to 3 s and over distance from 3 cm to 4 cm above the target plate.

shifts from 33 cm distance from the pumping gap further away to about 43 cm while the maximum of n_e moves closer to the pumping gap from previously 25 cm to 15 cm away from the pumping gap. This resembles the move of the strike line and island structure on the target and is visualized in figure 5.21.

Figure 3.1 is superimposed with a black guide grid. A 1 cm spacing is chosen perpendicular, and a 10 cm spacing parallel to the horizontal target. The position of the Langmuir probe array is marked with the shift of the peak loads of T_e and n_e marked by red arrows, that resemble the shift of the island with increase in size. The area above the horizontal target where an increase of carbon radiation was measured is marked with a red box.

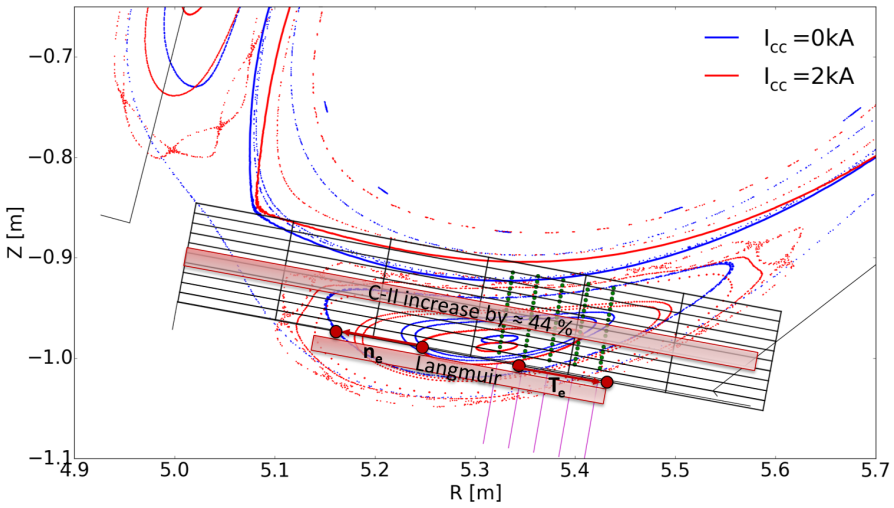

FIGURE 5.21: Location of the C-II increase and the shift of T_e and n_e on the Langmuir probe array plotted over figure 3.1.

The increase of carbon has been shown on line averaged measurements from HEXOS and more localized measurements by the He beam diagnostic and are likely the cause of the increase in P_{Rad}. To understand if the additional carbon is actually a result from sputtering we will look at the spectroscopic cameras again, just this time at the ones with a Carbon filter instead of H_α.

Unfortunately not all cameras that were equipped with Carbon filters took reliable data during these two discharges.

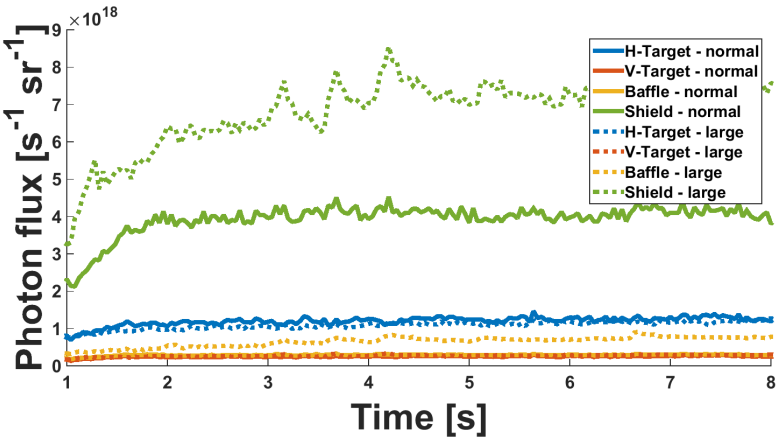

FIGURE 5.22: Photon fluxes over time of a camera in half module 11 equipped with a C-III filter. The photon fluxes are separated by the ROIs introduced in chapter 3. Solid lines represent the normal island size, dashed lines the large one.

In figure 5.22 the C-III line emission intensity obtained with a camera equipped with a narrow band pass filter at 704 nm. The ROIs are the same as defined in section 3.1 for the $H\alpha$ measurements. Solid lines represent the normal island size while dashed ones represent the large one. While the carbon photon flux from the horizontal and the vertical target do not change significantly with island size a strong effect can be seen on the shield. A strong increase of about 60 % on average can be seen throughout the discharge on the heat shield with three local maxima at the time of the divertor gas injections. Interestingly, the C-III photon flux on the baffle also increases, even though the particle load did not.

A C-II camera in half module 41, that only took data for parts of the discharge shows a similar increase on the heat shield. This is strong evidence for the hypothesis that the shift of particle loads onto the heat shield indeed causes an increase in sputtering on the graphite tiles and leads to an overall increase of the Carbon impurity.

5.8 The particle balance in detached scenarios

When approaching higher densities in order to optimize the fusion gain in a reactor scenario, the heat loads on PFCs become a major concern. In order to stay within the technical and material limitations of the divertor it is desirable

to reduce the heat and particle load by reducing the plasma contact with the material surface of the divertor, while maintaining sufficient neutral pressure for pumping. Such regimes exist and are known as detachment. Discharges with full divertor heat and particle flux detachment have been accomplished with the TDU in OP1.2 [39].

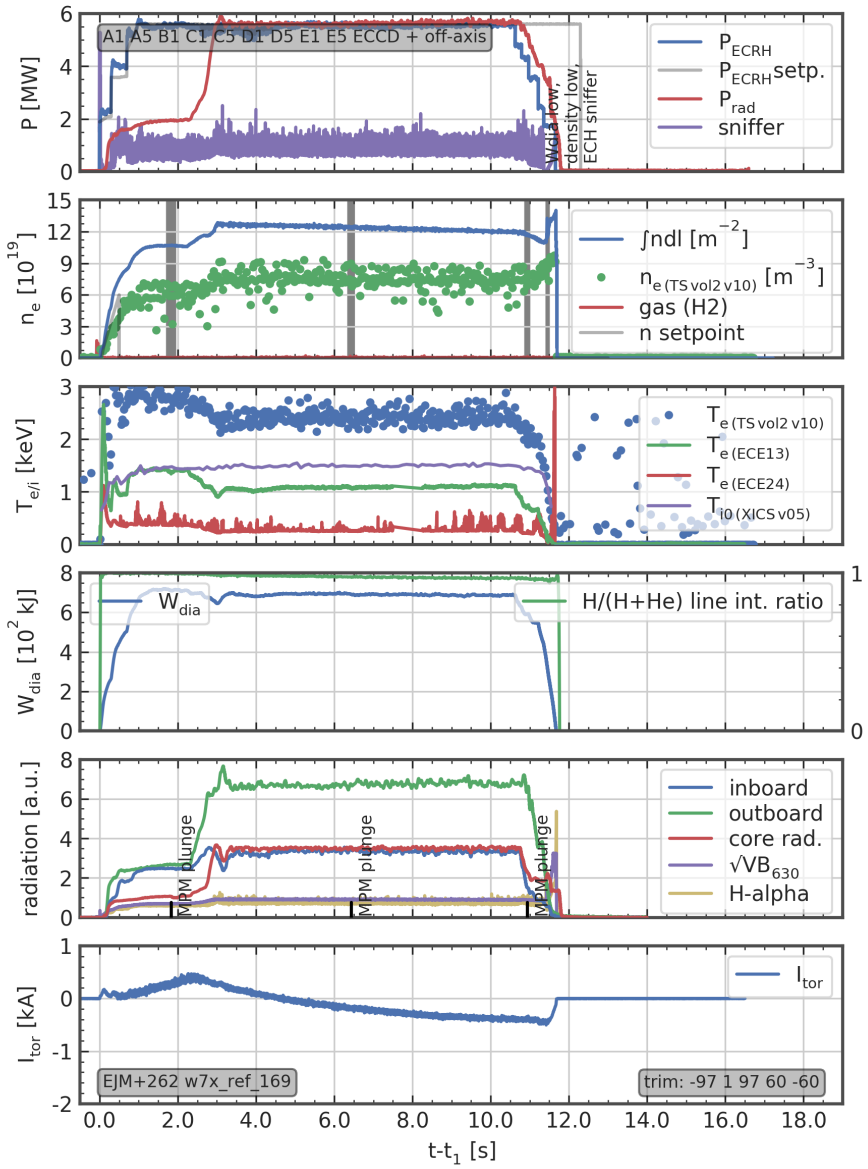

FIGURE 5.23: Overview plot for Program ID 20181010.036.

In this section the transition process from an attached phase to a detached regime in terms of the particle balance of the plasma wall and divertor system is analyzed. Changes in the recycling flux distribution on the PFCs as well as in the particle confinement time τ_p are discussed. Program ID 20181010.036 is used as an example for a detached discharge, which featured two seconds of attached operation until detachment was achieved during a density increase

between 2 s and 3 s, and was held stable for 8 seconds. An overview of important discharge parameters as a function of time are shown in figure 5.23.

This overview shall just serve as a brief summary of the parameter interdependencies to discuss the particle balance changes. An extensive discussion of the detachment process in the island divertor can be found in [39].

The rapid transition from the attached to the detached phase between 2 s and 3 s can be seen in the maximum heat flux density q_{max} from infra red measurements, averaged over all divertor targets, as shown in figure 5.24. $\bar{q_{max}}$ drops by 80 % within 0.8 s and shows that thermal detachment is achieved. The investigation of the particle detachment is part of this thesis and is presented in the following.

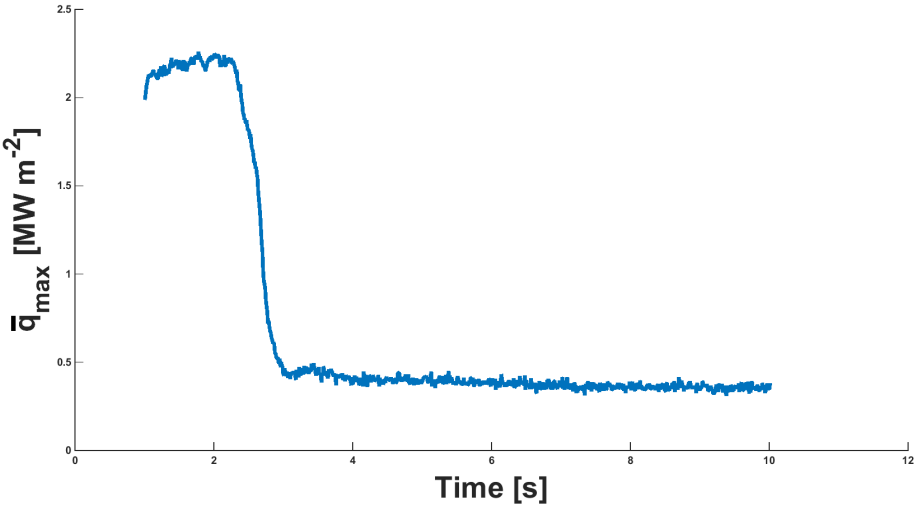

FIGURE 5.24: Maximum heat flux density averaged over all divertor targets for Program ID 20181010.036 measured by infra red cameras.

The integrated photon fluxes as well as n_e are shown in figure 5.25. The density increase between 2 s and 3 s enabled access to the detached regime, which can be seen by a strong sudden decrease in the photon flux on the horizontal and vertical divertor target. A decrease in photon flux would resemble a decrease in the recycling flux, assuming a constant S/XB coefficient throughout the discharge. If the recycling flux as the dominant particle source decreases, but the density stays at a constant high level, the particle confinement time needs to increase to compensate the decline of fueling by the recycling particles in the particle balance.

Volumetric recombination in the detached phase was investigated by all possible means by investigating molecular H bands as well as higher energy

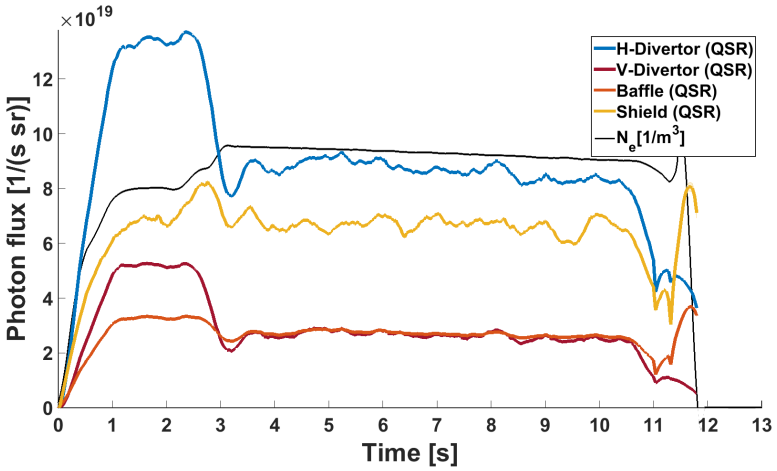

FIGURE 5.25: Photon fluxes over time for Program ID 20181010.036.

level Balmer series emissions, but no evidence could be found. It is therefore assumed that ions neutralize on the target surfaces and the analysis approach of converting photon to particle fluxes is applicable as before.

The recycling fueling efficiency f_{recy} was determined during the plasma start up, as discussed in 5.2. It is not possible to determine f_{recy} for the detached phase, since this can only be determined during the plasma start up that is attached. The fueling efficiency is dominated by the ionization length and how deeply particles can penetrate before being ionized. Based on the small change in the ionization length between the detached and attached phase, as shown in figure 3.16, f_{recy} is assumed to be constant throughout the discharge. At most it could be reduced which would reduce the impact of the recycling flux further and therefore increasing tau_p even more. The value determined during plasma start up is also used for the detached phase.

The edge density and temperature change in the divertor during the transition into detachment. This leads to a change in the S/XB factor as discussed in section 3.2.4. When applying the S/XB coefficients to the photon flux, a decrease of the total recycling flux from $1.46 \times 10^{23}\,\mathrm{s}^{-1}$ to $6.9 \times 10^{22}\,\mathrm{s}^{-1}$ can be measured.

The changes of the individual recycling sources is shown in figure 5.26. The sudden drop in recycling flux on the divertor shows that in addition to thermal detachment, particle detachment is achieved as well, as also discussed in [39]. The recycling flux on the baffle reduces slightly while the particle flux on the heat shield and steel panels stays constant within the uncertainties.

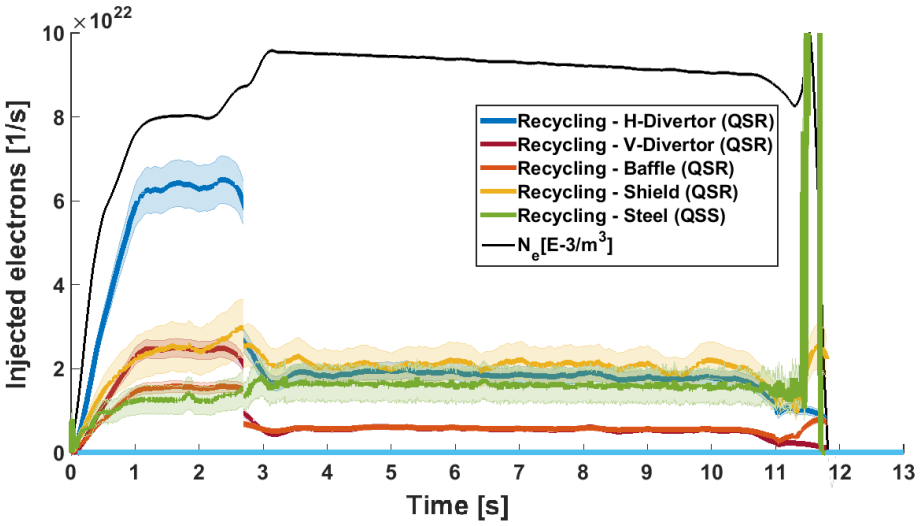

FIGURE 5.26: Source terms for the particle balance τ_p for Program ID: 20181010.036.

With all source terms determined, the particle confinement time can be resolved, as shown in figure 5.27. The particle confinement time increases from 0.101 s in the attached phase by 146 % to 0.248 s in the detached phase. This is due to two superimposing effects of an increase in N_{tot} with a decrease in Φ_{recy} as the main particle source, due to a decrease in photon flux and S/XB. The change in S/XB from 33.98 to 15.26 for the divertor and baffle was placed in the transition at 2.8 s and causes the sudden jump. This is superimposed by a decrease in photon flux as discussed in figure 5.25. The resulting change in τ_p can be seen in the increase before and after the change of S/XB. It shall be noted that the transition into detachment is tightly coupled to the fraction of radiated power f_{rad} [39][111], and that the detachment occurs rapidly in terms of the particle flux. Hence, because of the fast density ramp in this discharge, the reduction of the recycling flux and the resulting increase in τ_p are defined by the density rate of change.

In addition to the particle confinement time, the particle balance can also be utilized to determine the recycling flux distribution, as conducted for the attached scenarios. Changes with the transition into detachment can be resolved, as shown in figure 5.28. In the attached phase the divertor dominates the recycling flux with the horizontal and vertical target contributing 62 %. With the transition into detachment the recycling source is shifted from the divertor onto the heat shield and steel panels, which then contribute 55 % of the recycling flux.

The absolute values and their relative change are summarized in table 5.12. The constant high density with a reduction in the recycling flux can

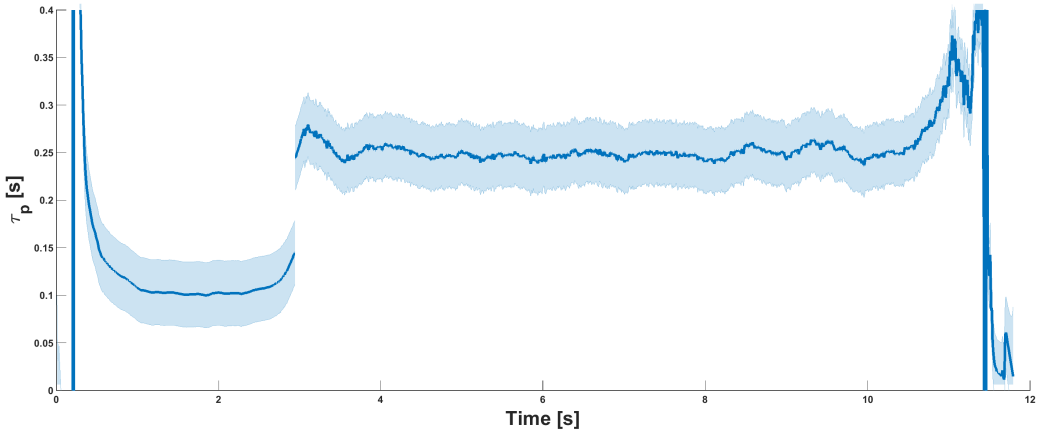

FIGURE 5.27: Particle confinement time τ_p for Program ID: 20181010.036.

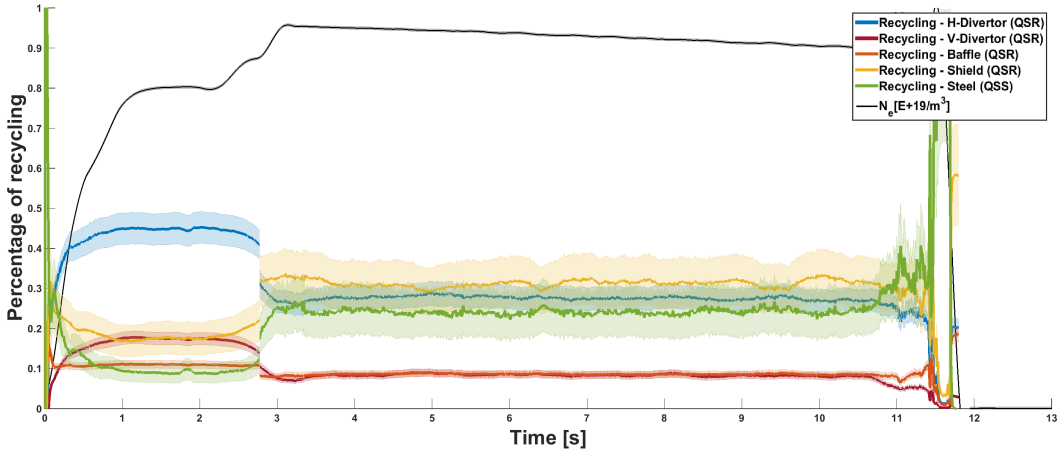

FIGURE 5.28: Recycling sources normalized to the total recycling flux (Program ID: 20181010.036).

only be supported by an increase of the particle confinement time. When transitioning into the detached phase, the flux distribution shifts from the divertor more onto the heat shield and steel panels.

	τ_p [s]	$\Phi_{recy}[s^{-1}]$	H-Div	V-Div	Baffle	Shield	Steel
Attached	0.101 $\pm$ 0.034	1.46×10^{23}	44.8 % $\pm$ 3.9	17.7 % $\pm$ 1.3	11.1 % $\pm$ 1.0	17.6 % $\pm$ 4.2	8.8 % $\pm$ 2.3
Detached	0.248 $\pm$ 0.034	0.69×10^{23}	27.8 % $\pm$ 2.8	8.6 % $\pm$ 0.9	8.6 % $\pm$ 0.9	31.1 % $\pm$ 6.3	23.9 % $\pm$ 6.1
Det/Att	+ 146 %	- 53 %	- 38 %	-51 %	- 23 %	+ 77 %	+ 172 %

TABLE 5.12: Change in τ_p, Φ_{recy}, and the recycling flux contribution of different PFCs in the attached and detached phase of Program ID: 20181010.036

The particle flux detachment is seen in a reduction of the recycling source by 53 %. This came with a shift of flux dominance from the divertor to the

main wall PFCs, contributing equally to the recycling flux in the detached phase. The increase in τ_p is in agreement with the measured recycling flux and the changes in N_{tot}. A stable τ_p through the detached phase shows a stable particle balance with these signatures which is promising for future steady state operation. A stable density in particular is necessary for steady state conditions. Improved particle confinement indicates reduced fueling needs which reduces pumping needs and aids stable density and neutral control conditions. The large decrease in τ_p could also be explained by underestimating f_{recy}. If f_{recy} would increase significantly for the detached phase, a smaller recycling flux could maintain a higher density.For the detached phase the same f_{recy} from the attached phase is assumed, as the experimental measurements discussed in section 5.2 can only be obtained in the attached start up. This assumption needs to be validated by modeling in the future. The fueling efficiency depends on the ionization length which changes only slightly, as shown in figure 3.16. These slight changes in ionization length support the assumption of marginal changes in f_{recy}.

Chapter 6

Helium Fueling and Exhaust

In addition to H injections that were discussed in chapter 5, similar experiments with short perturbative gas injections were also conducted with He to study the He exhaust and fueling characteristics at W7-X with the island divertor. The layout of the discharge was the same as shown for H in figure 5.1, where gas injections from the divertor gas box and the main gas system were injected into a H plasma with 4.5 MW heating power at a density of $5 \times 10^{19}\,\mathrm{m}^{-3}$, the only difference being that the injected gas was now He. Just like with H, these experiments were performed with two island sizes where Program ID 20181010.019 represents the normal island size with $I_{cc} = 0kA$ and 20181010.020 the large island with $I_{cc} = 2kA$.

6.1 Comparison of fueling efficiencies for helium and hydrogen

For the 10 He injections that were conducted, no significant effect of the island size on the fueling efficiency could be seen. It should be noted, that the sample size of gas injections was smaller, compared to H presented in section 5.1. This is due to the fact that there were only two discharges with He injections and that He fueled much better than expected. Because of this the injections increased the density stronger than with H and the discharge was terminated early due to the density reaching the cut-off limit [104].

The measured fueling efficiencies for He are shown next to the H results from section 5.1 in table 6.1. The standard deviation of the averaging is used as an estimate of the uncertainty. The first observations is, that the overall fueling efficiency of He was increase by 55 % compared to H, from 0.33 for H, to 0.52 for He.

The results for the different fueling systems for He are similar to H, where the measured fueling efficiency from the divertor is 5 % higher than the main

	Main System	Divertor System
Hydrogen	0.30 ± 0.09	0.36 ± 0.12
Helium	0.49 ± 0.11	0.54 ± 0.09

TABLE 6.1: Measured fueling efficiencies for the main and divertor gas fueling system for Hydrogen and Helium.

system, however they are still within the $\approx$ 10 % uncertainty. Therefore a significant difference in fueling could not be shown for either the change in island size, nor the gas fueling system. The fueling efficiencies that were measured for He however are much higher than for H. While the overall fueling efficiency for H was determined to be 0.33, He fueled 55 % better than H at 0.52. A possible explanation is that He has a longer dwell time in the system and therefore has more chances of ionization. Additionally the ionization length of He is larger than H, so that neutral He particles penetrate deeper into the plasma before ionizing, thus increasing the likelihood of He to penetrate the SOL, compared to H.

6.2 Build up of substantial helium partial neutral pressure in the island divertor

The higher fueling efficiency is not the sole reason that both He injection discharges were terminated early. A larger effect than the fueling efficiency, is due to the fact that the He that gets injected is measured to stay in the machine. This effect can be seen in figure 6.1, where the He partial pressure is shown for one divertor module in blue and the He concentration in the edge, measured by charge exchange spectroscopy [83], in yellow as a function of time. Both signals remain at the background noise level until the first He injection at 3 s and increase step wise with each injection. After each injection two different decay times can be seen. First a very fast decay results in a sudden drop in the signal over a few milliseconds until a very slow decay, sometimes even a plateau, in signal is seen. The fast decay is caused by the different speeds of the distribution of neutral He and its ionization, while the second represents the actual pumping. Once the He is injected into the plasma edge, the neutral He distributes rapidly in the vacuum vessel, which is measured in the sudden increase in He partial pressure or the He-I line in charge exchange spectroscopy. This neutral reservoir is then depleted on a slower time scale by the ionization of more and more He particles, until

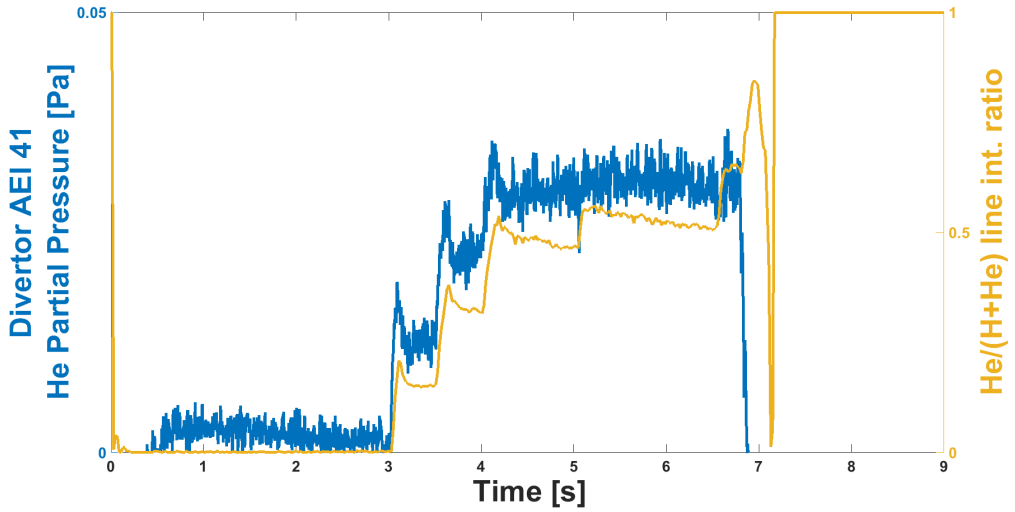

FIGURE 6.1: He partial pressure in the divertor of half module 41 (blue) and the He/(H+He) ratio out of charge exchange spectroscopy (yellow) plotted over time for program ID 20181010.020.

an equilibrium is established. This is seen in the fast decay in the first few milliseconds after the increase.

Once the equilibrium is reached, the neutral reservoir is not depleted by ionization anymore but solely by the pumping. Here only a very slow decay or even a plateau can be seen in the charge exchange data, while the He partial pressure stays constant or even increases slightly. However, the increase might just be an effect due to measurement uncertainties. Since the neutral He level practically stays constant after the equilibrium is reached, the He concentration and overall electron density increases with each additional injection.

Observation shows that the neutral He distributes quickly throughout the vacuum vessel and also gets transported into the divertor as seen in the He partial pressure. A significant build up of the He partial neutral pressure is the main requirement for a feasible He exhaust with the island divertor. While a build up of neutral pressure is shown, an exhaust due to lack of effective He pumping at sub-divertor region is not and the injected He is present throughout the course of the discharge.

Interestingly the increase of the He concentration and n_e did not result in a significant increase in overall divertor neutral pressure as shown in figure 6.2. Here the H partial pressure for the same divertor module as in figure 6.1 is plotted together with the line averaged electron density over time. The decrease in H neutral pressure can clearly be seen with each injection of He,

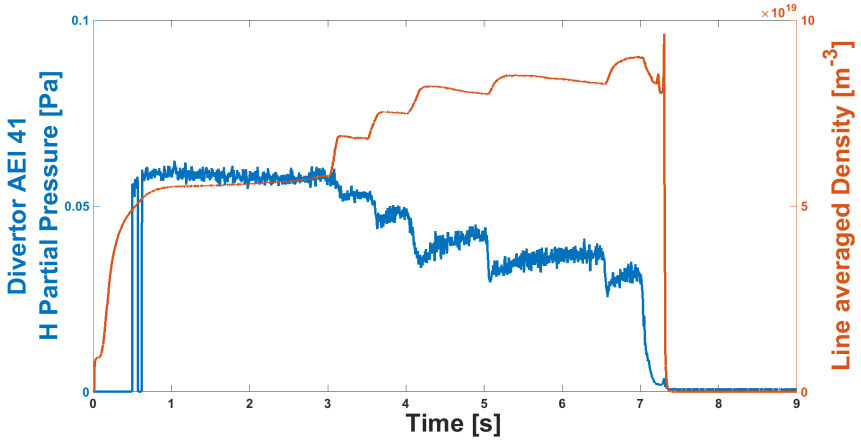

FIGURE 6.2: H partial pressure in the divertor of half module 41 (blue) and the line averaged electron density from the interferometer (red) plotted over time for program ID 20181010.020.

so much that it is almost an inverse function of the He partial pressure. After an injection a sudden drop is seen which then recovers quickly to a plateau that is at a lower value than previously. The quick recovery represents the fast He decay due to ionization until the equilibrium is reached.

This shows that the He injections do not increase the divertor pressure in total but rather that the additional He is simply changing the divertor gas composition by replacing the H, without changing the overall pressure. The line integrated electron density is plotted in red where a sudden jump is seen with each gas injection, followed by a very slow decay. The increase in density with each injection is larger than the decay in between which results in an overall increase of density until the discharge is terminated due to the ECRH sniffer interlock. For the large island case the averaged density decay time was measured at 41.0 ± 7 s compared to H with 18.4 ± 2 s. While the density decay for H represents the effective confinement time τ_p^*, this is not true for He since the n_e measurement does not differ between the contributions from He or H.

For a proper τ_p^* measurement for He one would have to use the decay of the He density or concentration. He-I lines are often used for these kind of measurements since they can be assumed to represent the He density in first order. However, when trying to fit an exponential decay to the He-I line from charge exchange spectroscopy or the He partial pressure shown in figure 6.1, the adjusted R-squared values, which define the goodness of a fit, make finding a conveying fit impossible due to the very slow or non existent decay.

The pumping speeds of the vacuum pumping system have been in-situ

calibrated with a constant gas flux of 5 mbar l/s [112]. For hydrogen at a pressure of 1.5×10^{-4} mbar at the pump, the pumping speed was determined to be at 2500 l/s while helium was pumped at 3200 l/s at a pressure of 1.5×10^{-3} mbar at the pump. With the He partial neutral pressures of 2×10^{-4} mbar in the divertor a volume flow rate of 6.4 mbarl/s, or 3.14×10^{20} particles/s, should be achieved, assuming that the pumping speed stays constant with the decrease in pressure. The largest He injections however, were on the order of this theoretical pumped flux at 2.9×10^{20} particles/s, and should have been removed from the vacuum vessel on a short time scale. This is in strong contradiction to the experiments. The pressures for the pumping speed calibration however were measured at the pump and not at the divertor. The pumps are moved far away from the divertor, as they are sensitive to strong magnetic fields. Due to the conductance losses, it is likely that the He partial pressure decreases significantly between the sub-divertor region and the pump location, resulting in a much lower pumping speed than calibrated.

The fact that He gets transported into the divertor, but practically stays there is a very strong indication that there was no effective pumping speed for He in the sub-divertor region. The reasons for this are still under investigation. One explanation could be a strong decrease in pumping speed with the decrease in pressure, as the pumping speed was calibrated with a neutral pressure an order of magnitude larger than what was measured in experiments. The vacuum pumps are also far away from the sub-divertor region, so that conductance effects could play a significant role.

No matter the cause, this is not a downside to the island divertor concept, but only a question of sufficient pumping. The substantial neutral partial pressure of He shows that the injected He is transported to the divertor, through the divertor pump gap, into the sub-divertor region. This means that, given a sufficient pumping speed for He in the sub-divertor region, He could be removed from the machine. The pumping speed for He could be improved by the addition of argon frosted cryo-pumps that are capable of pumping He [46].

Chapter 7

Conclusion and future work

The results of the thesis can be divided into two main parts. First, a dedicated diagnostic was developed for He partial neutral pressure measurements. The resultant Wisconsin In-Situ Penning (WISP) probe head was implemented and operated at W7-X and enabled the He exhaust studies presented in this thesis. The second main part consists of the development of the single-reservoir particle balance for W7-X. Fueling and exhaust of the main species hydrogen in different scenarios has been assessed by dedicated experiments that were analyzed utilizing the newly established single-reservoir particle balance, which allowed to demonstrate stable particle equilibrium in attached as well as detached plasmas. The particle confinement time as a main parameter was extracted.

7.1 Conclusion

To support the particle balance in He fueling and exhaust studies the WISP probe head was developed and optimized for partial pressure measurements in the divertor pressure regime of fusion devices. At a dedicated test facility, operation between 0.07 T and 3.5 T and with anode potentials between 1.25 kV and 5 kV have been shown. The pressure range is dependent on the anode potential and the magnetic field. The magnetic field is usually dictated by the device and can therefore be a limiting factor, especially at higher fields, since the lower end of the operating regime shrinks with an increase in field. The anode potential can be used as a tool to somewhat mitigate this effect by moving the operational range. The highest achievable pressure under these conditions was 0.1 mbar, which was limited by the maximum acceptable pressure of the vacuum pumping system at the dedicated high magnetic field test device. No reason is obvious why higher pressures could not be achieved, as long as the WISP probe head can withstand the deposited input power. A misalignment of $\pm$ 10° has no effect on the measurement.

The diagnostic was successfully implemented at W7-X and was operated reliably throughout the second part of the test divertor campaign. The gauges were in-situ calibrated and showed general agreement with other neutral gas diagnostics. The calibration followed a power law fit throughout the entire operating range without any significant deviations.

The WISP gauge enabled dedicated helium exhaust studies at W7-X. The injected helium accumulated in the divertor, measured as a significant neutral partial pressure but was not removed, indicating insufficient pumping speeds for helium in the sub-divertor space. The measurements show a significant collection efficiency of the divertor that establishes a sufficient He neutral level for pumping, which could be removed once a local He pump capability is implemented.

A single-reservoir particle balance has been established at W7-X to investigate the fueling and exhaust of the main species hydrogen. In such a particle balance the particle sources are balanced with the outward flux, which is defined by the ratio of the total number of particles and a particle confinement time. Fueling efficiencies for the gas injection sources, as well as the recycling of ions to neutrals at the plasma facing components are a key component to such a particle balance.

The analysis done to constrain the particle balance showed no significant difference between up- or down stream gas injection fueling, nor an island size effect on the fueling efficiencies. While H was fueled at 33 %, He was fueled at $\sim$ 52 % of the injected flux.

An experimental technique to determine the recycling fueling efficiency was established successfully and is in agreement with modeling for the limiter campaign at $f_{recy} = 0.16$. The single-reservoir particle balance resolved the recycling distribution on the different PFC for the first time. It was shown that in attached scenarios, the divertor contributes 57 % to the recycling flux with the heat shield at 22 %, while the remainder of the overall recycling flux source was distributed between the baffle and the steel panels.

The particle confinement time for H was measured for the first time for a 4.5 MW, $5 \cdot 10^{19} m^{-3}$ discharge at 0.108 s with τ_p^* measurements for H at 8.1 s. This resulted in a global recycling coefficient around unity within the measurement uncertainties. This indicates that the wall was saturated and potentially changes from a desorbing to an absorbing state, or vice versa. This was supported by gas balance results, and shows that the wall is a recycling source that undergoes fluctuation by wall source effects, experiencing either

an enhanced or deminished effect on the order of 1 % of the total wall source.

A study of an increase in island size and shape revealed a recycling particle load shift from the divertor onto the heat shield due to the change in edge topology. An increase in the neutral pressure in the main chamber was measured, likely due to the shift in recycling. While the particles spent the same time confined, shown with τ_p, their effective dwell time τ_p^* in the system increases by 60 % with an increase in island size from $I_{cc} = 0kA$ to $I_{cc} = 2kA$. An increase in P_{Rad} was shown, predominantly in the SOL, where it increased by 51 % with the island size. The main cause for this is an increase in the carbon impurity concentration as shown with density and temperature normalized spectroscopic measurements.

Filtered visible cameras, equipped with spectroscopic carbon filters show a significant increase of carbon emissions on the heat shield with the larger island. This supports the hypothesis that the load shift from the divertor onto the heat shield - due to the larger island - causes more sputtering on the shield, increasing the overall carbon concentration and therefore P_{Rad}.

The transition from the attached to the detached phase was investigated with the particle balance and revealed an increase in the particle confinement time τ_p by 146 % from 101 ms to 248 ms. A significant drop in the recycling flux by - 53 % was measured.

The recycling flux distribution on the plasma facing components was resolved, showing that the particle flux on the divertor decreased significantly during the transition. While the divertor contributes 63 % of the total recycling flux in the attached phase, it decreases to 39 % once detachment is reached. Particle flux detachment in addition to thermal detachment was shown.

In this discharge a constant high density was achieved, even though the recycling flux as the main fueling source decreased. The constant density required an increase in particle confinement to compensate for the decrease in fueling. The origin of this improvement in particle confinement is still under investigation, but the stable fashion demonstrates an equilibrated particle balance with stable source conditions, which is mandatory for future steady state operation.

7.2 Future work

The challenges that were revealed during this work offer new opportunities to refine and extend the analysis model. Additional fueling systems should

be included in the single-reservoir particle balance, to make it applicable to any discharge of OP1.2. The investigation of the island size and shape effects on fueling and pumping used a previous EMC3-EIRENE study as a guideline, and resemble the experimental equivalent. A direct coupled study between modeling and experimental results for a deeper understanding of the underlying effects is suggested. These immediate items for future work are described briefly in the following.

7.2.1 Additional fueling systems for the particle balance

Currently only gas injection fueling is implemented in the single-reservoir particle balance, which limits the experiments that can be analyzed. Pellet and NBI fueling will become more relevant in future operational phases but experiments with both fueling systems have already been conducted in OP1.2. Including these two fueling systems into the particle balance analysis would help to get an insight on how these fueling systems effect the particle confinement and recycling properties at W7-X.

7.2.2 Effective S/XB coefficients

In chapter 3 the S/XB values were introduced and a sensitivity study was conducted in chapter 5. Here S/XB values were calculated based on edge T_e and n_e profiles. An alternative for the target region and the $S/XB_{Divertor}$ would be the approach of effective S/XB values. In this case the photon flux from a known particle flux is measured and that ratio used as an effective S/XB value. Two versions could be feasible at W7-X. The first would be using a defined gas injection from one of the valves of the divertor gas box and measuring the emitted photon flux around the valve.

$$S/XB_{Eff1} = \frac{Defined\ divertor\ gas\ injection}{H_\alpha\ photon\ flux\ over\ piezo\ valve} \tag{7.1}$$

This method would depend on H injections existing in the discharge under investigation, which is not always the case. Another option that would not depend on gas injections would be to utilize the Langmuir probes and to measure an ion flux on the probe area. This could then again be compared to the photon flux over the probe area to get a different effective S/XB value that is independent from edge profiles or gas injections.

$$S/XB_{Eff2} = \frac{Langmuir\ Ion\ flux}{H_\alpha\ photon\ flux\ over\ probe\ area} \tag{7.2}$$

Once the ion flux data from the Langmuir probes is accessible in the necessary accuracy, this should be tested, since it has the potential to be a uniform way to resolve the $S/XB_{Divertor}$ for any attached discharge.

7.2.3 Comparison with modeling

Additionally to the effective S/XB values, the S/XB coefficients determined in this work should be compared to modeling. A plasma edge fluid and kinetic neutral model, in the form of EMC3-EIRENE, could be used for validation of the assumptions made in section 3.2.4. Instead of assuming a 1D ionization based on the plasma parameters and a dominant rate coefficient, EIRENE as a neutral gas transport Monte Carlo code could resolve all atomic processes in a 3D environment. This could be used to determine the location of where H_α radiation is emitted and S/XB coefficients for individual lines of sight. The H_α subroutine that is capable of these calculations is currently in the bench-marking process.

The recycling flux on the heat shield and steel panels is a significant factor and can contribute to over half of the total recycling flux. Presently the wall is not considered as a recycling surface in EMC3-EIRENE, and needs to be added for future comparisons. Once added, the model could be used to determine f_{recy}, as it is a key component that the particle balance is very sensitive to.

A large data base of EMC3-EIRENE simulations for attached and detached scenarios exist and should be compared from a particle balance perspective.

List of Figures

2.1 Magnetic field strength of the quasi-isodynamic configuration. Image taken from [9, Fig. 3]. 8
2.2 Path of a reflected 300 keV T ion in a poloidally closed drift orbit. The coloring of the magnetic field surface indicates the magnetic field strength, similar to figure 2.1. Image taken from [25, Fig. 11]. 9
2.3 CAD drawing of the three different coil types and their location around some nested magnetic surfaces. The modular coils are shown in grey, planar coils in brown and the saddle trim coils in yellow. The fifth trim coil as well as some planar and non-planar coils in the foreground are not pictured, so as to not obstruct the view on the magnetic field surfaces. Image taken from [26, Fig. 1]. 9
2.4 CAD drawing of coils in one module. Modular coil types 1-5 in grey and planar coils type A and B in brown are pictured as they appear in one module. The point symmetry of the half modules is clearly visible. Image taken from [28, Fig. 1(b)]. . . 10
2.5 CAD drawing of the PFCs around one divertor element. The different PFCs are color coded. The divertor target plates with the horizontal and the vertical target in light blue. These targets are surrounded by the baffle in dark blue. The largest PFCs area-wise is the heat shield in orange and the wall panels in dark red. Image taken from [29, Fig. 6(a)(modified)]. . . 12
2.6 Rotational transform ι plotted over the effective radius R_{eff} for different magnetic field configurations at W7-X. Image taken from [31, Fig. 2]. 13
2.7 Cross-section of the standard divertor configuration of W7-X at the bean shaped plane. Image taken from [32, Fig. 1]. . . . 14
2.8 CAD drawing of a divertor module overlaid with a Poincaré plot of the standard configuration in red and the wetted area in blue. Courtesy of S. Lazerson. 15

2.9 CAD drawing of the ten divertor modules in grey placed around theplasma contour in orange. Thin black lines seperate the half modules. Image taken from [31, Fig. 1]. 16
2.10 CAD drawing of a divertor module showing the different target plates, pumping gap, baffles and closures. Image taken from [34, Fig. 2]. 17
2.11 Wall to wall connection length of the island structure with $I_{cc} = 0\ kA$ in (a) and the island structure with $I_{cc} = 2\ kA$ in (b) at toroidal angle $\phi = 12.5$ with L_c towards plasma core > 1000 m. Taken from [39, Fig. 6]. 18
2.12 Neutral pressure in the divertor chamber as function of carbon radiation fraction for high-mirror configurations (a) and SDC (b). Taken from [32, Fig. 8 & 9]. 21
2.13 Poincaré plot of the normal island on the left with $I_{cc} = 0kA$ and the large island with $I_{cc} = 2kA$ on the right. The Poincaré plot with the change in the edge topology is visualized in red, while blue marks the wetted area on the horizontal and vertical target. Courtesy of S. Lazerson. 21
2.14 Electron paths between co-axial cylinders in an axial magnetic field. B is increasing from 1 to 4. Taken from [54, Fig. 1]. 26
2.15 Schematics of the quadrupole field of a Penning trap, Ring Anode (a) and Cathode (b). Based on a sketch from [56]. 28
2.16 Classical epitrochoidal trajectory in the radial plane. Taken from [58]. 29
2.17 H_α S/XB coefficients for 5 different temperatures over the electron density taken from the ADAS data base [62]. 32
2.18 H_α S/XB coefficients for 5 different densities over the electron temperature in eV taken from the ADAS data base [62]. 32

3.1 Poincaré plot for the standard configuration in the island divertor. Normal island size is shown in blue, large island size in red. Pink lines resemble the gas injection valves while the green dotted lines resemble the area of observation from spectroscopy. Red area marks the location of the Langmuir array. Courtesy of T. Barbui. 36
3.2 Cross-section through module 3, visualizing the beam path length of the IEDDI. Taken from [68]. 36
3.3 Valve box of the divertor gas injection system with the main supplies attached. Taken from [63, Fig. 1]. 38

3.4 CAD drawing of the numbered Langmuir probes in the horizontal target of the TDU. The center of the torus is to the upper right with the pump gap starting where the CAD model ends.. Taken from [77]. 40
3.5 Overview of the MPM set up on W7-X. Taken from [81]. 41
3.6 Wide angle picture of one module at W7-X. The immersion tubes with the three windows for the three cameras can be seen with a sketched field of view in orange. The cameras on the left are focused on the lower divertor region while the ones on the right observe the upper divertor. Taken from [84]. 43
3.7 (a)Field of view of the filtered visible cameras superimposed with an H_α photon flux measurement. The regions of interest are color coded for the shield (gray), baffle (orange), horizontal (green), and vertical (red) target. Courtesy of P. Drewelow. (b) CAD drawing of the PFCs around one divertor element. Image (b) taken from [29, Fig. 6(a)(modified)]. 44
3.8 C-III (465.4 nm) photon flux of port AEK41 viewing a graphite surface and AEK11 viewing an open port for Program ID: 20181010.017. 44
3.9 Electron density as a function of time for Program ID: 20181010.017. Points $n_{e,1}$ and $n_{e,2}$ for each puff used for fueling efficiency measurements are labeled. 48
3.10 Recycling process of H atomic ions striking a PFC. Taken from [14, P. 39, Fig. 1.29]. 51
3.11 Edge temperature and density profiles for the divertor and wall areas. Temperatures are given in [eV] while the density is given in $[10^{18}m^{-3}]$. The LCFS is 22.7 cm away from the wall and around 8 cm away from the divertor. 55
3.12 Local S/XB coefficients based on the local temperature and density as shown in 3.11 taken from the *Atomic Data and Analysis Structure - ADAS*. 56
3.13 Degree of ionization α plotted over the distance from the PFC in blue for the Divertor target based on He beam data and in red for the wall, based on MPM data. 58

3.14 Edge temperature and density profiles for the divertor and wall areas in a detached scenario. Temperatures are given in [eV] while the density is given in $[10^{18}m^{-3}]$ for the wall and $[10^{19}m^{-3}]$ for the divertor. The LCFS is 22.7 cm away from the wall and around 8 cm away from the divertor. Values between the Langmuir probe and the first measurements of the He beam are interpolated 59
3.15 The two different S/XB values that are used for this study in attached scenarios. $S/XB_{Divertor}$ is used for the horizontal and vertical divertor target as well as the baffle while S/XB_{Wall} is used for the steel panels and the heat shield. 60
3.16 Degree of ionization α plotted over the distance from the PFC in blue for the Divertor target based on He beam data and in red for the wall, based on MPM data. 61
3.17 OP1.1 set up 64
3.18 Schematics of OP1.1 set up 65

4.1 Anode design schematics (not to scale) and pictures taken of a He discharge of the (a) NSTX-U anode, (b) double ring anode, and (c) single ring anode. Magnetic field is horizontal for this view. Taken from [95, Fig. 2]. 68
4.2 Light intensity of the He_{667} line with constant pressure at $T_{int} = 0.1s$ with a USB CCD spectrometer, left to right at different voltages: Ring, New Double Ring, Old Double Ring, Tube Anode. 69
4.3 CAD model of WISP Probe Head showing (a) front, (b) side, (c) top, and (d) isometric view. 70
4.4 Picture of a cross section of the WISP probe head with the lens in green, pin hole section in red and the field of view lines in black. 71
4.5 Picture of a WISP probe head on top of an adjustment unit to align it to the magnetic field vector. 72
4.6 Picture of the super conducting magnets of MDPX in black. The two sets of magnets are separated by a large air gap housing the UHV chamber used for this study. 73

4.7 Picture of the UHV chamber used for this study with the immersion tube on the left, viewports in the front and on the right, as well as pressure gauges in the back. The vacuum chamber was mounted in the center of MDPX using aluminum holders. 74
4.8 Measured ion current for pressure sweeps in He at various B field strengths with anode at 1500 V. 76
4.9 B field comparison of He-I (668 nm) line intensity measurements over pressure of WISP probe head in He at 1500 V with an integration time $T_{int} = 600ms$. 76
4.10 Ion current over pressure of WISP probe head in H at 1.024 T at different potentials. 78
4.11 Comparison of H and He ion current measurements over pressure of WISP probe head at 3000 V. 79
4.12 H_α and He-I line intensities at $T_{int} = 600ms$ over pressure of WISP probe head at 2 kV, 1.024 T and 1.7×10^{-3} mbar of H. . . 81
4.13 He_{668} line intensity at $T_{int} = 600ms$ over pressure of WISP probe head at 2 kV and different partial pressures of H. 82
4.14 WISP probe head at 1.5 kV and relative misalignment of 0°, 5°,10°, and 15° to magnetic field vector. 83
4.15 Picture of a the plasma column inside the anode ring in He. The opening of the pinhole camera can be seen between the anode and the lower cathode plate. 83
4.16 Pressure calibration curve that was conducted at the end of the campaign (ID: 20181010.001). The commercial baratrons serve as a reference that the other neutral gas gauges are calibrated against. In this plot the WISP signal is calibrated to the same calibration curve that was conducted at the beginning of the campaign (ID: 20180703.507). 84
4.17 (a) Cross section of module 4 of W7-X with the three mounting positions of the WISP gauge. (b) Cross section as a sketch with the plasma facing components and the relative positions of the WISP gauge. Sketch (b) based on a graphic from reference [32, Fig. 1]. 85
4.18 Picture of a the hole diaphragm on the front plate of the probe head space 86

4.19 Picture of the inside of the immersion tube without the surrounding ECRH cover. The fins as well as the insulated copper wires can be seen from the feed-through looking towards the probe head space. 87
4.20 Cross-section of the interface section with the SHV and SMA connectors. 88
4.21 Ion current as a function of pressure of two WISP gauges in W7-X during calibration Program ID. 20180816.006. 89
4.22 Comparison of divertor pump gap pressure measurements in module 4 (WISP) and module 5 (CCPG) of program ID 20181016.018 shows a general agreement between WISP and CCPG. 91
4.23 H_α partial pressure and line averaged density over time of program ID 20181010.025 with 10 Hz pellets. 92

5.1 Discharge layout sketch as it was often used for session planing during OP1.2. Time on the x-axis while the large blue box displays the constant 4.5 MW heating power over time. The red dotted line resembles the density. 94
5.2 Overview plot for Program ID 20181010.017. 96
5.3 Density (black), Recycling flux (red), and the continous recycling fueling efficiency (blue) during plasma start up for discharge 20181010.010. The local maximum used for the determination of the value for f_{recy} is marked with an orange circle. 97
5.4 Time trace of all the source terms for the particle balance as well as line integrated density (Program ID: 20181010.017). . . 99
5.5 Preliminary gas balance for Program ID: 20181010.017. Courtesy of G. Schlisio. 100
5.6 Recycling sources normalized to the total recycling flux (Program ID: 20181010.017). 101
5.7 Particle confinement time τ_p for Program ID: 20181010.017. . . 102
5.8 Effect of different f_{recy} on particle confinement time τ_p. Values for f_{recy} = 0.01 (top-left); = 0.1 (top-right); = 0.16 (bottom-left (standard)); = 0.2 (bottom-right)(Program ID: 20181010.017). . 104
5.9 ROI1 on the left at pixel x = 1250 y = 800 (100x100 pixel) with an observed area of 0.035m^2 and ROI2 on the right at pixel x = 1100 y = 1050 (100x100 pixel) with an observed area of 0.098m^2 (P. Drewelow). 106

5.10 ROI1 on the left at pixel x = 1250 y = 800 (100x100 pixel) with an observed area of $0.035m^2$ and ROI2 on the right at pixel x = 1100 y = 1050 (100x100 pixel) with an observed area of $0.098m^2$(Program ID: 20181010.017). 107
5.11 Plot of tau_p for all four discharges introduced at the beginning of chapter 5. Discharges with the larger island with $I_{cc} = 2kA$ are plotted in red, while the normal island size with $I_{cc} = 0kA$ are plotted in blue colors. 108
5.12 Plot of τ_e of all four selected discharges. Discharges with the larger island with $I_{cc} = 2kA$ are plotted in red, while the normal island size with $I_{cc} = 0kA$ are plotted in blue colors. Data courtesy of G. Fuchert 108
5.13 Plot of τ_p^* for all four discharges. Discharges with the larger island with $I_{cc} = 2kA$ are plotted in red, while the normal island size with $I_{cc} = 0kA$ are plotted in blue colors. 109
5.14 Plot of global recycling coefficient $\bar{R}$ for all four discharges. The data points for the discharges with the larger island with $I_{cc} = 2kA$ are plotted in red, while the normal island size with $I_{cc} = 0kA$ are plotted in blue colors. 110
5.15 Recycling sources normalized to the total recycling flux with a large island with $I_{cc} = 2kA$ (Program ID: 20181010.018). 112
5.16 Comparison of midplane neutral pressure, averaged over all midplane gauges, of the four selected discharges. Discharges with the larger island with $I_{cc} = 2kA$ are plotted in red, while the normal island size with $I_{cc} = 0kA$ are plotted in blue colors. 113
5.17 P_{Rad} from the SOL horizontal bolometer channels of the four selected discharges. Discharges with the larger island with $I_{cc} = 2kA$ are plotted in red, while the normal island size with $I_{cc} = 0kA$ are plotted in blue colors. 115
5.18 Ratio of HEXOS line integrated line intensities of different charge states of carbon. Ratio = $\frac{ProgramID:20181010.018}{ProgramID:20181010.017}$ 117
5.19 Carbon profiles from the He beam diagnostic over the distance above the horizontal target. Values are averaged over time from 2 s to 3 s. Solid lines are for the normal island size (Program ID: 20181010.017) while the dashed lines are from the large island size (Program ID: 20181010.018). The large island case is normalized to the change in edge density. 118

5.20 Change in C-II line intensity at 711 nm between 2 s and 3 s measured with the He beam diagnostic. Ratio = $\frac{ProgramID:20181010.018}{ProgramID:20181010.017}$ 118
5.21 Location of the C-II increase and the shift of T_e and n_e on the Langmuir probe array plotted over figure 3.1. 119
5.22 Photon fluxes over time of a camera in half module 11 equipped with a C-III filter. The photon fluxes are separated by the ROIs introduced in chapter 3. Solid lines represent the normal island size, dashed lines the large one. 120
5.23 Overview plot for Program ID 20181010.036. 121
5.24 Maximum heat flux density averaged over all divertor targets for Program ID 20181010.036 measured by infra red cameras. . 122
5.25 Photon fluxes over time for Program ID 20181010.036. 123
5.26 Source terms for the particle balance τ_p for Program ID: 20181010.036. 124
5.27 Particle confinement time τ_p for Program ID: 20181010.036. . . 125
5.28 Recycling sources normalized to the total recycling flux (Program ID: 20181010.036). 125

6.1 He partial pressure in the divertor of half module 41 (blue) and the He/(H+He) ratio out of charge exchange spectroscopy (yellow) plotted over time for program ID 20181010.020. . . . 129
6.2 H partial pressure in the divertor of half module 41 (blue) and the line averaged electron density from the interferometer (red) plotted over time for program ID 20181010.020. . . . 130

Bibliography

[1] IPCC Climate Change et al. The physical science basis. *Contribution of Working Group I to the fourth assessment report of the Intergovernmental Panel on Climate Change*, 996, 2007.

[2] P Denholm, E Ela, B Kirby, et al. Role of energy storage with renewable electricity generation. Technical report, National Renewable Energy Lab.(NREL), Golden, CO (United States), 2010.

[3] Jeffrey P Freidberg. *Plasma physics and fusion energy*. Cambridge university press, 2008.

[4] Francis F Chen. *Introduction to plasma physics and controlled fusion*, volume 1. Springer, 1984.

[5] John D Lawson. Some criteria for a power producing thermonuclear reactor. *Proceedings of the physical society. Section B*, 70(1):6, 1957.

[6] John Wesson and David J Campbell. *Tokamaks*, volume 149. Oxford university press, 2011.

[7] Lyman Spitzer Jr. The stellarator concept. *The Physics of Fluids*, 1(4):253–264, 1958.

[8] G Grieger, W Lotz, P Merkel, et al. Physics optimization of stellarators. *Physics of Fluids B: Plasma Physics*, 4(7):2081–2091, 1992.

[9] J Nührenberg et al. Development of quasi-isodynamic stellarators. *Plasma Physics and Controlled Fusion*, 52(12):124003, 2010.

[10] Detlev Reiter, GH Wolf, H Kever, et al. Burn condition, helium particle confinement and exhaust efficiency. *Nuclear Fusion*, 30(10):2141, 1990.

[11] P Norajitra, SI Abdel-Khalik, LM Giancarli, et al. Divertor conceptual designs for a fusion power plant. *Fusion Engineering and Design*, 83(7-9):893–902, 2008.

[12] CR Burnett, DJ Grove, RW Palladino, et al. The divertor, a device for reducing the impurity level in a stellarator. *The Physics of Fluids*, 1(5):438–445, 1958.

[13] R König, P Grigull, K McCormick, et al. The divertor program in stellarators. *Plasma physics and controlled fusion*, 44(11):2365, 2002.

[14] Peter C Stangeby. *The plasma boundary of magnetic fusion devices*. CRC Press, 2000.

[15] T Denner, KH Finken, G Mank, et al. Helium partial pressure measurement in a deuterium environment. *Review of scientific instruments*, 67(10):3515–3520, 1996.

[16] E Thomas, U Konopka, D Artis, et al. The magnetized dusty plasma experiment (mdpx). *Journal of Plasma Physics*, 81(2), 2015.

[17] S Benhard, J Boscary, H Greuner, et al. Manufacturing of the wendelstein 7-x divertor and wall protection. *Fusion engineering and design*, 75:463–468, 2005.

[18] KH Finken, KH Dippel, WY Baek, et al. Measurement of helium gas in a deuterium environment. *Review of scientific instruments*, 63(1):1–7, 1992.

[19] T Klinger, T Andreeva, S Bozhenkov, et al. Overview of first wendelstein 7-x high-performance operation. *Nuclear Fusion*, 2019.

[20] J Nührenberg and R Zille. Stable stellarators with medium β and aspect ratio. *Physics Letters A*, 114(3):129–132, 1986.

[21] M Hirsch, J Baldzuhn, C Beidler, et al. Major results from the stellarator wendelstein 7-as. *Plasma Physics and Controlled Fusion*, 50(5):053001, 2008.

[22] Dalton D Schnack. *Lectures in magnetohydrodynamics: with an appendix on extended MHD*, volume 780. Springer, 2009.

[23] CD Beidler, E Harmeyer, F Herrnegger, et al. The helias reactor hsr4/18. *Nuclear Fusion*, 41(12):1759, 2001.

[24] RC Wolf et al. A stellarator reactor based on the optimization criteria of wendelstein 7-x. *Fusion Engineering and Design*, 83(7-9):990–996, 2008.

[25] E Strumberger. Deposition patterns of fast ions on plasma facing components in w7-x. *Nuclear fusion*, 40(10):1697, 2000.

[26] T Sunn Pedersen, M Otte, S Lazerson, et al. Confirmation of the topology of the wendelstein 7-x magnetic field to better than 1: 100,000. *Nature communications*, 7:13493, 2016.

[27] S A Lazerson, M Otte, M Jakubowski, et al. Error field measurement, correction and heat flux balancing on wendelstein 7-x. *Nuclear Fusion*, 57(4):046026, 2017.

[28] A Dinklage, CD Beidler, P Helander, et al. Magnetic configuration effects on the wendelstein 7-x stellarator. *Nature Physics*, 14(8):855, 2018.

[29] A Puig Sitjes, M Jakubowski, A Ali, et al. Wendelstein 7-x near real-time image diagnostic system for plasma-facing components protection. *Fusion Science and Technology*, 74(1-2):116–124, 2018.

[30] P Grigull, K McCormick, J Baldzuhn, et al. First island divertor experiments on the w7-as stellarator. *Plasma physics and controlled fusion*, 43(12A):A175, 2001.

[31] TS Pedersen, R König, M Krychowiak, et al. First results from divertor operation in wendelstein 7-x. *Plasma Physics and Controlled Fusion*, 61(1):014035, 2018.

[32] Y Feng, CD Beidler, J Geiger, et al. On the w7-x divertor performance under detached conditions. *Nuclear Fusion*, 56(12):126011, 2016.

[33] Y Feng, M Kobayashi, T Lunt, et al. Comparison between stellarator and tokamak divertor transport. *Plasma physics and controlled fusion*, 53(2):024009, 2011.

[34] J Boscary, R Stadler, A Peacock, et al. Design and technological solutions for the plasma facing components of wendelstein 7-x. *Fusion Engineering and Design*, 86(6-8):572–575, 2011.

[35] U Wenzel, G Schlisio, P Drewelow, et al. Particle exhaust and neutral compression in w7-x. Oral, International Stellarator and Heliotron Workshop, 9 2019.

[36] A Peacock, H Greuner, F Hurd, et al. Progress in the design and development of a test divertor (tdu) for the start of w7-x operation. *Fusion Engineering and Design*, 84(7-11):1475–1478, 2009.

[37] H Renner, D Sharma, J Kißlinger, et al. Physical aspects and design of the wendelstein 7-x divertor. *Fusion science and technology*, 46(2):318–326, 2004.

[38] J Geiger, CD Beidler, Y Feng, et al. Physics in the magnetic configuration space of w7-x. *Plasma Physics and Controlled Fusion*, 57(1):014004, 2014.

[39] O Schmitz, Y Feng, M Jakubowski, et al. Stable heat and particle flux detachment with efficient particle exhaust in the island divertor of wendelstein 7-x. *EPS invited*, 2019.

[40] JT Hogan, DL Hillis, et al. Helium transport and exhaust in tokamaks report on the international workshop on helium transport and exhaust experiments held at gatlinburg, tennessee, united states of america, 16–18 april 1991. *Nuclear Fusion*, 31(11):2181, 1991.

[41] A Loarte, B Lipschultz, AS Kukushkin, et al. Power and particle control. *Nuclear Fusion*, 47(6):S203, 2007.

[42] MJ Baldwin and RP Doerner. Helium induced nanoscopic morphology on tungsten under fusion relevant plasma conditions. *Nuclear Fusion*, 48(3):035001, 2008.

[43] Martha H Redi, Samuel A Cohen, et al. Effects of particle transport on helium ash accumulation and sustained ignition in the international thermonuclear experimental reactor. *Fusion Technology*, 20(1):48–57, 1991.

[44] HS Bosch, D Coster, R Dux, et al. Particle exhaust studies in asdex upgrade. *Plasma physics and controlled fusion*, 39(11):1771, 1997.

[45] MR Wade, DL Hillis, JT Hogan, et al. Helium transport and exhaust studies in enhanced confinement regimes in diii-d. *Physics of Plasmas*, 2(6):2357–2365, 1995.

[46] MR Wade, DL Hillis, JT Hogan, et al. Helium exhaust studies in h-mode discharges in the diii-d tokamak using an argon-frosted divertor cryopump. *Physical review letters*, 74(14):2702, 1995.

[47] Y Nakamura, Y Takeiri, BJ Peterson, et al. Impurity behaviour in lhd long pulse discharges. *Plasma physics and controlled fusion*, 44(10):2121, 2002.

[48] Y Nakamura, Y Takeiri, R Kumazawa, et al. Plasma performance and impurity behaviour in long pulse discharges on lhd. *Nuclear fusion*, 43(4):219, 2003.

[49] Y Nakamura, M Kobayashi, S Yoshimura, et al. Impurity shielding criteria for steady state hydrogen plasmas in the lhd, a heliotron-type device. *Plasma Physics and Controlled Fusion*, 56(7):075014, 2014.

[50] O Schmitz, K Ida, M Kobayashi, et al. Enhancement of helium exhaust by resonant magnetic perturbation fields at lhd and textor. *Nuclear Fusion*, 56(10):106011, 2016.

[51] U Samm, J Boedo, G Bertschinger, et al. Helium exhaust in plasmas with strong radiative edge cooling. *Journal of nuclear materials*, 196:633–636, 1992.

[52] ISO. *ISO 21360-1:2012 - Vacuum technology — Standard methods for measuring vacuum-pump performance — Part 1: General description*. Beuth Verlag, Berlin, 2012.

[53] H-S Bosch, G Haas, M Lörcher, et al. Helium and hydrogen atom detection in the recycling gas using optical measurements on an asdex pressure gauge. *Journal of nuclear materials*, 196:1074–1077, 1992.

[54] Frans Michel Penning. Die glimmentladung bei niedrigem druck zwischen koaxialen zylindern in einem axialen magnetfeld. *physica*, 3(9):873–894, 1936.

[55] G Gabrielse, P Larochelle, D Le Sage, et al. Antiproton confinement in a penning-ioffe trap for antihydrogen. *Physical review letters*, 98(11):113002, 2007.

[56] Arian Kriesch. Penning trap. https://en.wikipedia.org/wiki/Penning_trap#/media/File:Penning_Trap.svg, 2006. [Online; accessed 19-Nov-2019].

[57] Lowell S Brown and Gerald Gabrielse. Geonium theory: Physics of a single electron or ion in a penning trap. *Reviews of Modern Physics*, 58(1):233, 1986.

[58] jrzs. ion's trajectory penning trap. https://en.wikipedia.org/wiki/Penning_trap#/media/File:Penningtrajec.png, 2008. [Online; accessed 19-Nov-2019].

[59] A Pospieszczyk. Diagnostics of edge plasmas by optical methods, 1993.

[60] S Brezinsek, G Sergienko, A Pospieszczyk, et al. Characterization of the deuterium recycling flux in front of a graphite surface in the textor tokamak. *Plasma physics and controlled fusion*, 47(4):615, 2005.

[61] S Brezinsek, PT Greenland, Ph Mertens, et al. On the measurement of molecular particle fluxes in fusion boundary plasmas. *Journal of nuclear materials*, 313:967–971, 2003.

[62] https://open.adas.ac.uk/.

[63] D Hathiramani, A Ali, G Anda, et al. Upgrades of edge, divertor and scrape-off layer diagnostics of w7-x for op1. 2. *Fusion Engineering and Design*, 136:304–308, 2018.

[64] C Hennig, J Maier, M Grün, et al. Archivedb—scientific and technical data archive for wendelstein 7-x. *Fusion Engineering and Design*, 112:984–990, 2016.

[65] M Grahl, T Bluhm, M Grün, et al. Archive web api: A web service for the experiment data archive of wendelstein 7-x. *Fusion Engineering and Design*, 123:1015–1019, 2017.

[66] VP Drachev, Yu I Krasnikov, and PA Bagryansky. Dispersion interferometer for controlled fusion devices. *Review of scientific instruments*, 64(4):1010–1013, 1993.

[67] T Akiyama, R Yasuhara, K Kawahata, et al. Dispersion interferometer using modulation amplitudes on lhd. *Review of Scientific Instruments*, 85(11):11D301, 2014.

[68] https://w7x-logbook.ipp-hgw.mpg.de/.

[69] KJ Brunner, T Akiyama, M Hirsch, et al. Real-time dispersion interferometry for density feedback in fusion devices. *Journal of Instrumentation*, 13(09):P09002, 2018.

[70] Keith H Burrell. Fast hydrogen gas injection system for plasma physics experiments. *Review of Scientific Instruments*, 49(7):948–954, 1978.

[71] T Barbui, SA Bozhenkov, F Effenberg, et al. The he/ne beam diagnostic for line-ratio spectroscopy in the island divertor of wendelstein 7-x. *Journal of Instrumentation*, 14(07):C07014, 2019.

[72] M Griener, O Schmitz, K Bald, et al. Fast piezoelectric valve offering controlled gas injection in magnetically confined fusion plasmas for diagnostic and fuelling purposes. *Review of scientific instruments*, 88(3):033509, 2017.

[73] JM Muñoz Burgos, O Schmitz, SD Loch, et al. Hybrid time dependent/independent solution for the he i line ratio temperature and density diagnostic for a thermal helium beam with applications in the scrape-off layer-edge regions in tokamaks. *Physics of plasmas*, 19(1):012501, 2012.

[74] O Schmitz, IL Beigman, LA Vainshtein, et al. Status of electron temperature and density measurement with beam emission spectroscopy on thermal helium at textor. *Plasma physics and controlled fusion*, 50(11):115004, 2008.

[75] Noah Hershkowitz. How langmuir probes work. *Plasma diagnostics*, 1:113–183, 1989.

[76] Sin-Li Chen and T Sekiguchi. Instantaneous direct-display system of plasma parameters by means of triple probe. *Journal of Applied Physics*, 36(8):2363–2375, 1965.

[77] R Brakel, M Köppen, A Peacock, et al. Specification of Design Loads for In-vessel Components of W7-X 1-qdp50–a. Technical report, Max-Planck-Institut für Plasmaphysik, 03 2019.

[78] L Rudischhauser, K C Hammond, M Endler, et al. Characterisation of the wendelstein 7-x divertor plasma with langmuir probes. *Verhandlungen der Deutschen Physikalischen Gesellschaft*, 2018.

[79] M Rudischhauser et al. The langmuir probe system in the wendelstein 7-x test divertor unit. *Review of Scientific Instruments*, in submission.

[80] D Nicolai, V Borsuk, P Drews, et al. A multi-purpose manipulator system for w7-x as user facility for plasma edge investigation. *Fusion Engineering and Design*, 123:960–964, 2017.

[81] A. Lorenz C. Baylard. Projektspezifikation multi-purpose manipulator. Technical report, MPG-IPP, 2013.

[82] M Hubeny, D Höschen, M Rack, et al. Diagnostic setup for the divertor manipulator at wendelstein 7-x. *Nuclear Materials and Energy*, 18:77–81, 2019.

[83] R König, J Baldzuhn, W Biel, et al. The set of diagnostics for the first operation campaign of the wendelstein 7-x stellarator. *Journal of Instrumentation*, 10(10):P10002, 2015.

[84] Max-Planck-IPP. Fish-eye view of w7-x interior. https://3c1703fe8d.site.internapcdn.net/newman/gfx/news/hires/2017/2-ppplphysicis.jpg, 2018. [Online; accessed 19-Nov-2019].

[85] P Drewelow. Private communication.

[86] O Schmitz, JW Coenen, H Frerichs, et al. Particle confinement control with resonant magnetic perturbations at textor. *Journal of nuclear materials*, 390:330–334, 2009.

[87] VA Soukhanovskii, R Maingi, R Raman, et al. Core fueling and edge particle flux analysis in ohmically and auxiliary heated nstx plasmas. *Journal of nuclear materials*, 313:573–578, 2003.

[88] R Maingi, GL Jackson, MR Wade, et al. Control of wall particle inventory with divertor pumping on diii-d. *Nuclear fusion*, 36(2):245, 1996.

[89] Steven P Hirshman and JC Whitson. Steepest-descent moment method for three-dimensional magnetohydrodynamic equilibria. *The Physics of fluids*, 26(12):3553–3568, 1983.

[90] AR Akerson, A Bader, CC Hegna, et al. Three-dimensional scrape off layer transport in the helically symmetric experiment hsx. *Plasma Physics and Controlled Fusion*, 58(8):084002, 2016.

[91] D Reiter, M Baelmans, and P Boerner. The eirene and b2-eirene codes. *Fusion science and technology*, 47(2):172–186, 2005.

[92] S Brezinsek, Ph Mertens, A Pospieszczyk, et al. Hydrogen atom velocities and penetration depths in front of graphite surfaces in textor. *Physica Scripta*, 2003(T103):51, 2003.

[93] HF Dylla, PH LaMarche, M Ulrickson, et al. Conditioning of the graphite bumper limiter for enhanced confinement discharges in tftr. *Nuclear fusion*, 27(8):1221, 1987.

[94] DL Hillis, KH Finken, JT Hogan, et al. Helium exhaust and transport studies with the alt-ii pump limiter in the textor tokamak. *Physical review letters*, 65(19):2382, 1990.

[95] K Flesch, T Kremeyer, O Schmitz, et al. Development of miniaturized, spectroscopically assisted penning gauges for fractional helium and hydrogen neutral pressure measurements. *Review of Scientific Instruments*, 87(11):11E529, 2016.

[96] R Raman, HW Kugel, T Provost, et al. Fast neutral pressure measurements in nstx. *Review of scientific instruments*, 74(3):1900–1904, 2003.

[97] W Knauer. Mechanism of the penning discharge at low pressures. *Journal of Applied Physics*, 33(6):2093–2099, 1962.

[98] Pfeiffer Vacuum GmbH. *The vacuum technology book*, volume 2. Pfeiffer Vacuum GmbH, 4 2013.

[99] GW Pacher, HD Pacher, G Janeschitz, et al. Modelling of demo core plasma consistent with sol/divertor simulations for long-pulse scenarios with impurity seeding. *Nuclear fusion*, 47(5):469, 2007.

[100] H-S Bosch, R Brakel, T Braeuer, et al. Final integration, commissioning and start of the wendelstein 7-x stellarator operation. *Nuclear Fusion*, 57(11):116015, 2017.

[101] U Wenzel, T Kremeyer, G Schlisio, et al. Advanced neutral gas diagnostics for magnetic confinement devices. *Journal of Instrumentation*, 12(09):C09008, 2017.

[102] RJ Colchin, DL Hillis, R Maingi, et al. The filterscope. *Review of scientific instruments*, 74(3):2068–2070, 2003.

[103] U Wenzel, TS Pedersen, M Marquardt, et al. An ionization pressure gauge with lab6 emitter for long-term operation in strong magnetic fields. *Review of Scientific Instruments*, 89(3):033503, 2018.

[104] T Stange, HP Laqua, M Beurskens, et al. Advanced electron cyclotron heating and current drive experiments on the stellarator wendelstein 7-x. In *EPJ Web of Conferences*, volume 157, page 02008. EDP Sciences, 2017.

[105] L Stephey, GA Wurden, O Schmitz, et al. Spectroscopic imaging of limiter heat and particle fluxes and the resulting impurity sources during wendelstein 7-x startup plasmas. *Review of Scientific Instruments*, 87(11):11D606, 2016.

[106] M Hirsch, A Dinklage, A Alonso, et al. Confinement in wendelstein 7-x limiter plasmas. *Nuclear Fusion*, 57(8):086010, 2017.

[107] LM Kovrizhnykh. The energy confinement time in stellarators. *Nuclear fusion*, 24(4):435, 1984.

[108] D Zhang, R Burhenn, R Koenig, et al. Design criteria of the bolometer diagnostic for steady-state operation of the w7-x stellarator. *Review of Scientific Instruments*, 81(10):10E134, 2010.

[109] B Buttenschön, R Burhenn, M Kubkowska, et al. Spectroscopic impurity survey in the first operation phase of wendelstein 7-x. In *43rd EPS Conference on Plasma Physics P*, volume 4, 2016.

[110] A Greiche, W Biel, O Marchuk, et al. Absolute intensity calibration of the wendelstein 7-x high efficiency extreme ultraviolet overview spectrometer system. *Review of scientific instruments*, 79(9):093504, 2008.

[111] Y Feng, CD Beidler, J Geiger, et al. On the w7-x divertor performance under detached conditions. *Nuclear Fusion*, 56(12):126011, 2016.

[112] H Grote. Private communication.